Interaction of atoms with twisted light

seit 1558

Dissertation

zur Erlangung des akademischen Grades

doctor rerum naturalium (Dr. rer. nat.)

vorgelegt dem Rat der Physikalisch-Astronomischen Fakultät

der Friedrich-Schiller-Universität Jena

von M.Sc. Anton Anatolyevich Peshkov

geboren am 10.06.1991 in Woronesch, Russland

Gutachter

1. Prof. Dr. Stephan Fritzsche, Friedrich-Schiller-Universität Jena

2. Prof. Dr. Nikolay M. Kabachnik, Lomonosov Moscow State University

3. Prof. Dr. Jamal Berakdar, Martin-Luther-Universität Halle-Wittenberg

Tag der Disputation: 21. Juni 2018

Zusammenfassung

Getwistete Photonen sind Teilchen, die eine wohl-definierte Bahndrehimpulskomponente entlang der Propagationsrichtung besitzen. In den letzten Jahren ist die Wechselwirkung zwischen einem getwisteten Photon und einem Atom zu einem aktiven fundamentalen sowie angewandtenen Forschungsgebiet geworden. In dieser Arbeit wird dargestellt, wie der „Twist“ eines Bessel- oder Laguerre-Gauß Photons die Wechselwirkung zwischen Licht und Materie im Vergleich zu ebenen Wellen beeinflussen kann. Insbesondere wurde eine Analyse der Photoionisation von Wasserstoff-Molekülionen durch getwistete Photonen durchgeführt. Es wurde gezeigt, dass die Oszillationen in den Winkelverteilungen der Photoelektronen durch das Intensitätsprofil der getwisteten Photonen beeinflusst werden. Außerdem wurde die Anregung von Atomen durch Absorption eines getwisteten Photons berechnet. Der Bahndrehimpuls des Lichtes führt zu einem Alignment oder speziellen Besetzung der magnetischen Zustände des angeregten Atoms. Neben diesen Studien wurde auch die elastische Rayleigh Streuung von getwisteten Photonen an wasserstoffähnlichen Ionen untersucht. Die erhaltenen Ergebnisse zeigen, dass der „Twist“ eines Photons die Polarisationseigenschaften von gestreutem Licht signifikant beeinflussen kann.

Contents

1 Introduction

1.1 Historical background

The first suggestions that matter is composed of discrete particles were made by the Greek philosophers such as Leucippus (circa 450 bc) and Democritus (460-370 bc) (Bransden and Joachain 2003, Demtröder 2011). They assumed that the universe consists of empty space and of invisible particles or atoms. The real breakthrough of atomic physics was achieved in modern times. The experimental discovery of the gas laws by Boyle in 1662 and their interpretation in terms of a kinetic model by Bernoulli in 1738 have paved the way to the kinetic theory of atoms developed throughout the 19th century by Clausius, Maxwell, and Boltzmann. In parallel, following the qualitative findings of Proust in 1801 on mass ratios in chemical reactions, Dalton recognized in 1808 that all chemical elements consist of very small particles (atoms) which cannot be divided by chemical techniques. Also in 1808, Gay-Lussac found that if two gases are combined, the volumes are in the ratio of simple integers. In 1811, this result was explained by Avogadro who first made a clear distinction between atoms and molecules which are composed of two and more atoms bound together.

Various experimental investigations have shown in the end of 19th century that atoms contain negatively charged light particles, called electrons, and a positive charge. After a series of experiments on the scattering of alpha particles by metallic foils performed between 1906 and 1913 by Geiger and Marsden, Rutherford suggested that all the positive charge and almost all the mass of an atom are concentrated at the center of the atom in a nucleus of very small dimensions. In 1932, Ivanenko and Heisenberg suggested that this nucleus is composed of protons of positive charge and uncharged neutrons, which in turn are made of more elementary constituents, the quarks, as was proposed by Gell-Mann and Zweig in 1964.

The nature of light was also the major subject of research in the 18th century (Fox 2006). Newton postulated that light should consist of small particles, and this model explained the straight paths of light rays and the refraction of light at the boundary between two media. Huygens, on the other hand, believed that light was a wave, and the wave theory was proven by the double-slit experiment of Young in 1801 and by the wave interpretation of diffraction by Fresnel in 1815. As a result, the wave

theory has been put on a firm theoretical footing with Maxwell's electromagnetic equations in 1873, while the corpuscular theory has essentially been relegated to historical interest by the end of the 19th century. However, the situation changed in 1901, when Planck suggested that black-body radiation is emitted in finite amount of energy called quantum or photons, and he was able to solve the ultraviolet catastrophe problem with this hypothesis. Moreover, in a series of experiments on the properties of electromagnetic waves, Hertz, Hallwachs, Lenard, and Stoletov showed that charged particles are ejected from metal surfaces irradiated by electromagnetic waves of high frequency, and Einstein in 1905 applied Planck's quantum theory to explain this phenomenon (photoelectric effect).

The next major step forward to understanding the light-matter interaction was taken by Bohr in 1913. With the assumption that an electron in an atom moves in only stable orbits about the nucleus, he was able to combine the concepts of Rutherford nuclear atom, Planck's quanta, and Einstein's photons to explain the spectrum of atomic hydrogen. These pioneering ideas laid the foundations for the quantum mechanics in the years 1925 and 1926 by Heisenberg, Born, Jordan, de Broglie, and Scrödinger. Finally, the foundations of the quantum electrodynamics (QED), the relativistic quantum theory of the interaction of charged particles and photons, have been laid down by 1932.

Since then, the quantum aspects of the dynamics of atoms and ions in light fields have been extensively studied in both experiment and theory. In particular, the analysis of relativistic effects such as spin-flip contributions and higher-order multipole transitions in the photoionization of highly charged heavy ions is presented by Eichler and Stöhlker (2007), while the many-electron effects in the photoelectron spectrum for neutral atoms are discussed by Cubaynes *et al* (1989). Extensive studies of the atomic photoionization under intense laser irradiation have revealed many other effects, namely above-threshold ionization, electron wave-packet drift, quiver and rescattering motions (Blaga *et al* 2009). The radiative transitions between bound atomic states have also been intensively investigated, and they have found many applications in different areas. For instance, in Rudolph *et al* (2013) X-ray resonant photoexcitation was used to determine the linewidth of transitions in iron ions, which is important for understanding of photoexcited plasmas found in active galactic nuclei. The measurement of the lifetime of metastable levels in boronlike argon was employed to test QED effects like the electron anomalous magnetic moment and Breit interaction (Lapierre *et al* 2005). Moreover, the cesium

4

ground-state hyperfine transition in atomic clocks serves as the accurate frequency standard (Oskay *et al* 2006).

Much attention has also been paid to the scattering of photons by atoms. The first measurement of the elastically (Rayleigh) scattered light for linearly polarized incoming X-rays has been performed recently at the PETRA III synchrotron at DESY (Blumenhagen *et al* 2016), while the general details of the inelastic (Raman) photon scattering may be found in Kane (1992). In addition, many research teams around the world use laser radiation to cool a gas of atoms to temperatures in the microkelvin range, when the laser frequency is close to resonance with an atomic transition. A great triumph of the laser cooling together with atom trapping has been the observation of Bose–Einstein condensation in a vapor of rubidium atoms in Anderson *et al* (1995). At the same time, the first quantum logic gate was demonstrated in an ion trap system using a single beryllium ion, when the qubit manipulations were driven by lasers (Monroe *et al* 1995).

1.2 Light's orbital angular momentum

Until the present, however, all these investigations have been performed with incident plane-wave radiation, and very little is known about the interaction of atoms with twisted (or vortex) light beams. In contrast to plane waves, such twisted photons carry a nonzero projection of the orbital angular momentum (OAM) upon their propagation direction (Andrews and Babiker 2013). The study of light's angular momentum has a long history (Bliokh and Nori 2015). In 1909, Poynting realized that light has spin angular momentum associated with circular polarization, and it was confirmed experimentally by Beth in 1936. A paper by Allen *et al* (1992) started a new wave of angular momentum studies in optics, where they recognized that light beams with helical wavefronts carry an orbital angular momentum independent of the polarization state. Baranova and Zel'dovich (1981) have earlier introduced the term "twisted beams" for such electromagnetic fields. The twisted beams are also said to contain an optical vortex because their Poynting vector, representing energy flow, follows a spiral trajectory around the beam axis (Padgett *et al* 2004). The transverse intensity profile of twisted beams has an annular character, while the phase singularity on the beam axis dictates zero intensity at the center.

Beams carrying OAM can be readily produced with the help of computer-generated holograms, spatial light modulators, axions, and helical undulators in the wide pho-

ton energy range from THz to XUV (Walde *et al* 2017, Bahrdt *et al* 2013, Choporova *et al* 2017). The fact that twisted photons carry OAM presents possibilities for using them in practice (Yao and Padgett 2011). For example, one application of the angular momentum of light is for optical tweezers, in which trapped object is rotated by the transfer of OAM from a twisted beam (Padgett and Bowman 2011). The OAM of photons also enables the generation and manipulation of multidimensional quantum states, which may make quantum correlations more robust to the presence of noise and can provide better security in quantum cryptographic schemes (Molina-Terriza *et al* 2007). Moreover, the use of optical vortex coronagraph in astronomy makes binary system more visible (Swartzlander *et al* 2008).

During the last years a number of investigations have demonstrated that "twistedness" of incoming radiation may affect fundamental light-matter interaction processes. In the Compton scattering of twisted light by free electrons, the angular distributions of scattered photons and their phase structure are sensitive to the OAM projection of incident light (Jentschura and Serbo 2011, Stock *et al* 2015, Sherwin 2017). It was shown by Scholz-Marggraf *et al* (2014), Surzhykov *et al* (2015), Schmiegelow and Schmidt-Kaler (2012), Rodrigues *et al* (2016), and Afanasev *et al* (2013) that the alignment of the excited atomic states following absorption of twisted photons may differ from what is expected for incoming plane-wave radiation. In particular, Schmiegelow *et al* (2016) in a recent experiment demonstrated the transfer of OAM from a twisted photon to the valence electron of a single trapped calcium ion. Furthermore, the OAM may significantly modify the angular distribution (Matula *et al* 2013, Surzhykov *et al* 2016, Seipt *et al* 2016) along with energy distribution (Müller *et al* 2016), time delay (Wätzel and Berakdar 2016), and dynamics (Picón *et al* 2010) of photoelectrons in the photoionization of atoms. The general properties of the scattering of twisted photons were discussed by Davis *et al* (2013).

It was also demonstrated by Babiker *et al* (2002) that in the interaction of molecules with twisted light an exchange of OAM can occur between the light and the center of mass motion. The transfer of phase structure from applied laser radiation to optical fields generated in a four-wave-mixing process in atomic vapor has been observed in a number of works (Tabosa and Petrov 1999, Walker *et al* 2012, Akulshin *et al* 2015). Moreover, an azimuthal modulation of the absorption profile, that is dictated by the phase and polarization structure of the probe laser, was observed in electromagnetically induced transparency systems with twisted beams (Radwell

6

et al 2015). Theoretical studies in solid-state physics also predict that twisted light can induce new electronic transitions in quantum dots which are forbidden for plane waves (Quinteiro *et al* 2015). Apart from that, the generation of electric currents in quantum rings with twisted light was studied by Quinteiro and Berakdar (2009).

1.3 A brief overview of the thesis

In this thesis we will focus on three different atomic processes occurring in twisted light, namely on photoionization of diatomic molecules, atomic excitation, and Rayleigh scattering by ions. We start in Chapter 2 by considering two different types of twisted light beams such as Bessel and Laguerre-Gaussian beams. We introduce the vector potentials for both these beams, that will be used in our further calculations, and analyze the difference between them and plane-wave photons. Then in Chapter 3 we study the ionization of hydrogen molecular ions by twisted Bessel beams, where the angle-differential photoionization cross section is evaluated for a macroscopic target of randomly distributed but aligned molecules. We see there that main modifications in the angular distribution of the photoelectrons arise due to the ringlike pattern of Bessel beams and their intensity variation relative to the size of the molecule. Chapter 4 deals with the excitation of mesoscopic hydrogen-atom target by twisted Bessel beams. Results of the calculations performed for the $1s \rightarrow 2p$ transition clearly indicate that projection of the total angular momentum of Bessel beam affects the alignment of excited atomic states for sufficiently small targets of size less than several hundreds of nanometers. We show that this effect can be observed experimentally by measuring the linear polarization of the subsequent fluorescence.

Chapter 5 considers the excitation of a single calcium ion by twisted Laguerre-Gaussian beams which are more frequently used in experiments. For the $4s\ ^2S_{1/2} \rightarrow 3d\ ^2D_{5/2}$ transition, we demonstrate that the magnetic sublevel population of the excited $^2D_{5/2}$ level varies significantly with the atomic position with regard to the beam axis and is sensitive to the polarization, the radial index, as well as the OAM of the incident Laguerre-Gaussian beam. In Chapter 6 we perform an analysis of the nonresonant Rayleigh scattering of Bessel beams by hydrogenlike ions, where special attention is paid to the polarization Stokes parameters of photons scattered by carbon ions. It is shown that the polarization of scattered photons for incoming Bessel beams may significantly differ from what is expected for incident plane-wave

radiation. Finally, a summary of our results is given in Chapter 7.

Atomic units ($\hbar = e = m_e = 1$, $c = 1/\alpha$) are used throughout the work unless stated otherwise.

2 Twisted light

In this chapter we shall give a brief introduction to the theory of twisted photon states. We first consider the vector potential of more familiar plane wave photons and discuss their quantum mechanical properties. Then we construct a twisted Bessel beam from these plane waves and derive its vector potential in position space. Using this approach we recall the concept of the orbital angular momentum of light. The chapter concludes with a discussion of the principal features of another twisted beam, namely Laguerre-Gaussian beam, where we describe how one can expand its vector potential in plane waves working within the Coulomb gauge convenient for further atomic calculations.

2.1 Plane waves

2.1.1 Plane-wave solutions

In general, all the properties of photons are characterized by means of the vector potential $\boldsymbol{A}(\boldsymbol{r}, t)$. Here we limit our attention to monochromatic light with photon energy $\hbar\omega$, and therefore we can separate the vector potential into a part with the spatial dependence and a time dependent factor $\boldsymbol{A}(\boldsymbol{r}, t) = \boldsymbol{A}(\boldsymbol{r}) \exp(-i\omega t)$. In this case, the vector potential $\boldsymbol{A}(\boldsymbol{r})$ is a solution of the Helmholtz equation when no sources are present (Andrews and Babiker 2013)

$$\nabla^2 \boldsymbol{A} + k^2 \boldsymbol{A} = 0 \,, \tag{2.1}$$

were $k = \omega/c$ denotes the wave number. Let us consider plane-wave solutions of this equation. If we suppose that the circularly polarized plane wave propagates in the z direction with the wave vector

$$\boldsymbol{k} = \begin{pmatrix} 0 \\ 0 \\ k \end{pmatrix} \,, \tag{2.2}$$

its vector potential can be written as

$$\boldsymbol{A}^{\mathrm{pl}}(\boldsymbol{r}) = \boldsymbol{\varepsilon}_\lambda e^{ikz} \,, \tag{2.3}$$

where $\boldsymbol{\varepsilon}_\lambda$ refers to the polarization vector of the form

$$\boldsymbol{\varepsilon}_\lambda = \frac{-\lambda}{\sqrt{2}} \begin{pmatrix} 1 \\ i\lambda \\ 0 \end{pmatrix}. \tag{2.4}$$

Such a plane-wave photon is right-hand circularly polarized when $\lambda = +1$, and it is left-hand circularly polarized when $\lambda = -1$. Its wavefront is determined by the relation $kz - \omega t = 0$ that arises from the exponential factor in Eq. (2.3) and represents a plane as shown in Fig. 2.1 (a).

The vector potential (2.3) of the plane wave is expressed in Coulomb gauge which is defined by the condition

$$\nabla \cdot \boldsymbol{A} = 0. \tag{2.5}$$

In the Coulomb gauge, the electric $\boldsymbol{E}$ and magnetic $\boldsymbol{B}$ fields satisfying Maxwell's equations are represented in terms of a vector potential through the relations

$$\boldsymbol{E} = i\omega \boldsymbol{A}, \quad \boldsymbol{B} = \nabla \times \boldsymbol{A}. \tag{2.6}$$

It should be noted that the vector potential is not completely defined by these equations, since the fields $\boldsymbol{E}$ and $\boldsymbol{B}$ are invariant with regard to the gauge transformation. It is useful to consider the time-averaged flux of energy in an electromagnetic wave which can be calculated from the real part of the complex Poynting vector

$$\boldsymbol{S} = \frac{1}{2} \boldsymbol{E} \times \boldsymbol{B}^*, \tag{2.7}$$

giving the intensity of a light wave (Jackson 1962). For the plane wave discussed here, the Poynting vector is parallel to the propagation z axis and has the same value at each point of space, thereby implying a homogeneous intensity profile as seen from Fig. 2.1 (b).

2.1.2 Properties of plane-wave photons

Let us now analyze the quantum mechanical properties of the plane-wave photons. By making use of the longitudinal (z) momentum operator $\hat{p}_z = -i\partial/\partial z$, one can show that the vector potential (2.3) is its eigenfunction

$$\hat{p}_z \boldsymbol{A}^{\mathrm{pl}} = k\boldsymbol{A}^{\mathrm{pl}} \tag{2.8}$$
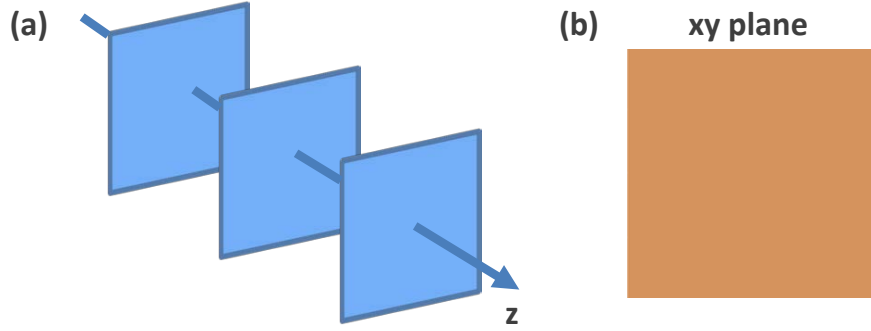
Figure 2.1: (a) Wavefronts of a plane wave are planes. (b) Its transverse (xy) intensity profile; the plane wave has the same intensity at each point of space.

with the eigenvalue k. This implies that the plane-wave photon (2.3) propagating in the z direction with the energy $\omega = kc$ has a well-defined z-component k of the momentum. Plane-wave photons travelling parallel to the z axis do not have a component of orbital angular momentum in the z direction. The angular momentum carried by the photons in this case can only be due to their intrinsic spin of unit magnitude corresponding to the fact that their wave function (2.3) is a vector. Applying the operator for z-component of the spin angular momentum for particles with spin 1 (Johnson 2007)

$$\hat{S}_z = \begin{pmatrix} 0 & -i & 0 \\ i & 0 & 0 \\ 0 & 0 & 0 \end{pmatrix} \tag{2.9}$$

to the vector potential (2.3) for the plane waves, we have

$$\hat{S}_z \boldsymbol{A}^{\mathrm{pl}} = \lambda \boldsymbol{A}^{\mathrm{pl}}. \tag{2.10}$$

Therefore, the vector potential $\boldsymbol{A}^{\mathrm{pl}}$ is an eigenfunction of the z-component $\hat{S}_z$ of the spin angular momentum (SAM) operator, and the plane-wave photons (2.3) have a well-defined component $\lambda = \pm 1$ of the spin in the (z) direction of motion, which is sometimes known as the helicity of a photon.

2.1.3 Plane waves propagating in arbitrary directions

So far, we have concentrated on plane waves propagating along the quantization z axis. In the general case, when a plane wave propagates in the direction (θ_k, ϕ_k)

with respect to the z axis, the momentum $\boldsymbol{k}$ of the photon reads

$$\boldsymbol{k} = \begin{pmatrix} k_\perp \cos \phi_k \\ k_\perp \sin \phi_k \\ k_z \end{pmatrix}, \qquad (2.11)$$

where $\theta_k = \arctan(k_\perp/k_z)$ and ϕ_k denote respectively the polar and azimuthal angles of the photon's momentum $\boldsymbol{k}$ whose absolute value is $k = \sqrt{k_\perp^2 + k_z^2}$. For such a plane wave, we need to rewrite its polarization vector as (Matula *et al* 2013)

$$\boldsymbol{e}_{\boldsymbol{k}\lambda} = \frac{-\lambda}{\sqrt{2}} \begin{pmatrix} \cos \theta_k \cos \phi_k - i\lambda \sin \phi_k \\ \cos \theta_k \sin \phi_k + i\lambda \cos \phi_k \\ -\sin \theta_k \end{pmatrix}, \qquad (2.12)$$

so that the circularly polarized plane wave $\boldsymbol{e}_{\boldsymbol{k}\lambda} e^{i\boldsymbol{k}\boldsymbol{r}}$ characterizes the photon with spin projection λ onto its momentum $\boldsymbol{k}$. In addition, from the Coulomb gauge condition (2.5) it follows that the polarization vector is orthogonal to the momentum, $\boldsymbol{e}_{\boldsymbol{k}\lambda} \cdot \boldsymbol{k} = 0$. Below we shall use these plane waves to construct from them the twisted beams.

2.2 Bessel beams

2.2.1 Bessel beam as a superposition of plane waves

Having discussed the properties of the plane waves, we may now introduce the Bessel beams of light. Following Jentschura and Serbo (2011) and Matula *et al* (2013), we define the vector potential of a Bessel beam propagating along the quantization z axis with well-defined longitudinal momentum k_z, modulus of the transverse momentum $\varkappa$, and photon energy $\omega = c\sqrt{\varkappa^2 + k_z^2}$ as

$$\boldsymbol{A}^{\mathrm{B}}(\boldsymbol{r}) = \int a_{\varkappa m_\gamma}(\boldsymbol{k}_\perp)\, \boldsymbol{e}_{\boldsymbol{k}\lambda} e^{i\boldsymbol{k}\boldsymbol{r}} \frac{d^2\boldsymbol{k}_\perp}{(2\pi)^2} \qquad (2.13)$$

together with the amplitude

$$a_{\varkappa m_\gamma}(\boldsymbol{k}_\perp) = \sqrt{\frac{2\pi}{\varkappa}}(-i)^{m_\gamma}\, e^{im_\gamma \phi_k}\, \delta(k_\perp - \varkappa)\,. \qquad (2.14)$$

The vector potential for a Bessel beam as well as for a plane wave is a solution of the Helmholtz equation (2.1) expressed in Coulomb gauge (2.5). The formula for $\boldsymbol{A}^{\mathrm{B}}$

indicates that the Bessel beam can be understood as a superposition of circularly polarized plane waves $\boldsymbol{e}_{\boldsymbol{k}\lambda}e^{i\boldsymbol{k}\boldsymbol{r}}$ of helicity λ whose wave vectors (2.11) with $k_\perp = \varkappa$ form the surface of a cone with an opening angle $\theta_k = \arctan(\varkappa/k_z)$ [cf. Fig. 2.2 (a)].

2.2.2 Bessel beam in position space

Even though the integral representation (2.13) of the vector potential $\boldsymbol{A}^{\mathrm{B}}(\boldsymbol{r})$ is convenient for atomic calculations, it is useful to perform the integration over the momentum $\boldsymbol{k}_\perp$. With the polarization vector (2.12), the relation $\boldsymbol{k}_\perp \boldsymbol{r}_\perp = k_\perp r_\perp \cos(\phi_k - \phi)$, and the integral formula for the Bessel function of the first kind (Watson 1966)

$$\int_0^{2\pi} e^{im\phi_k \pm ik_\perp r_\perp \cos(\phi_k - \phi)} \frac{d\phi_k}{2\pi} = (\pm i)^m e^{im\phi} J_m(k_\perp r_\perp) , \tag{2.15}$$

we can perform the integration over the azimuthal angle ϕ_k in Eq. (2.13). Then, on integrating over $k_\perp$ and by making use of the Dirac delta function $\delta(k_\perp - \varkappa)$, we find the vector potential of a Bessel beam in cylindrical coordinates

$$\boldsymbol{A}^{\mathrm{B}}(\boldsymbol{r}) = \sum_{m_s = 0, \pm 1} \boldsymbol{\varepsilon}_{m_s} c_{m_s} J_{m_\gamma - m_s}(\varkappa r_\perp) e^{i(m_\gamma - m_s)\phi} e^{ik_z z} , \tag{2.16}$$

where the coefficients c_{m_s} are independent of $\boldsymbol{r}$ and are defined by

$$c_{\pm 1} = \frac{(-i)^{m_s}}{2}\sqrt{\frac{\varkappa}{2\pi}}(1 \pm \lambda \cos\theta_k) , \quad c_0 = \frac{(-i)^{m_s}\lambda}{\sqrt{2}}\sqrt{\frac{\varkappa}{2\pi}}\sin\theta_k . \tag{2.17}$$

Here we have made use of three eigenvectors $\boldsymbol{\varepsilon}_{m_s}$ of SAM operator (2.9) given by Eq. (2.4) in the case of $m_s = \lambda = \pm 1$, while $\boldsymbol{\varepsilon}_0$ is just a unit vector along the z axis. The vector potential $\boldsymbol{A}^{\mathrm{B}}$ can be further simplified if the transverse momentum of the photon is much smaller comparing to its longitudinal momentum $\varkappa \ll k_z$, i.e. when the opening angle θ_k is very small. Within this paraxial approximation, the summation in Eq. (2.16) is restricted to the single term $m_s = \lambda$, and we have

$$\boldsymbol{A}^{\mathrm{B}}(\boldsymbol{r}) = \boldsymbol{\varepsilon}_\lambda c_\lambda J_{m_\gamma - \lambda}(\varkappa r_\perp) e^{i(m_\gamma - \lambda)\phi} e^{ik_z z} . \tag{2.18}$$

We note that in the limit $\varkappa \to 0$, where $J_{m_\gamma - \lambda}(\varkappa r_\perp) \to \delta_{m_\gamma \lambda}$, this formula reproduces the plane wave (2.3) propagating along the z axis. The wavefront of a Bessel beam in the paraxial approximation is determined by the relation $(m_\gamma - \lambda)\phi + k_z z - \omega t = 0$ and represents a helical (or twisted) structure because of the azimuthal ϕ dependence, which is missing for plane waves [cf. Fig. 2.2 (b)]. The transverse (xy) intensity

profile of twisted Bessel beams is determined by the z-component of the Poynting vector $S_z^{\mathrm{B}}(\boldsymbol{r}) \sim J_{m_\gamma-\lambda}^2(\varkappa r_\perp)$ and exhibits a ringlike pattern whose example is shown in Fig. 2.2 (c), where the orange and blue rings refer to high and low intensity in line with the maxima and zeros of the Bessel function. This is again in contrast to plane-wave radiation with a homogeneous intensity profile.

2.2.3 Angular momentum of Bessel photons

Let us now discuss the angular momentum features of twisted photons prepared in the Bessel state. To do this, apart from the SAM operator $\hat{S}_z$, we introduce the operator $\hat{L}_z$ for z-component of the orbital angular momentum and the operator $\hat{J}_z$ for z-component of the total angular momentum (TAM)

$$\hat{L}_z = -i\frac{\partial}{\partial\phi}\,, \quad \hat{J}_z = \hat{L}_z + \hat{S}_z\,. \tag{2.19}$$

Equation (2.18) implies that the vector potential of a Bessel beam in the paraxial approximation is a simultaneous eigenfunction of $\hat{L}_z$, $\hat{S}_z$, and $\hat{J}_z$

$$\hat{L}_z\boldsymbol{A}^{\mathrm{B}} = (m_\gamma - \lambda)\boldsymbol{A}^{\mathrm{B}}\,, \quad \hat{S}_z\boldsymbol{A}^{\mathrm{B}} = \lambda\boldsymbol{A}^{\mathrm{B}}\,, \quad \hat{J}_z\boldsymbol{A}^{\mathrm{B}} = m_\gamma\boldsymbol{A}^{\mathrm{B}}\,. \tag{2.20}$$

Thus each photon of a Bessel beam with a small opening angle θ_k is characterized not only by the helicity λ, just as in the case of plane waves, but also by the OAM $m_\gamma - \lambda$ and TAM m_γ projections on the propagation z axis. However, when the opening angle θ_k is large (the nonparaxial regime), Bessel beam do not possesses well-defined OAM and SAM projections, since the vector potential (2.16) is a superposition of three terms with different OAM $m_\gamma - m_s$ as well as SAM m_s. In fact, Eq. (2.16) shows us that only the TAM m_γ is the same for each term, and therefore only the projection m_γ of the total angular momentum is well defined for a nonparaxial Bessel beam of light.

2.3 Laguerre-Gaussian beams

2.3.1 Laguerre-Gaussian beam in position space and its properties

At this point we might consider another example of twisted beams, namely the Laguerre-Gaussian beam of light. Unlike vector potentials of plane waves and Bessel
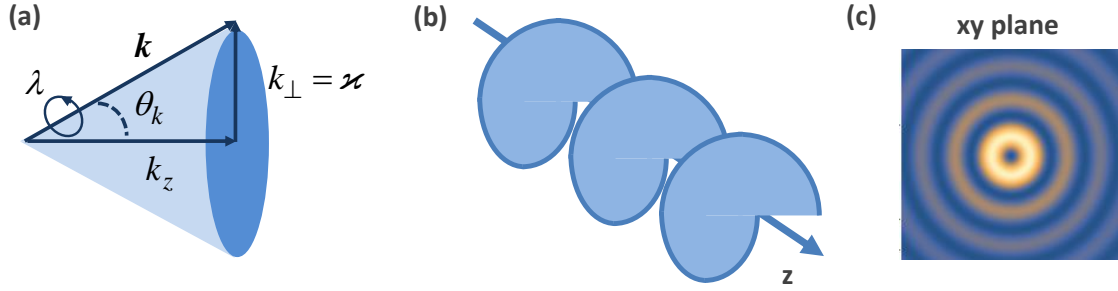
Figure 2.2: (a) In momentum space, a Bessel beam can be seen as a coherent superposition of plane waves with wave vectors $\boldsymbol{k}$ lying on a cone with an opening angle $\theta_k = \arctan(\varkappa/k_z)$ and with polarization vectors $\boldsymbol{e}_{\boldsymbol{k}\lambda}$ perpendicular to $\boldsymbol{k}$. (b) Bessel beam possesses a helical or twisted wavefront. (c) Transverse intensity profile of Bessel beams comprises a central dark spot and an infinite number of rings.

beams given in Coulomb gauge, the vector potential of Laguerre-Gaussian beams is usually expressed in Lorenz gauge $\boldsymbol{A}^{\mathrm{LG(L)}}$ indicated here by the superscript L (Allen *et al* 1992). For a complete description of the beam, one also needs the scalar potential $\Phi^{\mathrm{LG(L)}}$ in this case that is related to the vector potential $\boldsymbol{A}^{\mathrm{LG(L)}}$ by the Lorenz gauge condition (Johnson 2007)

$$\nabla \cdot \boldsymbol{A}^{\mathrm{LG(L)}} - \frac{ik}{c}\Phi^{\mathrm{LG(L)}} = 0 \,. \tag{2.21}$$

The equations for the electric and magnetic fields in Lorenz gauge then become

$$\boldsymbol{E} = -\nabla\Phi^{\mathrm{LG(L)}} + i\omega\boldsymbol{A}^{\mathrm{LG(L)}} = i\omega \left[\frac{\nabla(\nabla \cdot \boldsymbol{A}^{\mathrm{LG(L)}})}{k^2} + \boldsymbol{A}^{\mathrm{LG(L)}} \right] \,,$$
$$\boldsymbol{B} = \nabla \times \boldsymbol{A}^{\mathrm{LG(L)}} \,, \tag{2.22}$$

where we have used Eq. (2.21). Consider a circularly polarized Laguerre-Gaussian beam propagating primarily along the z direction whose vector potential can be written in the form

$$\boldsymbol{A}^{\mathrm{LG(L)}}(\boldsymbol{r}) = \boldsymbol{\varepsilon}_\lambda\, u(\boldsymbol{r})e^{ikz} \,, \tag{2.23}$$

where the polarization vector $\boldsymbol{\varepsilon}_\lambda$ orthogonal to the z axis is given by Eq. (2.4). If the amplitude distribution $u(\boldsymbol{r})$ changes slowly with distance z and this z dependence is slow compared to variations of $u(\boldsymbol{r})$ in the transverse direction, the paraxial

approximation is valid (Siegman 1986)

$$\left| \frac{\partial^2 u}{\partial z^2} \right| \ll \left| 2k \frac{\partial u}{\partial z} \right|, \quad \left| \frac{\partial^2 u}{\partial z^2} \right| \ll \left| \nabla_\perp^2 u \right|. \tag{2.24}$$

On substituting the vector potential (2.23) into the Helmholtz equation (2.1) and applying the paraxial approximation (2.24), we find that the amplitude distribution $u(\boldsymbol{r})$ satisfies the paraxial wave equation

$$\nabla_\perp^2 u + 2ik \frac{\partial u}{\partial z} = 0. \tag{2.25}$$

In the paraxial approximation, Laguerre-Gaussian light beam is described by the following amplitude distribution (Allen *et al* 1992)

$$u(r_\perp, \phi, z) = \frac{1}{w(z)} \left(\frac{\sqrt{2} r_\perp}{w(z)} \right)^m \exp \left[-\frac{r_\perp^2}{w^2(z)} \right] L_p^m \left(\frac{2r_\perp^2}{w^2(z)} \right)$$

$$\times \exp \left[im\phi + \frac{ikr_\perp^2 z}{2(z^2 + z_R^2)} - i(2p + m + 1) \arctan \left(\frac{z}{z_R} \right) \right], \quad (2.26)$$

which is a solution of Eq. (2.25). Here L_p^m refers to the associated Laguerre polynomial and w_0 denotes the beam waist, which determines both the width $w(z) = w_0 \sqrt{1 + z^2/z_R^2}$ and the Rayleigh range $z_R = kw_0^2/2$ of the beam. As was the case with Bessel beams in the paraxial regime, the vector potential of Laguerre-Gaussian beam is an eigenfunction of $\hat{L}_z$, $\hat{S}_z$, and $\hat{J}_z$, so that

$$\hat{L}_z \boldsymbol{A}^{\mathrm{LG(L)}} = m \boldsymbol{A}^{\mathrm{LG(L)}}, \quad \hat{S}_z \boldsymbol{A}^{\mathrm{LG(L)}} = \lambda \boldsymbol{A}^{\mathrm{LG(L)}}, \quad \hat{J}_z \boldsymbol{A}^{\mathrm{LG(L)}} = (m + \lambda) \boldsymbol{A}^{\mathrm{LG(L)}}. \tag{2.27}$$

Therefore, a photon in the Laguerre-Gaussian state carries the OAM projection m, helicity λ, and TAM projection $m + \lambda$. Such photons are again twisted since they have a helical wavefront defined by $m\phi + kz - \omega t = 0$ [cf. Fig. 2.4 (b)]. For the sake of simplicity, we here suppose that the OAM projection m is positive. It is worth stressing that the transverse intensity profile of a Laguerre-Gaussian beam is characterized by the amplitude distribution $S_z^{\mathrm{LG}}(\boldsymbol{r}) \sim |u(r_\perp)|^2$ (Haus 1984) and exhibits a ringlike pattern with a finite number of rings determined by the radial index p due to the properties of L_p^m [cf. Fig. 2.4 (c)]. This is in contrast to Bessel beams with an infinite number of rings. Moreover, the width of Laguerre-Gaussian beams changes on propagation with the minimum at the focus $z = 0$, while the width of Bessel beams does not depend on z.
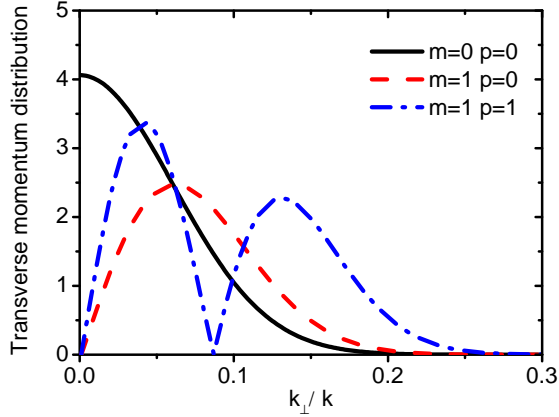
Figure 2.3: Comparison of the transverse momentum distribution $|v_{pm}(k_\perp)|$ for Laguerre-Gaussian beams with different radial indices p and OAM m. Results in arbitrary units are shown for waist $w_0 = 2.7\,\mu\text{m}$ and photon energy $\hbar\omega = 1.699$ eV.

2.3.2 Laguerre-Gaussian beam as a superposition of plane waves

To facilitate our later discussion, it is convenient to represent the vector potential of a Laguerre-Gaussian beam as a superposition of plane waves

$$\boldsymbol{A}^{\text{LG(L)}}(\boldsymbol{r}) = \int U_0(\boldsymbol{k}_\perp)\,\boldsymbol{\varepsilon}_\lambda e^{i\boldsymbol{kr}}\,d^2\boldsymbol{k}_\perp \tag{2.28}$$

with the momentum vector $\boldsymbol{k} = (k_\perp \cos\phi_k,\, k_\perp \sin\phi_k,\, k_z)$ while its modulus $k = \sqrt{k_\perp^2 + k_z^2}$ is kept fixed. These plane waves propagate at small opening angles $\theta_k = \arctan(k_\perp/k_z)$ with regard to the beam (z) axis in order to fulfill the paraxial approximation (2.24). The wave amplitude $U_0(\boldsymbol{k}_\perp)$ represents the momentum distribution within the beam and can be found when comparing Eq. (2.23) with (2.28) at $z = 0$. It then becomes clear that the wave amplitude $U_0(\boldsymbol{k}_\perp)$ is just the Fourier transform of the amplitude distribution $u(r_\perp, \phi, z)$ at the beam focus ($z = 0$ plane) and is given by

$$U_0(\boldsymbol{k}_\perp) = \frac{1}{(2\pi)^2} \int u(r_\perp, \phi, z = 0)e^{-i\boldsymbol{k}_\perp \boldsymbol{r}_\perp}\,d^2\boldsymbol{r}_\perp\,. \tag{2.29}$$

Therefore, the knowledge of the wave amplitude $U_0(\boldsymbol{k}_\perp)$ is sufficient in order to reconstruct the vector potential of the beam in the entire space. To further simplify $U_0(\boldsymbol{k}_\perp)$, we carry out the integration over the azimuthal angle ϕ in Eq. (2.29) by making use of the integral representation of the Bessel function (2.15). The remaining integration over the radius $r_\perp$ can be performed by using an explicit expression

for the associated Laguerre polynomials (Abramowitz and Stegun 1964)

$$L_p^m \left(\frac{2r_\perp^2}{w_0^2} \right) = \sum_{\beta=0}^{p} \frac{(-1)^\beta}{\beta!} \binom{p+m}{p-\beta} \left(\frac{2r_\perp^2}{w_0^2} \right)^\beta , \tag{2.30}$$

and formula (Lebedev 1965)

$$\int_0^\infty \left(\frac{r_\perp^2}{w_0^2} \right)^{\beta+m/2} J_m(k_\perp r_\perp) \, e^{-r_\perp^2/w_0^2} \, r_\perp \, dr_\perp$$
$$= \frac{w_0^2 \beta!}{2} e^{-k_\perp^2 w_0^2/4} \left(\frac{k_\perp w_0}{2} \right)^m L_\beta^m \left(\frac{k_\perp^2 w_0^2}{4} \right) . \tag{2.31}$$

With these algebraic manipulations, the wave amplitude $U_0(\boldsymbol{k}_\perp)$ for Laguerre-Gaussian beams can be written as (Cerjan and Cerjan 2011)

$$U_0(\boldsymbol{k}_\perp) = v_{pm}(k_\perp) \, e^{im\phi_k} , \tag{2.32}$$

and where the distribution

$$v_{pm}(k_\perp) = \frac{(-i)^m w_0}{4\pi} e^{-k_\perp^2 w_0^2/4} \left(\frac{k_\perp w_0}{2} \right)^m$$
$$\times \sum_{\beta=0}^{p} (-1)^\beta 2^{\beta+m/2} \binom{p+m}{p-\beta} L_\beta^m \left(\frac{k_\perp^2 w_0^2}{4} \right) \tag{2.33}$$

now only depends on the modulus of the transverse momentum. Fig. 2.3 displays the transverse momentum distribution $|v_{pm}(k_\perp)|$ for the beams with different OAM m and radial indices p. As seen from this figure, Laguerre-Gaussian beam always consists of plane waves with different transverse momenta $k_\perp$ and, hence, different opening angles $\theta_k = \arctan(k_\perp/k_z)$ with respect to the propagation z direction as shown in Fig. 2.4 (a). On the other hand, a Bessel beam can be considered also as a superposition of plane waves propagating at some fixed opening angle θ_k, because its wave amplitude is proportional to the Dirac delta function $a_{\varkappa m_\gamma}(\boldsymbol{k}_\perp) \sim \delta(k_\perp - \varkappa)$. From the discussion above we see that the polarization vector $\boldsymbol{\varepsilon}_\lambda$ of the plane waves in Eq. (2.28) is not always perpendicular to the wave vector $\boldsymbol{k}$. In this case, the divergence of the vector potential $\boldsymbol{A}^{\mathrm{LG(L)}}$ does not vanish, and hence the scalar potential $\Phi^{\mathrm{LG(L)}}$ is not zero in Lorenz gauge. Because of this non-zero scalar potential the Lorenz gauge is less convenient for atomic calculations than the Coulomb gauge (indicated by the superscript C), in which the scalar potential vanishes. To derive the vector potential $\boldsymbol{A}^{\mathrm{LG(C)}}$ in Coulomb gauge, we compare the equation for the electric

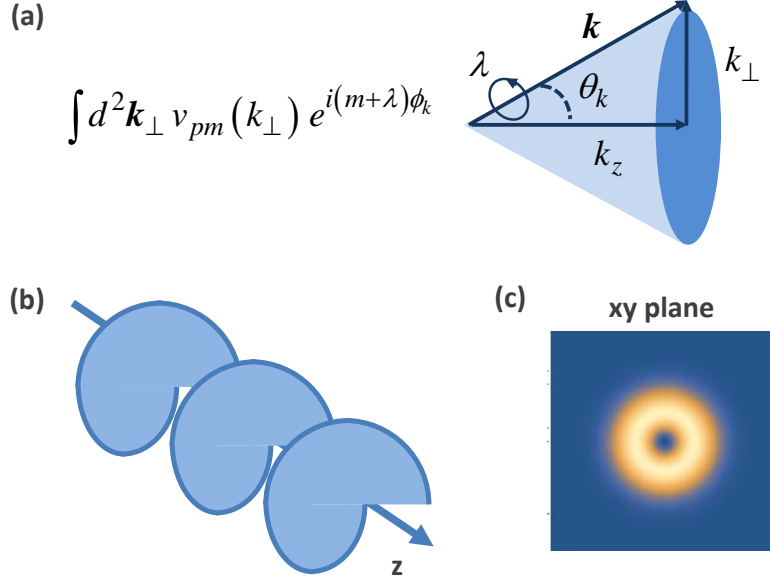$$\int d^2 \boldsymbol{k}_\perp \, v_{pm}(k_\perp) \, e^{i(m+\lambda)\phi_k}$$

Figure 2.4: (a) In momentum space, the Laguerre-Gaussian beam is a superposition of plane waves with momenta $\boldsymbol{k}$ lying on cones with opening angles $\theta_k = \arctan(k_\perp/k_z)$. The contributions from different opening angles θ_k are determined by $v_{pm}(k_\perp)e^{i(m+\lambda)\phi_k}$. (b) Laguerre-Gaussian beam has a helical wavefront. (c) Its transverse intensity profile comprises a central dark spot and a finite number of rings.

field in Lorenz gauge (2.22) with the equation for the electric field in Coulomb gauge $\boldsymbol{E} = i\omega \boldsymbol{A}^{\mathrm{LG(C)}}$ and find the relationship between the vector potentials in two different gauges

$$\boldsymbol{A}^{\mathrm{LG(C)}} = \frac{\nabla(\nabla \cdot \boldsymbol{A}^{\mathrm{LG(L)}})}{k^2} + \boldsymbol{A}^{\mathrm{LG(L)}} \,. \tag{2.34}$$

Since in the paraxial approximation the Laguerre-Gaussian beam contains only plane waves with small opening angles $\theta_k = \arctan(k_\perp/k_z)$, we can approximate the wave vector (2.11) by

$$\boldsymbol{k} \approx \begin{pmatrix} k\theta_k \cos\phi_k \\ k\theta_k \sin\phi_k \\ k\left(1 - \theta_k^2/2\right) \end{pmatrix} \,. \tag{2.35}$$

Let us apply this approximation to the vector potential in Lorenz gauge and substitute its integral formula (2.28) into Eq. (2.34). Up to terms of order θ_k, the vector

potential of a Laguerre-Gaussian beam in Coulomb gauge is then given by

$$\boldsymbol{A}^{\text{LG(C)}}(\boldsymbol{r}) \approx \int v_{pm}(k_\perp)\, e^{i(m+\lambda)\phi_k} \left[e^{-i\lambda\phi_k}\boldsymbol{\varepsilon}_\lambda + \frac{\lambda}{\sqrt{2}}\, \theta_k\, \boldsymbol{\varepsilon}_0 \right] e^{i\boldsymbol{k}\boldsymbol{r}} d^2\boldsymbol{k}_\perp \,. \qquad (2.36)$$

Here the longitudinal (z) component of the field arises from the contribution of the scalar potential in Lorenz gauge (Davis 1979). To better understand the square bracket in the equation above, let us consider the polarization vector $\boldsymbol{e}_{\boldsymbol{k}\lambda}$ given by Eq. (2.12). In contrast to the polarization vector $\boldsymbol{\varepsilon}_\lambda$ in Eq. (2.4), the vector $\boldsymbol{e}_{\boldsymbol{k}\lambda}$ is always orthogonal to the momentum $\boldsymbol{k}$. For the plane waves with small opening angle θ_k with regard to the z axis, the polarization vector $\boldsymbol{e}_{\boldsymbol{k}\lambda}$ is approximately equal to the square bracket term in Eq. (2.36) up to terms of order θ_k. As a result, the vector potential of Laguerre-Gaussian beam in Coulomb gauge is written as

$$\boldsymbol{A}^{\text{LG(C)}}(\boldsymbol{r}) = \int v_{pm}(k_\perp)\, e^{i(m+\lambda)\phi_k}\, \boldsymbol{e}_{\boldsymbol{k}\lambda}\, e^{i\boldsymbol{k}\boldsymbol{r}}\, d^2\boldsymbol{k}_\perp \,. \qquad (2.37)$$

As seen from this expression, the circularly polarized Laguerre-Gaussian beam can be understood as a superposition of circularly polarized plane waves $\boldsymbol{e}_{\boldsymbol{k}\lambda}\, e^{i\boldsymbol{k}\boldsymbol{r}}$ with the amplitude $v_{pm}(k_\perp)\, e^{i(m+\lambda)\phi_k}$. The formula (2.37) for Laguerre-Gaussian beams is the analogue of the expression (2.13) for Bessel beams and will be used in further derivations.

3 Ionization of H_2^+ molecular ions by Bessel beam

Like in Young's well-known double-slit experiment with plane-wave light, interference effects can be observed also in the photoionization of diatomic molecules (Walter and Briggs 1999). The interference pattern in the photoelectron angular distribution arises from the phase shift of the electrons emitted from different atomic centers of the molecule. This phenomenon was first analyzed by Cohen and Fano (1966) almost half a century ago in the ionization of H_2^+ molecular ions with incident plane-wave radiation. In this chapter we study the photoionization of H_2^+ by twisted Bessel beams. We begin with a derivation of the transition matrix element describing the ionization process. Using this matrix element, the cross sections and angular distributions of the emitted photoelectrons are then analyzed. Our calculations show that the known oscillations in the angular and energy distributions of photoelectrons, as they were confirmed in experiments with plane-wave radiation (Akoury *et al* 2007), become much less pronounced for twisted light. This happens especially at higher photon energies when the variations in the intensity profile of the beams become comparable to the size of the molecule.

3.1 Theory of photoionization of H_2^+ molecular ions

We begin with the general transition amplitude that describes the photoionization of a H_2^+ molecular ion, which consists of just two nuclei (protons) and a single electron. In nonrelativistic first-order perturbation theory, the differential and total photoionization cross sections are usually expressed in terms of the matrix element (Bransden and Joachain 2003)

$$M_{fi} = \int \psi_f^*(\boldsymbol{r})\, \boldsymbol{A}(\boldsymbol{r}) \cdot \hat{\boldsymbol{p}}\, \psi_i(\boldsymbol{r})\, d^3\boldsymbol{r}\,, \tag{3.1}$$

that describes the transition of the electron from its initial bound state ψ_i into the final continuum state ψ_f because of the absorption of an incident photon. Here $\hat{\boldsymbol{p}} = -i\nabla$ is the momentum operator, and the vector potential $\boldsymbol{A}(\boldsymbol{r})$ characterizes the properties of the photons. In order to calculate the transition amplitude (3.1), we need to know the explicit form of the wave functions of the electron in its initial
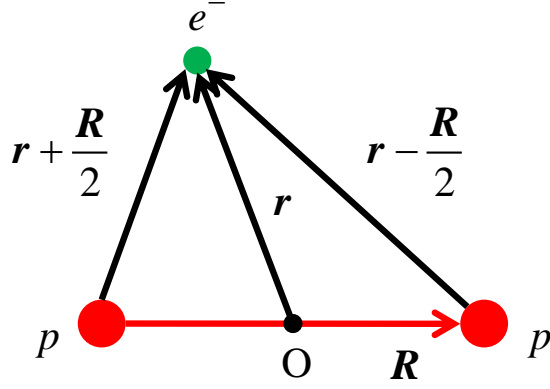
Figure 3.1: Coordinates that are used to describe the hydrogen molecular ion H_2^+. If the origin is chosen at the midpoint of the internuclear axis, the position vector $\boldsymbol{r}$ of the electron can easily be written also in terms of the positions of the two nuclei as $\boldsymbol{r} \pm \boldsymbol{R}/2$.

and final states. As usual, we construct the initial wave function ψ_i of the $1\sigma_g$ molecular ground state as linear combination of atomic orbitals

$$\psi_i(\boldsymbol{r}) = \frac{1}{\sqrt{2}}[\psi_{1s}(\boldsymbol{r} - \boldsymbol{R}/2) + \psi_{1s}(\boldsymbol{r} + \boldsymbol{R}/2)], \tag{3.2}$$

where ψ_{1s} denotes the $1s$ ground state orbital of atomic hydrogen. Moreover, $\boldsymbol{R}$ is the internuclear vector from the first to the second proton, and $\boldsymbol{r}$ is the position vector of the electron with regard to the origin of the coordinates as shown in Fig. 3.1]. In the first-order Born approximation, which is applied in this work, a plane wave

$$\psi_f(\boldsymbol{r}) = (2\pi)^{-3/2}\, e^{i\boldsymbol{p}_f \boldsymbol{r}} \tag{3.3}$$

is supposed for the outgoing electron with momentum $\boldsymbol{p}_f$ in the matrix element (3.1). This approximation is valid when the kinetic energy T_f of the emitted electron is large compared to its interaction with the remaining nuclei, but much smaller than the rest energy of the electron,

$$I_p \ll T_f \ll m_e c^2. \tag{3.4}$$

In addition, the photon energy ω, ionization potential I_p of the H_2^+ molecular ion, and the modulus of the momentum are related to each other by

$$T_f = \frac{p_f^2}{2} = \omega - I_p \tag{3.5}$$

due to energy conservation.

3.1.1 Transition matrix element for plane-wave photons

The ionization of H_2^+ molecular ions by a plane wave has been discussed in good detail; see, for example, Baltenkov *et al* (2012). Here we may therefore restrict ourselves to a rather short account of the basic formulas. If we insert the vector potential $\boldsymbol{A}(\boldsymbol{r}) = \boldsymbol{e}_{k\lambda} \, e^{i\boldsymbol{kr}}$ for plane-wave light with photon energy $\omega = ck$ and helicity λ into Eq. (3.1), we then obtain the transition amplitude

$$M_{fi}^{\mathrm{pl}}(\boldsymbol{k}) = -i \int \psi_f^*(\boldsymbol{r}) e^{i\boldsymbol{kr}} \, \boldsymbol{e}_{k\lambda} \cdot \nabla \, \psi_i(\boldsymbol{r}) \, d^3\boldsymbol{r} \,. \tag{3.6}$$

Upon integration by parts, we find that

$$M_{fi}^{\mathrm{pl}}(\boldsymbol{k}) = i \int \boldsymbol{e}_{k\lambda} \, \psi_i(\boldsymbol{r}) \cdot \nabla \left[\psi_f^*(\boldsymbol{r}) \, e^{i\boldsymbol{kr}} \right] d^3\boldsymbol{r} \,. \tag{3.7}$$

Hence, the transition amplitude can be written as

$$M_{fi}^{\mathrm{pl}}(\boldsymbol{k}) = -\frac{\boldsymbol{e}_{k\lambda} \cdot \boldsymbol{p}_f}{(2\pi)^{3/2}} \int e^{i(\boldsymbol{k} - \boldsymbol{p}_f)\boldsymbol{r}} \, \psi_i(\boldsymbol{r}) \, d^3\boldsymbol{r} \,, \tag{3.8}$$

where we have employed the final-state wave function (3.3) and the orthogonality between the polarization and the wave vectors of a photon, $\boldsymbol{e}_{k\lambda} \cdot \boldsymbol{k} = 0$. We can further apply the initial wave function (3.2) as well as the well-known Fourier transform of the hydrogenic $1s$ ground state (Bransden and Joachain 2003)

$$\int e^{i(\boldsymbol{k} - \boldsymbol{p}_f)\boldsymbol{r}} \, \psi_{1s}(\boldsymbol{r}) \, d^3\boldsymbol{r} = \frac{8\sqrt{\pi}}{[(\boldsymbol{k} - \boldsymbol{p}_f)^2 + 1]^2} \,, \tag{3.9}$$

to finally obtain the transition amplitude for the photoionization of H_2^+ molecular ions as

$$M_{fi}^{\mathrm{pl}}(\boldsymbol{k}) = -\frac{4}{\pi} \frac{\boldsymbol{e}_{k\lambda} \cdot \boldsymbol{p}_f}{[(\boldsymbol{k} - \boldsymbol{p}_f)^2 + 1]^2} \cos\left[\frac{(\boldsymbol{k} - \boldsymbol{p}_f) \cdot \boldsymbol{R}}{2} \right] \,. \tag{3.10}$$

In fact, the matrix element (3.10) will be utilized below to obtain all properties of the photoionization process with twisted light.

3.1.2 Transition matrix element for Bessel beams

To analyze the ionization of H_2^+ molecular ions by a twisted Bessel beam, we substitute its vector potential (2.13) into the transition amplitude (3.1). In the previous chapter we have seen that, in contrast to an incident plane wave, the Bessel beam has an inhomogeneous intensity distribution perpendicular to its propagation direction, i.e. in the xy plane for the given geometry. It was furthermore shown that this profile has a concentric ring structure, and therefore the photoionization will depend on the position of the H_2^+ molecular ion with regard to the beam axis. Here we shall use the impact parameter $\boldsymbol{b}$ in order to designate the origin of the molecular coordinates with regard to the beam axis [cf. Fig. 3.2]. With this notation, the initial wave function of the electron is written as

$$\psi_i(\boldsymbol{r}, \boldsymbol{b}) = \frac{1}{\sqrt{2}} \left[\psi_{1s}(\boldsymbol{r} - \boldsymbol{R}/2 - \boldsymbol{b}) + \psi_{1s}(\boldsymbol{r} + \boldsymbol{R}/2 - \boldsymbol{b}) \right]. \tag{3.11}$$

Using this wave function, the transition amplitude for the ionization of the H_2^+ molecular ions by a Bessel beam can be expressed as

$$M_{fi}^{\text{tw}}(\boldsymbol{k}, \boldsymbol{b}) = -i \int \frac{d^2 \boldsymbol{k}_\perp}{(2\pi)^2} \, a_{\varkappa m_\gamma}(\boldsymbol{k}_\perp) \int d^3 \boldsymbol{r} \, \psi_f^*(\boldsymbol{r}) e^{i\boldsymbol{k}\boldsymbol{r}} \, \boldsymbol{e}_{\boldsymbol{k}\lambda} \cdot \nabla \, \psi_i(\boldsymbol{r}, \boldsymbol{b}). \tag{3.12}$$

This amplitude can be evaluated quite similarly to the plane-wave case [cf. Eqs. (3.6)-(3.10)]

$$M_{fi}^{\text{tw}}(\boldsymbol{k}, \boldsymbol{b}) = -\frac{4}{\pi} \int a_{\varkappa m_\gamma}(\boldsymbol{k}_\perp) \, e^{i(\boldsymbol{k}-\boldsymbol{p}_f)\boldsymbol{b}} \, \frac{\boldsymbol{e}_{\boldsymbol{k}\lambda} \cdot \boldsymbol{p}_f}{[(\boldsymbol{k} - \boldsymbol{p}_f)^2 + 1]^2}$$

$$\times \cos \left[\frac{(\boldsymbol{k} - \boldsymbol{p}_f) \cdot \boldsymbol{R}}{2} \right] \frac{d^2 \boldsymbol{k}_\perp}{(2\pi)^2} = \int a_{\varkappa m_\gamma}(\boldsymbol{k}_\perp) \, e^{i(\boldsymbol{k}-\boldsymbol{p}_f)\boldsymbol{b}} \, M_{fi}^{\text{pl}}(\boldsymbol{k}) \, \frac{d^2 \boldsymbol{k}_\perp}{(2\pi)^2}, \tag{3.13}$$

and, hence, in terms of the plane-wave transition amplitude $M_{fi}^{\text{pl}}(\boldsymbol{k})$ in Eq. (3.10).

3.1.3 Photoionization cross section for macroscopic target

We can apply the amplitude (3.13) to evaluate the differential photoionization cross section. In contrast to an incident plane wave with a constant flux (per unit area), the cross section for Bessel beams depends on the particular geometry under which the incident beam interacts with the target molecules. For instance, if we assume a macroscopic target of initially aligned molecules, that are uniformly distributed in their impact parameter $\boldsymbol{b}$ over the extent of the Bessel beam with radius R_{tw},
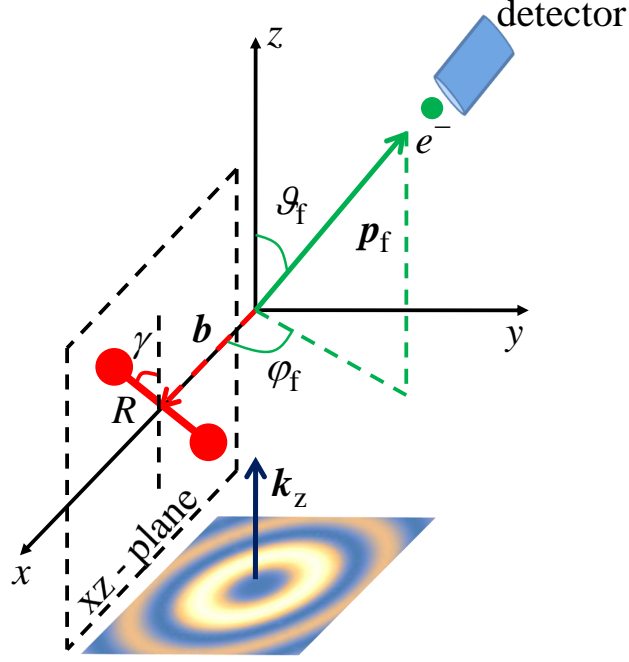
Figure 3.2: Geometry for the ionization of H_2^+ molecules by twisted light. While the quantization (z) axis is taken along the propagation direction of the incident beam, the H_2^+ molecular ion is supposed to lay in the xz plane. Moreover, the molecule is aligned with angle γ with respect to the z axis and its center of mass, i.e. the origin of the intermolecular coordinates, is displaced by the impact parameter $\boldsymbol{b}$ from the beam axis. Finally, the two angles ϑ_f and φ_f describe the detector for observing the emitted photoelectrons.

the angle-differential cross section can be determined explicitly by calculating the integral for just $b < R_{\text{tw}}$,

$$\frac{d\sigma^{\text{tw}}}{d\Omega_f} = \frac{2\pi p_f}{j^{\text{tw}}} \int |M_{fi}^{\text{tw}}(\boldsymbol{k}, \boldsymbol{b})|^2 \, \frac{d^2\boldsymbol{b}}{\pi R_{\text{tw}}^2} = \frac{4\pi^4 \alpha p_f R_{\text{tw}}}{\omega \cos\theta_k} \int e^{i(\boldsymbol{k}_\perp - \boldsymbol{k}'_\perp)\boldsymbol{b}}$$

$$\times \, a_{\varkappa m_\gamma}(\boldsymbol{k}_\perp) \, a_{\varkappa m_\gamma}^*(\boldsymbol{k}'_\perp) \, M_{fi}^{\text{pl}}(\boldsymbol{k}) \, M_{fi}^{\text{pl}\,*}(\boldsymbol{k}') \, \frac{d^2\boldsymbol{k}_\perp}{(2\pi)^2} \frac{d^2\boldsymbol{k}'_\perp}{(2\pi)^2} \frac{d^2\boldsymbol{b}}{\pi R_{\text{tw}}^2} \,, \tag{3.14}$$

where $j^{\text{tw}} = \omega \cos\theta_k / (2\pi^3 R_{\text{tw}}\,\alpha)$ denotes the flux of the incident Bessel radiation (Scholz-Marggraf *et al* 2014). As seen from Eq. (3.14), the integral over the impact parameter $\boldsymbol{b}$ is proportional to the delta-function $\delta(\boldsymbol{k}'_\perp - \boldsymbol{k}_\perp)$ due to the factor $\exp[i(\boldsymbol{k}_\perp - \boldsymbol{k}'_\perp)\boldsymbol{b}]$ in the integrand. Moreover, by carrying out the trivial integration

over $\boldsymbol{k}'_\perp$ and making use of Eqs. (3.10) and (2.14), we find

$$\frac{d\sigma^{\text{tw}}}{d\Omega_f} = \frac{32\pi a p_f}{\omega \cos\theta_k R_{\text{tw}}} \int \frac{\delta^2(k_\perp - \varkappa)}{\varkappa} \frac{|\boldsymbol{e}_{\boldsymbol{k}\lambda} \cdot \boldsymbol{p}_f|^2}{[(\boldsymbol{k} - \boldsymbol{p}_f)^2 + 1]^4}$$
$$\times \{1 + \cos[(\boldsymbol{k} - \boldsymbol{p}_f) \cdot \boldsymbol{R}]\} \frac{d^2\boldsymbol{k}_\perp}{2\pi}. \tag{3.15}$$

Furthermore, since we can treat the square of the δ-function as (Scholz-Marggraf *et al* 2014)

$$\delta^2(k_\perp - \varkappa) = \frac{R_{\text{tw}}}{\pi} \delta(k_\perp - \varkappa), \tag{3.16}$$

the integration over $k_\perp$ in Eq. (3.15) gives rise to $k_\perp = \varkappa$, and the angle-differential cross section for the photoionization of aligned H_2^+ molecular ions becomes

$$\frac{d\sigma^{\text{tw}}}{d\Omega_f} = \frac{32\alpha p_f}{\omega \cos\theta_k} \int\limits_0^{2\pi} \frac{|\boldsymbol{e}_{\boldsymbol{k}\lambda} \cdot \boldsymbol{p}_f|^2}{[(\boldsymbol{k} - \boldsymbol{p}_f)^2 + 1]^4} \{1 + \cos[(\boldsymbol{k} - \boldsymbol{p}_f) \cdot \boldsymbol{R}]\} \frac{d\phi_k}{2\pi}. \tag{3.17}$$

If, in addition, we assume the emitted electron to be fast but still nonrelativistic [cf. Eq. (3.4)], we can rewrite $(\boldsymbol{k} - \boldsymbol{p}_f)^2 + 1 \approx p_f^2 + 1$ in the denominator of Eq. (3.17) and apply the integral representation of the Bessel function (2.15) in order to perform the integration over the angle ϕ_k in the cross section. With these substitutions, the angle-differential cross section for the photoionization of H_2^+ ions by a Bessel beam can be expressed in good approximation in terms of the angles (ϑ_f, φ_f) of the emitted electron as

$$\frac{d\sigma^{\text{tw}}}{d\Omega_f} \approx \frac{8\alpha p_f^3}{\omega \cos\theta_k} \frac{1}{[p_f^2 + 1]^4} \{[2\sin^2\vartheta_f + 2\sin^2\theta_k$$
$$- 3\sin^2\vartheta_f \sin^2\theta_k] [1 + J_0(R\varkappa\sin\gamma)\cos\eta]$$
$$+ \sin(2\theta_k)\sin(2\vartheta_f)\cos\varphi_f J_1(R\varkappa\sin\gamma)\sin\eta$$
$$+ \sin^2\vartheta_f \sin^2\theta_k \cos(2\vartheta_f) J_2(R\varkappa\sin\gamma)\cos\eta\}, \tag{3.18}$$

where η is given by

$$\eta = Rk_z\cos\gamma - Rp_f[\sin\gamma\sin\vartheta_f\cos\varphi_f + \cos\gamma\cos\vartheta_f]. \tag{3.19}$$

Here the z axis is chosen along the direction of the incident light, and we assumed the internuclear vector $\boldsymbol{R}$ to lay within the xz plane and to be tilted by the angle γ with regard to the z axis as shown in Fig. 3.2]. We note that, for $\varkappa = 0$ or zero
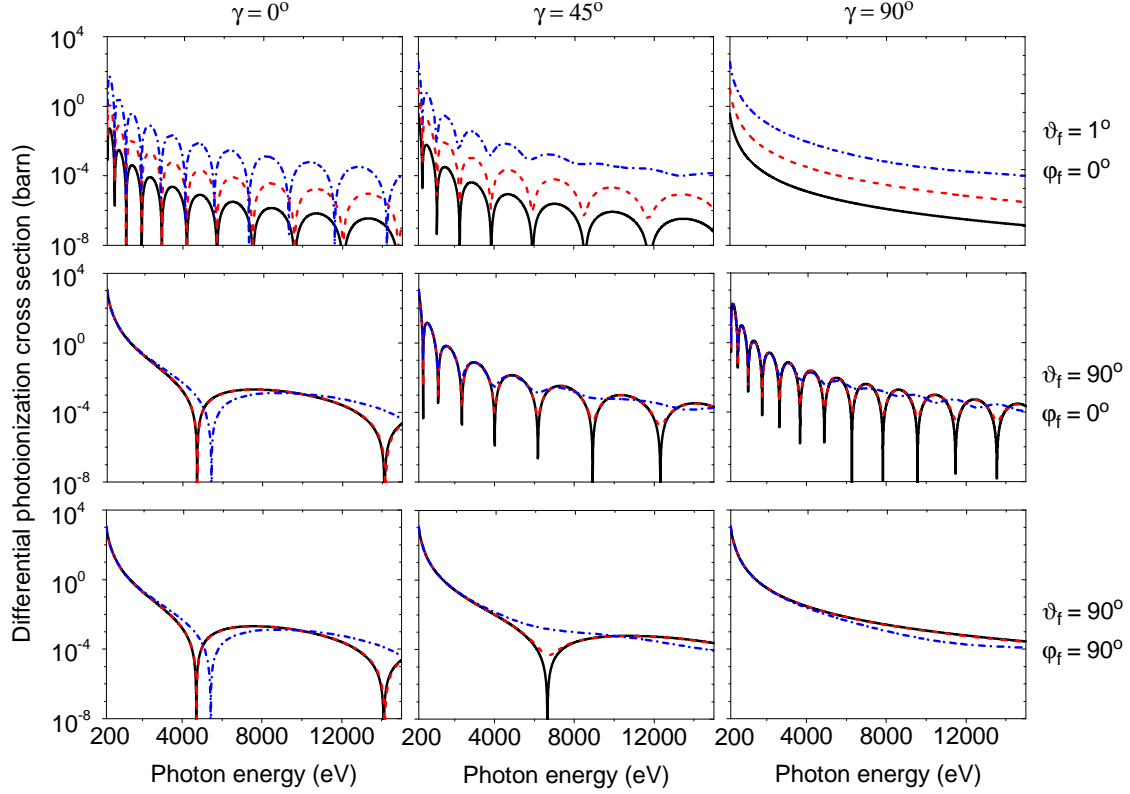
Figure 3.3: Angle-differential photoionization cross sections as a function of the photon energy of the incident light. Results are presented for selected angles (ϑ_f, φ_f) of the emitted electrons as well as for different orientations of the molecules. Cross sections for incident plane waves (black solid lines) are compared with those for Bessel beams with opening angles $\theta_k = 5°$ (red dashed lines) and $\theta_k = 30°$ (blue dash-dotted lines), respectively.

opening angle $\theta_k = 0°$, the expression (3.17) simply becomes the cross section for the ionization of H_2^+ ions by plane-wave radiation in agreement with the formal limit of a Bessel beam for $\theta_k = 0°$, i.e. for $\boldsymbol{k} \parallel z$.

3.2 Numerical results for H_2^+ molecular ions

3.2.1 Photoelectron energy distribution

We previously found that the angle-differential cross section for the photoionization of a macroscopic target of aligned but randomly distributed H_2^+ molecular ions by a Bessel beam is independent of its TAM projection m_γ. However, the cross section $d\sigma^{tw}/d\Omega_f$ obviously depends on the opening angle θ_k. This can be seen in Fig. 3.3,

in which the angle-differential cross section (3.17) is displayed as function of the photon energy. Results for an incident plane-wave radiation along the z axis are compared with Bessel beams with opening angles $\theta_k = 5°$ and $\theta_k = 30°$, respectively. Cross sections are shown for three selected pairs of angles (ϑ_f, φ_f) of the emitted photoelectrons [cf. the rows of Fig. 3.3]. In these computations, moreover, the H_2^+ molecular ions were assumed to be initially aligned along three different angles $\gamma = 0°$ (left column), $\gamma = 45°$ (middle column), and $\gamma = 90°$ (right column) with regard to the z axis.

In the left column of Fig. 3.3, in particular, the H_2^+ molecular ions are aligned along the direction of the incident light ($\gamma = 0°$). For this alignment, the plane-wave and twisted cross sections both oscillate and exhibit in general a rather similar behavior as function of the photon energy. These oscillations in the angle-differential cross sections, if taken as function of the photon energy, arise from the interference of the quantum amplitudes due to the photoionization of the electron from the two nuclear centers of the molecules. A destructive interference in the paths of the outgoing electron leads to the pronounced minima in the cross sections as discussed previously (Baltenkov *et al* 2012). For twisted Bessel light, the positions of these minima are shifted in general and now also depend on the opening angle θ_k of the beams.

More pronounced differences between the angle-differential cross sections for a plane wave and those for a Bessel beam are found if the molecular axis is tilted by some angle $\gamma \neq 0°$ with regard to the z axis. In the middle ($\gamma = 45°$) and right columns ($\gamma = 90°$) of Fig. 3.3, for example, the differential cross sections for the ionization by twisted light oscillate much less than for the plane-wave ionization, especially at high photon energies as well as for the large opening angles θ_k. An almost monotonic decrease of $d\sigma^{\mathrm{tw}}/d\Omega_f$ as function of energy is found for $\theta_k = 30°$ and $\vartheta_f = \varphi_f = 90°$. For plane waves, in contrast, a clear minimum in the cross section at $\hbar\omega = 6.5$ keV is still found for the same alignment of the molecules ($\gamma = 45°$).

This qualitative change in the angle-differential cross sections can be explained by the intensity profile of the Bessel beam. As mentioned in previous chapter, such an intensity profile exhibits a ringlike pattern as shown in Fig. 3.4. For sufficiently small photon energy, the size of these rings is much larger than the internuclear distance R [cf. the left panel of Fig. 3.4] and hence the atomic centers of the H_2^+ ions are effectively exposed to the same intensity of the incident radiation, like for plane waves also. The angle-differential cross sections therefore show for both plane-wave
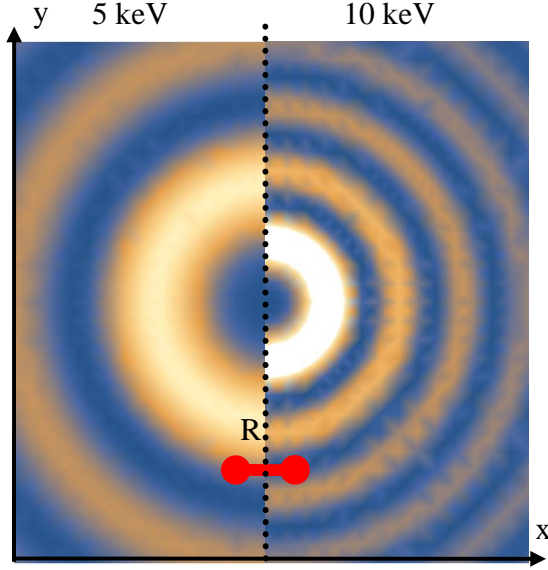
Figure 3.4: Transverse intensity profile of a Bessel beam with opening angle $\theta_k = 30°$, projection of the TAM $m_\gamma = 3$, helicity $\lambda = +1$, and for the two photon energies $\hbar\omega = 5$ keV (left panel) and $\hbar\omega = 10$ keV (right panel). For comparison, we also display the size of a H_2^+ molecular ion; see text for further discussion.

and twisted Bessel beams a quite similar energy behavior for all photon energies $\hbar\omega < 3$ keV. At higher photon energies, in contrast, the ringlike intensity varies over a smaller spatial extent and in particular for rather large opening angles θ_k, and the different nuclei are thus exposed to a different strength (intensity) of the radiation field. For this reason then, the interference pattern gradually disappear, similar to Young's experiment for double slits of nonequal widths.

3.2.2 Photoelectron angular distribution

So far, we have discussed the angle-differential cross section for the photoionization of H_2^+ ions as function of the photon energy but for fixed angles (ϑ_f, φ_f) of the emitted electrons. To analyze also the angular dependence of $d\sigma^{\mathrm{tw}}/d\Omega_f$, Fig. 3.5 displays the cross sections as function of polar angle ϑ_f of the photoelectrons for two different photon energies. In these computations, both the alignment $\gamma = 45°$ and azimuthal angle of the emitted electrons $\varphi_f = 0°$ are fixed. As seen from Fig. 3.5, the differential cross section $d\sigma^{\mathrm{tw}}/d\Omega_f$ does not longer vanish for $\vartheta_f = 0°$, in contrast to an incident plane wave. This effect can be explained by the polarization vector of twisted light, since the differential cross sections are always proportional to the
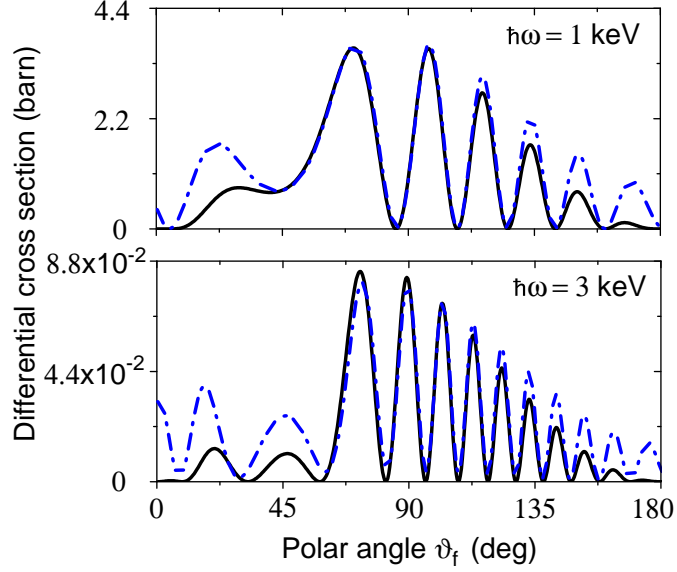
Figure 3.5: Angle-differential photoionization cross section as a function of the polar angle ϑ_f of the detector for H_2^+ molecular ions, aligned under the angle $\gamma = 45°$, and if the photoelectrons are observed in the xz plane ($\varphi_f = 0°$). Plane-wave results (black solid lines) are compared with the photoionization by means of a Bessel beam with opening angle $\theta_k = 30°$ (blue dash-dotted lines) and are shown for three different photon energies: $\hbar\omega = 1$ keV (upper panel), $\hbar\omega = 3$ keV (bottom panel), respectively.

scalar product of the polarization vector and the propagation direction of the emitted electrons. For plane waves with $\boldsymbol{k} \parallel z$, the polarization vector is perpendicular to the z axis and thus $|\boldsymbol{\varepsilon}_\lambda \cdot \boldsymbol{p}_f|^2 \sim \sin^2 \vartheta_f$ or the cross section is zero at $\vartheta_f = 0°$. For Bessel beams, in contrast, the polarization vector also has a non-zero z-component in forward direction $\vartheta_f = 0°$ and $d\sigma^{\mathrm{tw}}/d\Omega_f \neq 0$ in this case. For similar reasons, moreover, the cross section for twisted light is generally larger than for plane waves if $\vartheta_f = 1°$, as seen from the top row of Fig. 3.3.

Finally, we can consider the angle-differential cross sections $d\sigma^{\mathrm{tw}}/d\Omega_f$ also as function of the azimuthal angle φ_f of the emitted photoelectrons. In Fig. 3.6 we compare the corresponding angular distributions as functions of φ_f for plane waves (black solid lines) with those of Bessel beams with opening angle $\theta_k = 30°$ (blue dash-dotted lines). Here the H_2^+ molecular ions are assumed to be aligned again under the angle $\gamma = 45°$ with regard to the z axis. As seen from this figure, the cross sections for the Bessel beam and for the plane wave exhibit a quite similar φ_f dependence at small photon energies. For $\hbar\omega = 0.5$ keV, for example, the shapes of the angular
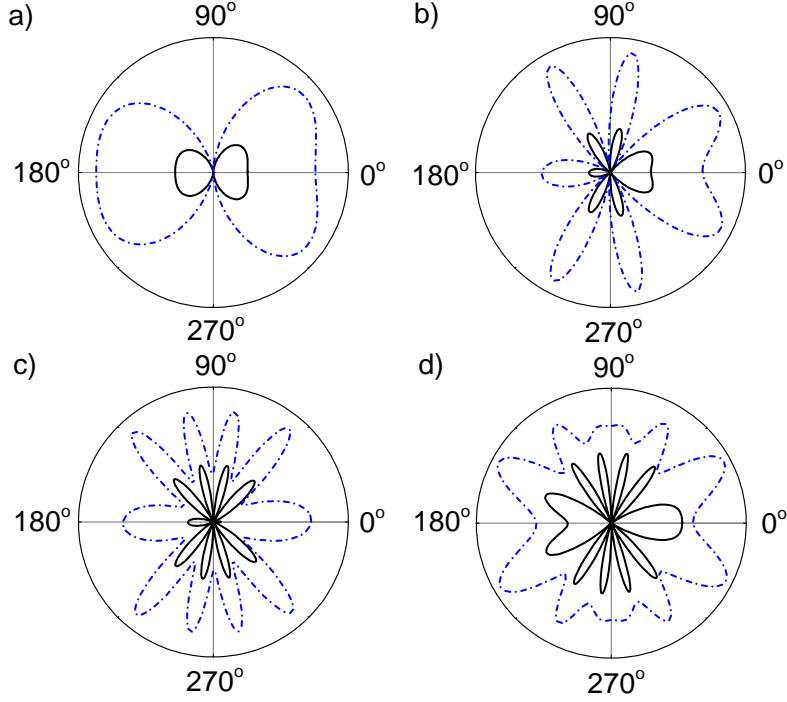
Figure 3.6: Comparison of the photoelectron angular distribution as function of the angle φ_f for incident plane waves (black solid lines) and Bessel beams with opening angle $\theta_k = 30°$ (blue dash-dotted lines). The H_2^+ molecular ions are assumed to be aligned again under the angle $\gamma = 45°$ with regard to the z axis. Results in arbitrary units are shown for four different photon energies: a) $\hbar\omega = 0.5$ keV; b) $\hbar\omega = 3$ keV; c) $\hbar\omega = 7$ keV; d) $\hbar\omega = 10$ keV. The polar angle of emitted electrons $\vartheta_f = 20°$ is fixed.

distribution are almost identical at the given polar angle $\vartheta_f = 20°$, apart from their absolute values [cf. Fig. 3.6(a)]. In particular, the electron emission vanishes for $\varphi_f = 90°$ for incident plane-wave radiation as well as for the Bessel beam. However, these two relative distributions start to deviate from each other if either the photon energies or the opening angle θ_k (not shown here in this figure) increases. For a photon energy of $\hbar\omega = 10$ keV, the Bessel beam results in a quite isotropic φ_f distribution of the emitted photoelectrons and in contrast to the well-defined lobes for plane-wave radiation of the same energy [cf. Fig. 3.6(d)]. Again, these modifications in the φ_f angular distribution can be understood from the intensity pattern of the corresponding Bessel beams, relative to the size of the H_2^+ molecular ions.

4 Excitation of mesoscopic atomic target by Bessel beam

More often than not, optical excitations refers to the transfer of an atom from a ground state to an upper state. For an incident plane-wave photon, the probability to find an atom in a particular magnetic sublevel of the upper state is determined by the well-known selection rules (Bransden and Joachain 2003). However, the selection rules and hence magnetic sublevel population of excited atomic states were found to be different when twisted light collides with a well-localized single atom (Afanasev *et al* 2013) or with a macroscopic (infinitely extended) target (Scholz-Marggraf *et al* 2014). In this chapter we shall investigate the excitation of a mesoscopic atomic target by twisted Bessel beams. The atoms are assumed to be confined and localized with nanometer precision in this target, corresponding to experiments on the excitation of atoms or ions in magneto-optical and Paul traps (Tabosa and Petrov 1999, Schmiegelow *et al* 2016). By using nonrelativistic first-order perturbation theory and density matrix formalism, we first derive the excitation cross sections and alignment parameters describing the population of excited atoms. Further calculations performed for the $1s \rightarrow 2p$ transition in atomic hydrogen indicate that the TAM projection of the incident Bessel beam affects the alignment of excited atoms for sufficiently small targets of size less than 200 nm. Finally we demonstrate that this effect can be observed experimentally by measuring the linear polarization of the subsequent fluorescence.

4.1 Theory of excitation with Bessel beams

4.1.1 Transition amplitude for Bessel beams

Let us first consider the photoexcitation of a single hydrogen atom from an initial $|n_i l_i m_i\rangle$ to a final $|n_f l_f m_f\rangle$ bound state, which is described within the framework of the nonrelativistic perturbation theory by the following matrix element (Bransden and Joachain 2003)

$$M_{m_f m_i}^{\mathrm{tw}}(\boldsymbol{b}) = \int \psi_{n_f l_f m_f}^*(\boldsymbol{r})\, \boldsymbol{A}^{\mathrm{B}}(\boldsymbol{r}+\boldsymbol{b}) \cdot \hat{\boldsymbol{p}}\, \psi_{n_i l_i m_i}(\boldsymbol{r})\, d^3\boldsymbol{r}\,, \qquad (4.1)$$

where the impact parameter $\boldsymbol{b} = (b_x, b_y, 0)$ characterizes the position of a target atom with respect to the beam axis. The main difference between this matrix element and that from the previous chapter lies in the final bound state. In order to calculate the amplitude for the excitation of the atom by the radiation prepared in the pure Bessel state, we insert its vector potential (2.13) into Eq. (4.1) and find

$$M_{m_f m_i}^{\text{tw}}(\boldsymbol{b}) = -i \int \frac{d^2 \boldsymbol{k}_\perp}{(2\pi)^2} \, a_{\varkappa m_\gamma}(\boldsymbol{k}_\perp) e^{i\boldsymbol{k}_\perp \boldsymbol{b}} \int d^3 \boldsymbol{r} \, \psi_{n_f l_f m_f}^*(\boldsymbol{r}) e^{i\boldsymbol{k}\boldsymbol{r}} \, \boldsymbol{e}_{\boldsymbol{k}\lambda} \cdot \nabla \, \psi_{n_i l_i m_i}(\boldsymbol{r})$$

$$= \int a_{\varkappa m_\gamma}(\boldsymbol{k}_\perp) e^{i\boldsymbol{k}_\perp \boldsymbol{b}} \, M_{m_f m_i}^{\text{pl}}(\theta_k, \phi_k) \frac{d^2 \boldsymbol{k}_\perp}{(2\pi)^2} \,. \tag{4.2}$$

Here we introduced the matrix element

$$M_{m_f m_i}^{\text{pl}}(\theta_k, \phi_k) = -i \int \psi_{n_f l_f m_f}^*(\boldsymbol{r}) e^{i\boldsymbol{k}\boldsymbol{r}} \, \boldsymbol{e}_{\boldsymbol{k}\lambda} \cdot \nabla \, \psi_{n_i l_i m_i}(\boldsymbol{r}) \, d^3 \boldsymbol{r} \,, \tag{4.3}$$

describing the absorption of a circularly polarized plane-wave photon $\boldsymbol{e}_{\boldsymbol{k}\lambda} e^{i\boldsymbol{k}\boldsymbol{r}}$ whose wave vector points in the direction $\hat{\boldsymbol{k}} = \boldsymbol{k}/k = (\theta_k, \phi_k)$ not coinciding with the quantization z axis. To calculate the matrix element $M_{m_f m_i}^{\text{pl}}(\theta_k, \phi_k)$ for this general case, we express the initial- and final-state atomic wavefunctions, defined in the coordinate system $S(x, y, z)$, in terms of the functions from the system $S(\tilde{x}, \tilde{y}, \tilde{z})$ with the $\tilde{z}$ axis along the vector $\boldsymbol{k}$. Since the $S(\tilde{x}, \tilde{y}, \tilde{z})$ coordinate system is obtained from the $S(z, y, z)$ by a rotation through an angle θ_k around the y axis and an angle ϕ_k around the z axis, we have (Varshalovich *et al* 1988)

$$\psi_{nlm}(\boldsymbol{r}) = \sum_{\tilde{m}} D_{m\tilde{m}}^{l*}(\phi_k, \theta_k, 0) \psi_{nl\tilde{m}}(\tilde{\boldsymbol{r}}) \,, \tag{4.4}$$

where the Wigner D function can be written in terms of his small d function as

$$D_{m\tilde{m}}^l(\phi_k, \theta_k, 0) = e^{-im\phi_k} d_{m\tilde{m}}^l(\theta_k) \,. \tag{4.5}$$

If one inserts these expressions into Eq. (4.3), one can derive

$$M_{m_f m_i}^{\text{pl}}(\theta_k, \phi_k) = e^{-i(m_f - m_i)\phi_k} \sum_{\tilde{m}_f \tilde{m}_i} d_{m_f \tilde{m}_f}^{l_f}(\theta_k) \, d_{m_i \tilde{m}_i}^{l_i}(\theta_k) M_{\tilde{m}_f \tilde{m}_i}^{\text{pl}}(0, 0) \,, \tag{4.6}$$

where $\tilde{m}_i$ and $\tilde{m}_f$ are projections of the initial- and final-state angular momenta on the $\tilde{z}$ axis, and where the matrix element $M_{\tilde{m}_f \tilde{m}_i}^{\text{pl}}(0, 0)$ corresponds to the absorption of circularly polarized plane-wave photon of helicity λ incident along the $\tilde{z}$ axis. According to the well-known selection rules for incoming plane-wave radiation

(Bransden and Joachain 2003), the matrix element $M^{\text{pl}}_{\tilde{m}_f \tilde{m}_i}(0,0)$ does not vanish only if $\tilde{m}_f = \tilde{m}_i + \lambda$. For example, if the initial state is the s state, the summation in the matrix element (4.6) is restricted to $\tilde{m}_i = 0$ and $\tilde{m}_f = \lambda$.

By inserting the matrix element (4.6) into Eq. (4.2) and performing the integration over the transverse momentum $k_\perp$ as well as over the azimuthal angle ϕ_k with the help of Eq. (2.15), we finally obtain the transition amplitude for the excitation of a single atom by twisted Bessel light in the form

$$M^{\text{tw}}_{m_f m_i}(\boldsymbol{b}) = i^{m_i - m_f}\, e^{i(m_\gamma + m_i - m_f)\phi_b}\, \sqrt{\frac{\varkappa}{2\pi}}\, J_{m_\gamma + m_i - m_f}(\varkappa b)\, M^{\text{pl}}_{m_f m_i}(\theta_k, 0)\,. \quad (4.7)$$

This formula shows that the amplitude $M^{\text{tw}}_{m_f m_i}(\boldsymbol{b})$ for the twisted light can be expressed in terms of the matrix elements (4.6) for the absorption of plane-wave photons.

4.1.2 Density matrix for the mesoscopic target

Next, we shall analyze the excitation of the target consisting of hydrogen atoms by Bessel beams. We assume that the atoms are distributed independently and symmetrically with respect to the target center, while their spatial distribution inside the target is characterized by the function $f(\boldsymbol{b} - \boldsymbol{b}_t)$. Here the impact parameter $\boldsymbol{b}$ is again the distance from the beam axis to a single atom in the target, and the vector $\boldsymbol{b}_t$ denotes the distance from the beam axis to the target center. To discuss the excitation of the target atoms which are assumed to be unpolarized, we will use the density matrix theory (Balashov *et al* 2000, Blum 2012). The final-state density for a single atom can be expressed in terms of transition amplitudes (4.7) as

$$\langle n_f l_f m_f | \hat{\rho}^{\text{s}}_f | n_f l_f m_f' \rangle = \frac{1}{2l_i + 1} \sum_{m_i} M^{\text{tw}}_{m_f m_i}(\boldsymbol{b})\, M^{\text{tw}\,*}_{m_f' m_i}(\boldsymbol{b})\,. \quad (4.8)$$

For the atomic target with the spatial distribution $f(\boldsymbol{b} - \boldsymbol{b}_t)$, we also need to average the density matrix (4.8) over positions of atoms. In this case, the density matrix for

the atomic target excited by a Bessel beam is given by

$$\langle n_f l_f m_f | \hat{\rho}_f | n_f l_f m'_f \rangle = \int \langle n_f l_f m_f | \hat{\rho}_f^{\text{s}} | n_f l_f m'_f \rangle \, f(\boldsymbol{b} - \boldsymbol{b}_t) \, d^2 \boldsymbol{b}$$

$$= \frac{i^{m'_f - m_f}}{2l_i + 1} \frac{\varkappa}{2\pi} \sum_{m_i} M^{\text{pl}}_{m_f m_i}(\theta_k, 0) \, M^{\text{pl}*}_{m'_f m_i}(\theta_k, 0) \int e^{i(m'_f - m_f)\phi_b}$$

$$\times \ J_{m_\gamma + m_i - m_f}(\varkappa b) \, J_{m_\gamma + m_i - m'_f}(\varkappa b) \, f(\boldsymbol{b} - \boldsymbol{b}_t) \, d^2 \boldsymbol{b} \,, \tag{4.9}$$

where we have employed the transition amplitude (4.7). The atomic density of the target in the xy plane is assumed to follow the Gaussian distribution

$$f(\boldsymbol{b} - \boldsymbol{b}_t) = \frac{1}{2\pi w^2} \, e^{-\frac{(b_x - b_{tx})^2 + (b_y - b_{ty})^2}{2w^2}} \tag{4.10}$$

with the width of the target w. As was pointed out by Eschner (2003), the Gaussian distribution provides a good description of the density of ions in Paul-type traps. Here the quantization z axis is taken along the beam axis, while the x axis is directed from the beam axis to the target center [cf. Fig. 4.2], so that $b_{ty} = 0$. With this atomic density, the density matrix for such a mesoscopic target can be significantly simplified if we write the integral over the $\boldsymbol{b}$ in Eq. (4.9) as

$$\int e^{i(m'_f - m_f)\phi_b} J_{m_\gamma + m_i - m_f}(\varkappa b) \, J_{m_\gamma + m_i - m'_f}(\varkappa b) \, f(\boldsymbol{b} - \boldsymbol{b}_t) \, d^2 \boldsymbol{b}$$

$$= \int_0^\infty e^{-(b^2 + b_t^2)/(2w^2)} \, J_{m_\gamma + m_i - m_f}(\varkappa b) \, J_{m_\gamma + m_i - m'_f}(\varkappa b) \, \frac{b \, db}{w^2}$$

$$\times \int_0^{2\pi} e^{i(m'_f - m_f)\phi_b + \frac{b b_t}{w^2} \cos \phi_b} \, \frac{d\phi_b}{2\pi} \,. \tag{4.11}$$

If we apply the integral representation of the modified Bessel function of the first kind (Abramowitz and Stegun 1964)

$$I_n(x) = \int_0^{2\pi} e^{in\phi_b + x \cos \phi_b} \, \frac{d\phi_b}{2\pi} \,, \tag{4.12}$$

we are able to perform the integration over ϕ_b in Eq. (4.11), thus giving rise to the density matrix in the form

$$\langle n_f l_f m_f | \hat{\rho}_f | n_f l_f m'_f \rangle = \frac{i^{m'_f - m_f}}{2l_i + 1} \frac{\varkappa}{2\pi} \sum_{m_i} M^{\text{pl}}_{m_f m_i}(\theta_k, 0) \, M^{\text{pl}*}_{m'_f m_i}(\theta_k, 0)$$

$$\times \int_0^\infty e^{-(b^2 + b_t^2)/(2w^2)} \, J_{m_\gamma + m_i - m_f}(\varkappa b) \, J_{m_\gamma + m_i - m'_f}(\varkappa b) \, I_{m'_f - m_f}\left(\frac{b b_t}{w^2}\right) \frac{b \, db}{w^2} \,, \tag{4.13}$$
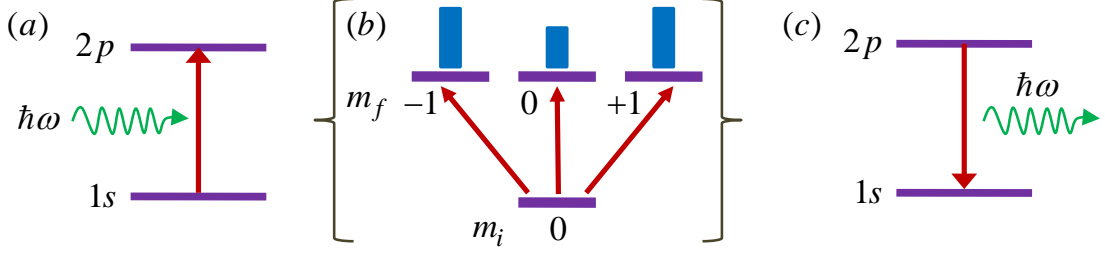
Figure 4.1: (a) Excitation of a $1s \to 2p$ transition in target hydrogen atoms with a twisted Bessel photon. (b) Magnetic sublevel population of the excited atomic $2p$ state described in the text by means of the alignment parameters. (c) Polarization of fluorescence signal due to spontaneous emission from the $2p$ level is determined by the alignment parameters of the hydrogen $2p$ level.

that will be used further on.

4.1.3 Photoexcitation cross sections

The density matrix for target atoms excited by twisted Bessel beams allows us to derive the properties of the excited atomic states. We start with the partial cross sections $\sigma_{m_f}^{\text{tw}}$ for the excitation $|n_i l_i\rangle + \gamma \to |n_i l_i m_f\rangle$ to a particular magnetic m_f state. If an incoming radiation is prepared in the Bessel state, the partial excitation cross section for the mesoscopic atomic target (4.10) is defined by

$$
\begin{aligned}
\sigma_{m_f}^{\text{tw}} &= \frac{2\pi}{j^{\text{tw}}} \frac{1}{2l_i + 1} \sum_{m_i} \int |M_{m_f m_i}^{\text{tw}}(\boldsymbol{b})|^2 \, f(\boldsymbol{b} - \boldsymbol{b}_t) \, d^2\boldsymbol{b} \; \delta(\omega + E_i - E_f) \\
&= \frac{2\pi}{j^{\text{tw}}} \langle n_f l_f m_f | \hat{\rho}_f | n_f l_f m_f \rangle \, \delta(\omega + E_i - E_f) \,,
\end{aligned} \tag{4.14}
$$

where the Dirac δ function ensures the energy conservation $\omega + E_i = E_f$ (Berestetskii *et al* 1982). We note that the partial cross sections $\sigma_{m_f}^{\text{tw}}$ are proportional to the diagonal elements of the density matrix (4.13) obtained above.

As can be seen from Eq. (4.14), we need to determine the flux j^{tw} of incident radiation for the calculation of these cross sections. For the Bessel beam of light, its flux through the surface of the mesoscopic target is defined by

$$
\begin{aligned}
j^{\text{tw}} &= \int S_z(r_\perp; m_\gamma = \lambda = 1) \, f(\boldsymbol{r}_\perp) \, d^2\boldsymbol{r}_\perp \\
&= \frac{\varkappa\omega}{4\pi^2\alpha} \left[I_0(w^2\varkappa^2) \cos^4(\theta_k/2) - I_2(w^2\varkappa^2) \sin^4(\theta_k/2) \right] e^{-w^2\varkappa^2} \,,
\end{aligned} \tag{4.15}
$$

where we have substituted $m_\gamma = \lambda = 1$ in the expression for longitudinal (z) component of the Poynting vector for Bessel beams (Matula *et al* 2013). If we use the formula $I_0(x) - I_2(x) = 2I_1(x)/x$ for the modified Bessel functions of the first kind (Abramowitz and Stegun 1964), we find that

$$j^{\mathrm{tw}} = \frac{\varkappa \omega}{4\pi^2 \alpha} \left\{ \frac{1 + \cos^2 \theta_k}{2w^2 \varkappa^2} I_1(w^2 \varkappa^2) + \frac{\cos \theta_k}{2} \left[I_0(w^2 \varkappa^2) + I_2(w^2 \varkappa^2) \right] \right\} e^{-w^2 \varkappa^2} .$$

(4.16)

One then sees that the flux j^{tw} is a positive function because $I_n(x) > 0$ when $x > 0$ and $n > -1$. In addition, this expression for the flux of a Bessel beam with zero opening angle θ_k gives us the correct limit of the plane-wave partial cross sections (Scholz-Marggraf *et al* 2014)

$$\sigma_{m_f}^{\mathrm{pl}} = \frac{2\pi}{j^{\mathrm{pl}}} \frac{1}{2l_i + 1} \sum_{m_i} |M_{m_f m_i}^{\mathrm{pl}}(0,0)|^2 \ \delta(\omega + E_i - E_f)$$

(4.17)

with the flux of the plane-wave radiation $j^{\mathrm{pl}} = \omega/(2\pi\alpha)$.

4.1.4 Alignment of excited atoms and polarization of fluorescence

Instead of the final-state density matrix derived before, it is often more convenient to describe the population of photoexcited atomic states with the help of the so-called statistical tensors $\rho_{k_f q_f}(n_f l_f)$ expressed in terms of the elements of the density matrix as

$$\rho_{k_f q_f}(n_f l_f) = \sum_{m_f m_f'} (-1)^{l_f - m_f'} \langle l_f m_f, l_f - m_f' | k_f q_f \rangle \langle n_f l_f m_f | \hat\rho_f | n_f l_f m_f' \rangle .$$

(4.18)

By using these statistical tensors $\rho_{k_f q_f}(n_f l_f)$, we can introduce the alignment parameters (or reduced statistical tensors) $\mathcal{A}_{k_f q_f}(n_f l_f)$ in the form

$$\mathcal{A}_{k_f q_f}(n_f l_f) = \frac{\rho_{k_f q_f}(n_f l_f)}{\rho_{00}(n_f l_f)} .$$

(4.19)

In fact, the alignment parameters with zero projection $q_f = 0$ are determined by the diagonal elements of the density matrix (4.13) and describe the relative population of atomic sublevels $|n_f l_f m_f\rangle$ [cf. Fig. 4.1], while the parameters $\mathcal{A}_{k_f q_f}(n_f l_f)$ with $q_f \neq 0$
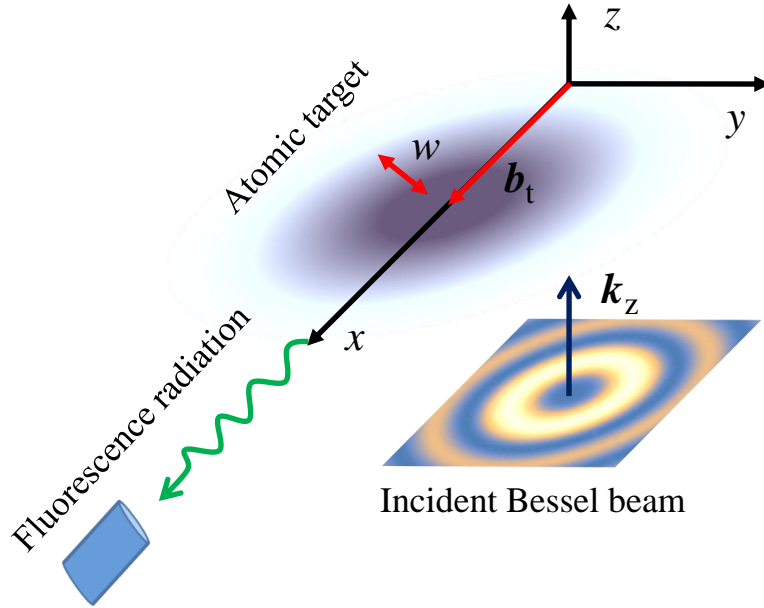
Figure 4.2: Geometry of the excitation of target atoms by Bessel beams and the subsequent fluorescence. The quantization z axis is chosen along the propagation direction of the incident beam, while the mesoscopic atomic target is located in the xy plane. The distance from the beam axis to the target center is described by b_t, and the x axis is taken along this direction. Moreover, the parameter w characterizes the size of target. The fluorescent light emitted by the subsequent radiative decay is detected along the x axis.

are determined by nondiagonal elements of the density matrix and characterize the coherence between sublevels with different m_f.

These alignment parameters of the excited state allow us to analyze the polarization of fluorescence light emitted in the subsequent radiative decay $|n_i l_i\rangle \to |n_0 l_0\rangle + \gamma$ to one of the lower-lying levels. As usual in atomic and optical physics, the polarization properties of photons are characterized by the Stokes parameters. In particular, we consider here the degree of linear polarization characterized by the Stokes parameter P_1. For the fluorescent photons detected along the x axis for the given geometry [cf. Fig. 4.2], the Stokes parameter P_1 within the leading electric dipole ($E1$) approximation reads as (Balashov $et\ al$ 2000)

$$P_1 = -\frac{\sqrt{\frac{3}{2}}\,\alpha_2^\gamma \sum_{q_f} \mathcal{A}_{2q_f}(n_f l_f)\left[d_{q_f 2}^2(\frac{\pi}{2}) + d_{q_f -2}^2(\frac{\pi}{2})\right]}{1 + \sqrt{\frac{4\pi}{5}}\,\alpha_2^\gamma \sum_{q_f}\mathcal{A}_{2q_f}(n_f l_f)\,Y_{2q_f}(\frac{\pi}{2},0)}\,,\tag{4.20}$$

where the parameter α_2^γ is given by

$$\alpha_2^\gamma = \sqrt{\frac{3}{2}} \sqrt{2l_f + 1} \, (-1)^{l_f + l_0 + 1} \begin{Bmatrix} l_f & l_f & 2 \\ 1 & 1 & l_0 \end{Bmatrix}, \qquad (4.21)$$

and where $Y_{2q_f}(\pi/2, 0)$ denotes the spherical harmonics. Here we assumed that the fine structure of the excited level remains unresolved. In experiment, this Stokes parameter is determined simply as $P_1 = (I_z - I_y)/(I_z + I_y)$, where the I_z and I_y are intensities of light linearly polarized along the z and y axes, respectively.

4.2 Numerical results for hydrogen atoms

4.2.1 Cross sections for $1s \to 2p$ excitation

Let us compare the partial cross sections (4.14) for the excitation of target hydrogenic atoms by twisted Bessel light with those for incident plane waves (4.17). To do so, we now introduce the relative total excitation cross section defined by

$$\frac{\sigma^{\mathrm{tw}}}{\sigma^{\mathrm{pl}}} = \frac{\sum_{m_f} \sigma_{m_f}^{\mathrm{tw}}}{\sum_{m_f} \sigma_{m_f}^{\mathrm{pl}}}. \qquad (4.22)$$

In order to illustrate the behaviour of these relative total cross sections, we consider the $1s \to 2p$ excitation of hydrogen atoms. In our calculations we assume that an incident twisted photon has the helicity $\lambda = +1$ and the opening angle $\theta_k = 20°$. Fig. 4.3 shows the relative total cross sections $\sigma^{(\mathrm{tw})}/\sigma^{(\mathrm{pl})}$ for different TAM projections $m_\gamma = 0$, $m_\gamma = 1$, and $m_\gamma = 5$ of the Bessel beam. Its top panel illustrates these cross sections as a function of the width w of the target located at distances $b_t = 20$ nm and $b_t = 100$ nm from the beam center. As seen from this figure, the cross sections depend strongly on the TAM projection m_γ of the beam if the target is rather small. When the atomic target becomes larger $w > 400$ nm, the excitation cross sections increase and eventually reach the limit $\sigma^{(\mathrm{tw})}/\sigma^{(\mathrm{pl})} = 1/\cos\theta_k = 1.064$ obtained in Scholz-Marggraf *et al* (2014) for the macroscopic (infinitely large) target. The position of the target with respect to the beam axis also affects the probability of the excitation. In the bottom panel of Fig. 4.3, we display the b_t dependence of the cross section for two different targets of size $w = 20$ nm and $w = 100$ nm. For the target located near the beam axis with $b_t < 50$ nm, the excitation cross section for the TAM projection $m_\gamma = 1$ is larger than those for $m_\gamma = 0$ and $m_\gamma = 5$,
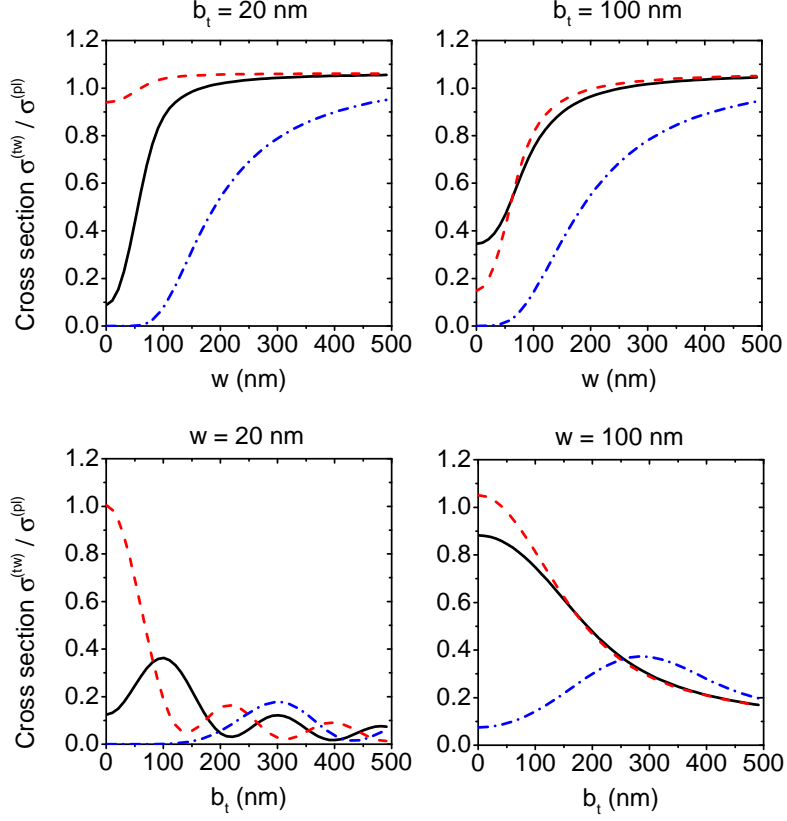
Figure 4.3: Relative total cross sections $\sigma^{(\mathrm{tw})}/\sigma^{(\mathrm{pl})}$ for the $1s \rightarrow 2p$ excitation of hydrogen atoms by a Bessel beam with the helicity $\lambda = +1$ and opening angle $\theta_k = 20°$. Top: Cross sections are presented as a function of the size w of atomic targets located at distances $b_t = 20$ nm (left) and $b_t = 100$ nm (right) from the beam center. Bottom: Relative total cross sections as a function of the position b_t of targets with width $w = 20$ nm (left) and $w = 100$ nm (right). Calculations are performed for three TAM projections of Bessel beams: $m_\gamma = 0$ (blacks solid lines), $m_\gamma = 1$ (red dashed lines), and $m_\gamma = 5$ (blue dash-dotted lines).

since the Bessel beam with TAM $m_\gamma = 1$ has a higher intensity near the beam axis, leading to a higher probability of the excitation. Moreover, when the target center is displaced further from the beam axis, the cross section $\sigma^{(\mathrm{tw})}/\sigma^{(\mathrm{pl})}$ decreases and reveals the oscillatory b_t behaviour. This is due to the fact that the intensity of Bessel beams in general also decreases and oscillates with increasing the distance from the beam center.
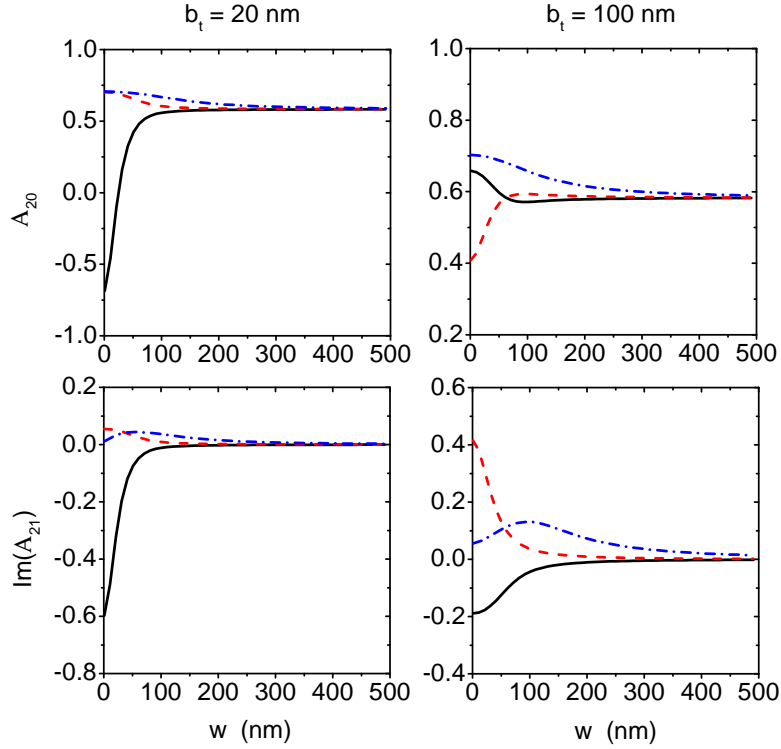
Figure 4.4: Alignment parameters $\mathcal{A}_{20}$ (top) and $\text{Im}(\mathcal{A}_{21})$ (bottom) of the excited $2p$ atomic state as a function of the size w of mesoscopic atomic target. The case of $1s \rightarrow 2p$ excitation by a Bessel beam with the opening angle $\theta_k = 20°$ and helicity $\lambda = +1$ is considered. Results are presented for hydrogen target located at distances $b_t = 20$ nm (left) and $b_t = 100$ nm (right). Alignment parameters are compared for three different TAM of the incident beam: $m_\gamma = 0$ (blacks solid lines), $m_\gamma = 1$ (red dashed lines), and $m_\gamma = 5$ (blue dash-dotted lines).

4.2.2 Alignment of excited $2p$ state

Having discussed the excitation cross sections, we can analyze the magnetic sublevel population of the excited $2p$ state by means of the alignment parameters (4.19). We restrict our attention just to the alignment parameters $\mathcal{A}_{2q_f}$, because they are required for the calculation of the first Stokes parameter P_1 of the fluorescence radiation (4.20). If we take into account their general properties $\mathcal{A}_{2-q_f} = (-1)^{q_f} \mathcal{A}_{2q_f}^*$ and $q_f = -2, ..., 2$ from Balashov *et al* (2000), we will see that there are only three independent alignment parameters, namely $\mathcal{A}_{20}$, $\mathcal{A}_{21}$, and $\mathcal{A}_{22}$. Moreover, our calculations also indicate that the parameter $\mathcal{A}_{22}$ is small compared with other two parameters, while the real part of $\mathcal{A}_{21}$ is always zero. The only two parameters $\mathcal{A}_{20}$ and $\text{Im}(\mathcal{A}_{21})$ will be hereby discussed below.
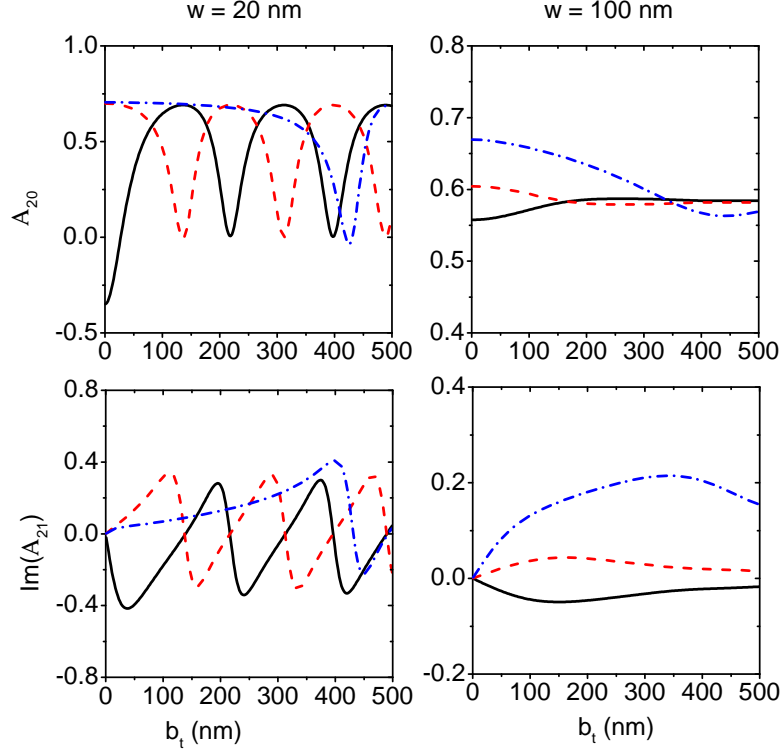
Figure 4.5: Same as Fig. 4.4, but for the alignment parameters $\mathcal{A}_{20}$ (top) and Im($\mathcal{A}_{21}$) (bottom) as a function of the distance b_t from the beam axis to the center of the target with size $w = 20$ nm (left) and $w = 100$ nm (right).

Fig. 4.4 displays the alignment parameters $\mathcal{A}_{20}$ (top) and Im($\mathcal{A}_{21}$) (bottom) as a function of the target size w. Results are shown for three TAM projections of the incident light and two target positions such as $b_t = 20$ nm (left) and $b_t = 100$ nm (right). The pronounced difference between alignment parameters with different m_γ and b_t is found for rather small hydrogen atomic target of $w < 200$ nm, as can be seen from Fig. 4.4. Nevertheless, the alignment parameter $\mathcal{A}_{20}$ for sufficiently large targets of size $w > 300$ nm is independent of the TAM m_γ and of the target position b_t, and it tends to the limit $\mathcal{A}_{20} = [1 + 3\cos(2\theta_k)]/(4\sqrt{2}) = 0.58$ obtained for the infinitely extended target (Scholz-Marggraf *et al* 2014). In addition, our computations indicate that the alignment parameter $\mathcal{A}_{21}$ vanishes for such large targets [cf. the bottom panel of Fig. 4.4]. This can be predicted by the symmetry arguments, according to which the system "atoms-beam" with the axial symmetry provides the only nonzero $\mathcal{A}_{k_f 0}$ alignment parameters (Balashov *et al* 2000). Since the spatial distribution of atoms in rather extended target has axial symmetry with
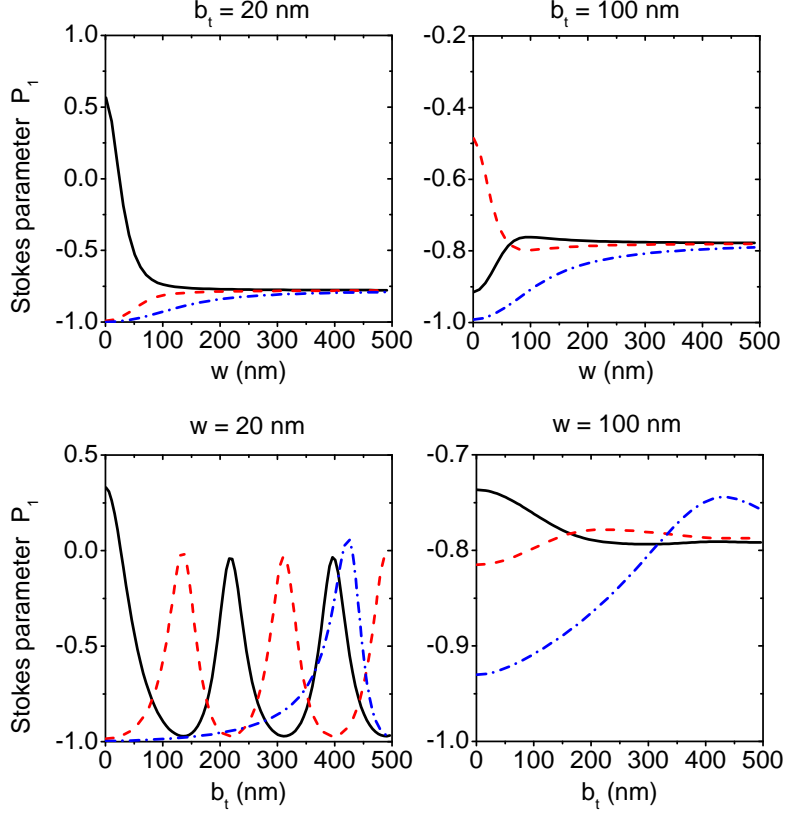
Figure 4.6: Stokes parameters P_1 of the $2p \rightarrow 1s$ fluorescence radiation propagating along the x axis and following the photoexcitation of hydrogen atoms by the Bessel beam with helicity $\lambda = +1$ and opening angle $\theta_k = 20°$. Top: P_1 as a function of the size w of atomic target located at distances $b_t = 20$ nm (left) and $b_t = 100$ nm (right). Bottom: P_1 as a function of the position b_t of the target with size $w = 20$ nm (left) and $w = 100$ nm (right). Stokes parameters are compared for the following TAM projections of twisted Bessel beams: $m_\gamma = 0$ (blacks solid lines), $m_\gamma = 1$ (red dashed lines), and $m_\gamma = 5$ (blue dash-dotted lines).

regard to the beam axis, the parameter $\mathcal{A}_{21}$ therefore becomes zero.

Let us now examine the behaviour of the alignment parameters $\mathcal{A}_{20}$ and $\text{Im}(\mathcal{A}_{21})$ when the target position b_t varies. As seen from Fig. 4.5, if the center of atomic target is placed right on the beam axis ($b_t = 0$), the alignment parameter $\mathcal{A}_{21}$ is always zero, in contrast to nonzero $\mathcal{A}_{20}$, because the target has axial symmetry with respect to the beam axis in this case. For the atomic targets displaced from the beam center ($b_t \neq 0$), the alignment parameters $\mathcal{A}_{20}$ and $\mathcal{A}_{21}$ are both nonzero and oscillate as functions of the distance b_t, as seen from the left column of Fig. 4.5. Again, these oscillations of the alignment parameters are revealed because of the

oscillatory structure of the intensity profile for Bessel beams.

4.2.3 Polarization of $2p \rightarrow 1s$ fluorescent light

Until now we have discussed the alignment parameters of the excited $2p$ state of hydrogen target atoms. Let us consider the polarization of the subsequent radiative decay $2p \rightarrow 1s$. In Fig. 4.6, for example, we display the Stokes parameter P_1 characterizing the degree of linear polarization along the z axis of the fluorescence emitted in the x direction. Both the target position b_t and the TAM projection m_γ of an incident Bessel beam affect the Stokes parameter P_1 for sufficiently small targets with $w < 200$ nm. However, similar to the alignment parameters, P_1 is independent of m_γ and b_t if the target becomes larger. Moreover, we note that the Stokes parameter oscillates as a function of the target position b_t, while the TAM projection m_γ of the Bessel beam affects the positions of its maxima. For instance, the first maximum of the Stokes parameter P_1 for $m_\gamma = 5$ (blue dash-dotted line) is located at $b_t = 420$ nm, in contrast to $b_t = 130$ nm for $m_\gamma = 1$ (red dashed line). This difference in maxima arise from the intensity profile of Bessel beams, since the first intensity maximum for the TAM $m_\gamma = 5$ lies further from the beam center than that for $m_\gamma = 1$.

5 Excitation of atoms by Laguerre-Gaussian beam

In a recent experiment, Schmiegelow *et al* (2016) investigated the magnetic sublevel population of Ca^+ ions in a Laguerre-Gaussian light beam if the target atoms were just centered along the beam axis. They demonstrated in this experiment that the sublevel population of excited atoms is uniquely defined by the projection of the orbital angular momentum of the incident twisted photon. However, little attention has been paid so far to the question of how the magnetic sublevels are populated when atoms are displaced from the beam axis by the impact parameter $\boldsymbol{b}$. In this chapter we shall study the sublevel population for twisted Laguerre-Gaussian beams and for different atomic impact parameters by making use of the density-matrix formalism. Detailed calculations are performed especially for the $4s\ ^2S_{1/2} \to 3d\ ^2D_{5/2}$ transition in Ca^+ ions. In so doing we will show that the magnetic sublevel population of the excited $^2D_{5/2}$ level varies significantly with the impact parameter and is sensitive to the polarization, the radial index, as well as the orbital angular momentum of the incident light beam.

5.1 Theory of excitation with Laguerre-Gaussian beams

5.1.1 Transition amplitude for Laguerre-Gaussian beams

We consider the excitation of a single atom from an initial state $|\alpha_i J_i M_i\rangle$ to a final state $|\alpha_f J_f M_f\rangle$, where J, M denote the total angular momentum and its projection upon the beam z axis. Here α refers to all additional quantum numbers. In relativistic first-order perturbation theory, the probability of this $|\alpha_i J_i M_i\rangle \to |\alpha_f J_f M_f\rangle$ transition is expressed in terms of the transition amplitude (Johnson 2007)

$$\mathcal{M}_{M_f M_i}(\boldsymbol{b}) = \langle \alpha_f J_f M_f | \sum_q \boldsymbol{\alpha}_q \cdot \boldsymbol{A}^{\mathrm{LG(C)}}(\boldsymbol{r}_q + \boldsymbol{b}) | \alpha_i J_i M_i \rangle \,, \tag{5.1}$$

where $\boldsymbol{A}^{\mathrm{LG(C)}}$ is the vector potential of the Laguerre-Gaussian beam in the Coulomb (C) gauge (2.37), the sum on q runs over all electrons in the atom, and $\boldsymbol{\alpha}_q$ denotes

the vector of Dirac matrices for the qth electron. While an free atom is typically not in a quantum state with well-defined projection M_i, such a polarized state can be prepared experimentally by optical pumping (Auzinsh *et al* 2010), for example. We used the impact parameter $\boldsymbol{b} \equiv b\boldsymbol{e}_x$ in order to designate the position of the atomic nucleus within the focus plane $z = 0$ of the beam [cf. Fig. 5.1]. In an experiment, such a displacement $\boldsymbol{b}$ of an atom can be controlled with few nanometers precision by using present-day Paul traps (Schmiegelow *et al* 2016). If we apply the decomposition of a Laguerre-Gaussian beam into plane waves (2.37), the transition amplitude then becomes

$$\mathcal{M}_{M_f M_i}(\boldsymbol{b}) = \int v_{pm}(k_\perp)\, e^{i(m+\lambda)\phi_k + i\boldsymbol{k}_\perp \boldsymbol{b}}$$
$$\times \langle \alpha_f J_f M_f | \sum_q \boldsymbol{\alpha}_q \cdot \boldsymbol{e}_{\boldsymbol{k}\lambda}\, e^{i\boldsymbol{k}\boldsymbol{r}_q} | \alpha_i J_i M_i \rangle\, d^2\boldsymbol{k}_\perp\,. \tag{5.2}$$

This expression readily shows that the amplitude $\mathcal{M}_{M_f M_i}$ for a Laguerre-Gaussian beam can simply be obtained from the matrix elements for circularly polarized plane waves $\boldsymbol{e}_{\boldsymbol{k}\lambda}\, e^{i\boldsymbol{k}\boldsymbol{r}}$ that propagate along the direction $\hat{\boldsymbol{k}} = (\theta_k, \phi_k)$, similar to Bessel beams. To evaluate these matrix elements, we expand the plane waves in terms of multipole fields

$$\boldsymbol{e}_{\boldsymbol{k}\lambda}\, e^{i\boldsymbol{k}\boldsymbol{r}} = \sqrt{2\pi} \sum_{L=1}^{\infty} \sum_{M=-L}^{L} \sum_{\mathfrak{p}=0,1} i^L\, \sqrt{2L+1}\, (i\lambda)^{\mathfrak{p}}\, D_{M\lambda}^L(\phi_k, \theta_k, 0)\, \boldsymbol{a}_{LM}^{\mathfrak{p}}(\boldsymbol{r})\,, \tag{5.3}$$

where $D_{M\lambda}^L$ is the Wigner D function, and $\boldsymbol{a}_{LM}^{\mathfrak{p}}$ refers to magnetic ($\mathfrak{p} = 0$) and electric ($\mathfrak{p} = 1$) multipole potentials (Rose 1957). If we substitute this multipole expansion into the matrix element for plane waves, we obtain (Surzhykov *et al* 2015)

$$\langle \alpha_f J_f M_f | \sum_q \boldsymbol{\alpha}_q \cdot \boldsymbol{e}_{\boldsymbol{k}\lambda}\, e^{i\boldsymbol{k}\boldsymbol{r}_q} | \alpha_i J_i M_i \rangle = \sqrt{2\pi} \sum_{LM} \sum_{\mathfrak{p}=0,1} i^L\, \sqrt{\frac{2L+1}{2J_f+1}}\, (i\lambda)^{\mathfrak{p}}$$
$$\times D_{M\lambda}^L(\phi_k, \theta_k, 0)\langle J_i M_i, LM | J_f M_f \rangle \langle \alpha_f J_f \| \sum_q \boldsymbol{\alpha}_q \cdot \boldsymbol{a}_{L,q}^{\mathfrak{p}} \| \alpha_i J_i \rangle\,. \tag{5.4}$$

Here we have applied the Wigner-Eckart theorem (Varshalovich *et al* 1988) to the matrix element of each term of the multipole expansion (5.3), since $\boldsymbol{\alpha}_q \cdot \boldsymbol{a}_{LM}^{\mathfrak{p}}(\boldsymbol{r}_q)$ is an irreducible tensor of rank L with projection quantum number M. Although several multipole transitions are generally possible, we just restrict ourselves to the leading multipole transition of lowest rank L as allowed by the triangle relation
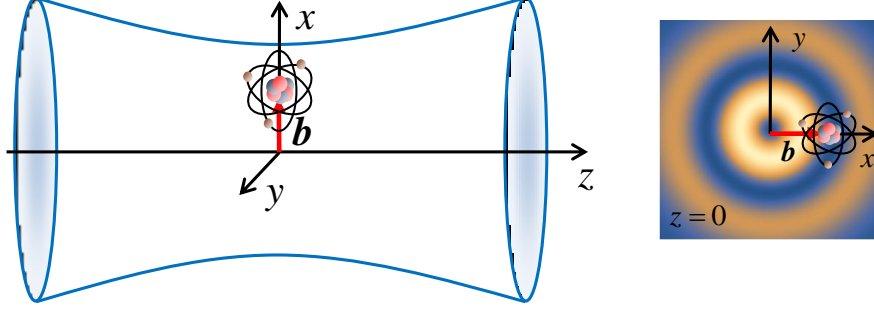
Figure 5.1: Geometry for the excitation of a single atom by Laguerre-Gaussian beam. The quantization z axis is chosen along the propagation direction of the incident beam, and the origin of the coordinate system lies on the beam axis. The atom is supposed to lie at the beam focus ($z = 0$), and its nucleus is shifted from the beam axis along the x axis by the impact parameter $\boldsymbol{b}$.

$|J_i - J_f| \leq L \leq J_i + J_f$ from the Clebsch-Gordan coefficients. This is a very good approximation for all low-energy transitions and light atoms. Another condition $M = M_f - M_i$ from the Clebsch-Gordan coefficients restricts the projection quantum number M, while the type of the multipole transition, magnetic ($\mathfrak{p} = 0$) or electric ($\mathfrak{p} = 1$), is determined by the parity selection rule $\pi_i \pi_f = (-1)^{L+\mathfrak{p}+1}$, and where π_i and π_f denote the parity of the initial and final atomic states, respectively.

If we substitute the matrix element of just the leading multipole from Eq. (5.4) into (5.2), the transition amplitude for the photoexcitation of a single atom by a Laguerre-Gaussian beam becomes

$$
\begin{aligned}
\mathcal{M}_{M_f M_i}(\boldsymbol{b}) =& \sqrt{2\pi} i^L (i\lambda)^{\mathfrak{p}} \sqrt{\frac{2L+1}{2J_f+1}} \langle J_i M_i, L\, M_f - M_i | J_f M_f \rangle \\
& \times \langle \alpha_f J_f \| \sum_q \boldsymbol{\alpha}_q \cdot \boldsymbol{a}^{\mathfrak{p}}_{L,q} \| \alpha_i J_i \rangle \int v_{pm}(k_\perp) \\
& \times e^{i(M_i + m + \lambda - M_f)\phi_k + i\boldsymbol{k}_\perp \boldsymbol{b}}\, d^L_{M_f - M_i\, \lambda}(\theta_k)\, d^2 \boldsymbol{k}_\perp \,,
\end{aligned}
\tag{5.5}
$$

and where we replaced the Wigner D function by the small d function (4.5) with $\theta_k = \arctan(k_\perp/k_z)$. The integral over the angle ϕ_k in the transition amplitude (5.5) can be evaluated analytically by using Eq. (2.15) together with $\boldsymbol{k}_\perp \boldsymbol{b} = k_\perp b \cos \phi_k$,

so that we finally obtain

$$
\begin{aligned}
\mathcal{M}_{M_f M_i}(\boldsymbol{b}) =& (2\pi)^{3/2}\, i^{L+M_i+m+\lambda-M_f}(i\lambda)^{\mathfrak{p}}\sqrt{\frac{2L+1}{2J_f+1}} \\
&\times \langle J_i M_i, L\, M_f - M_i | J_f M_f \rangle\, \langle \alpha_f J_f \| \sum_q \boldsymbol{\alpha}_q \cdot \boldsymbol{a}^{\mathfrak{p}}_{L,q} \| \alpha_i J_i \rangle \\
&\times \int_0^\infty v_{pm}(k_\perp)\, J_{M_i+m+\lambda-M_f}(k_\perp b)\, d^L_{M_f - M_i\, \lambda}(\theta_k)\, k_\perp\, dk_\perp\,.
\end{aligned} \tag{5.6}
$$

Here the magnetic quantum number M_f of a final atomic state is included not only in the Clebsch-Gordan coefficient, but also in the integral over the transverse momentum $k_\perp$, which is related to the structure of the beam. In this integral the Bessel function $J_{M_i+m+\lambda-M_f}(k_\perp b)$ expresses the dependence of the transition amplitude on the atomic impact parameter $\boldsymbol{b}$.

5.1.2 Density matrix of excited atoms

The photoexcited state of atoms can be efficiently described by means of the density-matrix. If we apply this formalism to the $|\alpha_i J_i M_i\rangle \to |\alpha_f J_f\rangle$ photoexcitation by a Laguerre-Gaussian beam from the state with well-defined projection M_i and make use of the transition amplitude (5.6), the density matrix of the excited $|\alpha_f J_f\rangle$ state reads (Balashov $et\ al$ 2000)

$$
\langle \alpha_f J_f M_f | \hat{\rho}_f | \alpha_f J_f M_f' \rangle = \mathcal{M}_{M_f M_i}(\boldsymbol{b})\, \mathcal{M}^*_{M_f' M_i}(\boldsymbol{b})\,. \tag{5.7}
$$

While the non-diagonal elements of the density matrix (5.7) characterize the coherence between sublevels with different M_f, its diagonal elements determine the relative partial cross sections for the excitation of the atom into a particular magnetic M_f sublevel

$$
\langle \alpha_f J_f M_f | \hat{\rho}_f | \alpha_f J_f M_f \rangle = \frac{\sigma_{M_f}(\boldsymbol{b})}{\sum_{M_f} \sigma_{M_f}(\boldsymbol{b})} = \frac{\sigma_{M_f}(\boldsymbol{b})}{\sigma_{\text{tot}}(\boldsymbol{b})}\,. \tag{5.8}
$$

As seen from Eq. (5.6), the relative partial cross sections (5.8) and, hence, also the population of the sublevels M_f depend not only on the impact parameter $\boldsymbol{b}$ of the atom, but also on the helicity λ, radial index p, and OAM m of the incident Laguerre-Gaussian beam. Below we will analyze these dependencies in more detail. The density matrix of the excited atoms (5.7) is experimentally accessible with present day techniques. In Schmiegelow $et\ al$ (2016), for instance, the density ma-
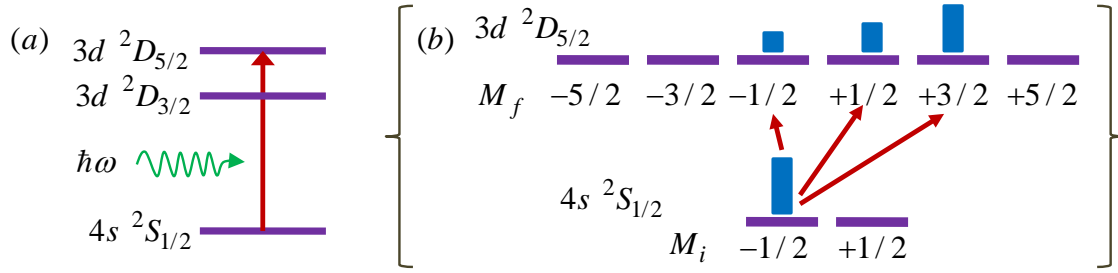
Figure 5.2: (a) Excitation of a $4s\ ^2S_{1/2}\ M_i = -1/2 \rightarrow 3d\ ^2D_{5/2}$ transition in Ca$^+$ ions with a Laguerre-Gaussian photon. (b) Magnetic sublevel population of the excited $3d\ ^2D_{5/2}$ state described in the text by means of the relative partial cross sections.

trix was obtained by measuring the Rabi frequency of the oscillations between the ground and excited atomic states, when the atoms were exposed to a Laguerre-Gaussian light beam. In this experiment each of the M_f magnetic sublevels was spectroscopically resolved due to an external magnetic field that was aligned along the beam propagation (z) direction.

5.2 Numerical results for Ca$^+$ ions

In the previous section, we just considered the excitation $|\alpha_i J_i M_i\rangle \rightarrow |\alpha_f J_f\rangle$ of a single atom by a Laguerre-Gaussian light beam. From the transition amplitude (5.6), we found the relative partial cross section (5.8) for populating sublevels $|\alpha_f J_f M_f\rangle$ of the excited atoms as a function of the atomic impact parameter b. We analyze the b dependence of the partial cross sections $\sigma_{M_f}/\sigma_{\text{tot}}$ especially for the electric-quadrupole $4s\ ^2S_{1/2}\ M_i = -1/2 \rightarrow 3d\ ^2D_{5/2}$ transition in Ca$^+$ ions that was used also in Schmiegelow *et al* (2016), and for which we have $L = 2$, $J_i = 1/2$, and $J_f = 5/2$ [cf. Fig. 5.2]. The calculations of the relative cross sections $\sigma_{M_f}/\sigma_{\text{tot}}$ were performed for a Laguerre-Gaussian beam with the optically accessible photon energy $\hbar\omega = 1.699$ eV and a beam waist $w_0 = 2.7\,\mu$m. Based on these calculations, we shall investigate below how the OAM m, the helicity λ, and the radial index p of the beam affect the sublevel population of the excited $3d\ ^2D_{5/2}$ state for different impact parameters b.

5.2.1 Partial cross sections for $4s\ ^2S_{1/2} \rightarrow 3d\ ^2D_{5/2}$ excitation

We begin with atoms that are centered on the beam axis ($b = 0$). Since the Bessel function in Eq. (5.6) is $J_{M_i+m+\lambda-M_f}(0) = \delta_{M_i+m+\lambda-M_f,\,0}$ (Abramowitz and Stegun 1964), only the magnetic sublevel

$$M_f = M_i + \lambda + m \tag{5.9}$$

is populated for the atoms of $b = 0$. The selection rule (5.9) obviously differs from the known rule $M_f = M_i + \lambda$ for an incident plane-wave light. The "modified" rule (5.9) has a simple physical interpretation: For atoms on the beam axis, only the projection $m + \lambda$ of the total angular momentum (TAM) of Laguerre-Gaussian beam can be transferred to the atoms. The selection rule (5.9) has also been demonstrated in the experiment (Schmiegelow *et al* 2016) for the $4s\ ^2S_{1/2}\ M_i = -1/2 \rightarrow 3d\ ^2D_{5/2}$ transition in Ca$^+$ ion. From the properties of the Clebsch-Gordan coefficient in Eq. (5.6) and the selection rule (5.9), we also deduce that no atom can be excited on the beam axis if the TAM of a Laguerre-Gaussian beam has a projection $m + \lambda$ which is larger than the multipolarity L of the underlying atomic transition. If the impact parameter is $b = 0$ and the helicity is $\lambda = +1$, for example, the electric-quadrupole ($E2$) transition $^2S_{1/2} \rightarrow ^2D_{5/2}$ with $L = 2$ is allowed for OAM $m = 1$, but is forbidden for $m = 2$.

Next, let us examine the behaviour of the relative cross sections (5.8) at small impact parameters $kb \ll 1$, i.e. when the atoms are only slightly displaced from the beam axis. By using the asymptotic form of the Bessel function $J_{M_i+m+\lambda-M_f}(k_\perp b)$ in the transition amplitude (5.6), we can approximate the relative partial cross sections (5.8) by

$$\frac{\sigma_{M_f}}{\sigma_{\text{tot}}} \approx \begin{cases} 1 - c_f \cdot (kb)^2, & \text{if } M_f = M_i + m + \lambda, \\ \tilde{c}_f \cdot (kb)^{2|M_i+m+\lambda-M_f|}, & \text{if } M_f \neq M_i + m + \lambda, \end{cases} \tag{5.10}$$

where the coefficients c_f and $\tilde{c}_f$ are independent of b, but depend on the radial index p and on the OAM m. Moreover, this m dependence is more pronounced, and the coefficients c_f and $\tilde{c}_f$ are very small for $m = 0$. Equation (5.10) shows that the population of the $M_f = M_i + m + \lambda$ sublevel may decrease quickly as the impact parameter b increases, while the population of all other M_f sublevels increases.

In the bottom line of Fig. 5.3 we display the relative partial cross sections $\sigma_{M_f}/\sigma_{\text{tot}}$ as a function of the impact parameter b. The calculations were performed using
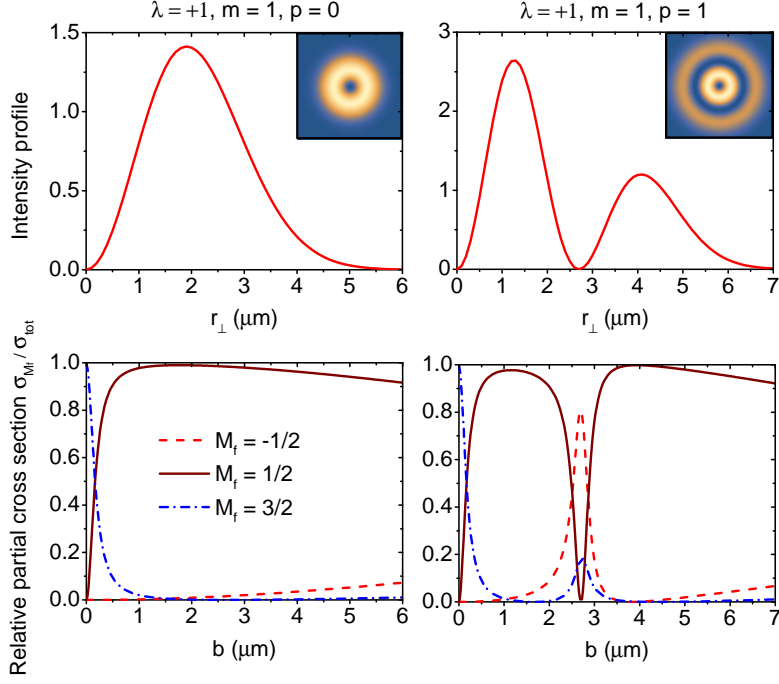
Figure 5.3: Top: Intensity profile $|u(r_\perp)|^2$ of a Laguerre-Gaussian beam for different radial indices $p = 0$ (left) and $p = 1$ (right), while the helicity $\lambda = +1$ and the OAM $m = 1$ are both kept constant. Results are shown in arbitrary units for the beam waist $w_0 = 2.7\,\mu\text{m}$ and the photon energy $\hbar\omega = 1.699$ eV at the beam focus ($z = 0$). Bottom: Relative partial cross sections for the $4s\ ^2S_{1/2}\ M_i = -1/2 \rightarrow 3d\ ^2D_{5/2}$ excitation of a Ca$^+$ ion by beams from above as a function of the atomic impact parameter b. The relative cross sections are compared for sublevels with $M_f = \pm 1/2, +3/2$, while those with $M_f = \pm 5/2, -3/2$ are very small and are not shown here.

the exact transition amplitudes (5.6) for two Laguerre-Gaussian beams of the same helicity $\lambda = +1$ and OAM $m = 1$, but with different radial indices $p = 0$ (left column) and $p = 1$ (right column). The intensity profiles of these beams exhibit a dark spot in the center surrounded by one concentric bright ring for $p = 0$ and by two bright rings for $p = 1$ [cf. the upper line of Fig. 5.3]. In accordance with the selection rule (5.9), only the magnetic sublevel $M_f = 3/2$ is excited when the atoms are placed in the center of the dark spot ($b = 0$). If the impact parameter b increases, the partial cross section for $M_f = 3/2$ decreases rapidly and the sublevel population approaches $M_f = 1/2$. In fact, the sublevel population varies near the beam axis in the same manner for both beams with radial indices $p = 0, 1$, and which can be understood from Eq. (5.10) at small b: while the relative population
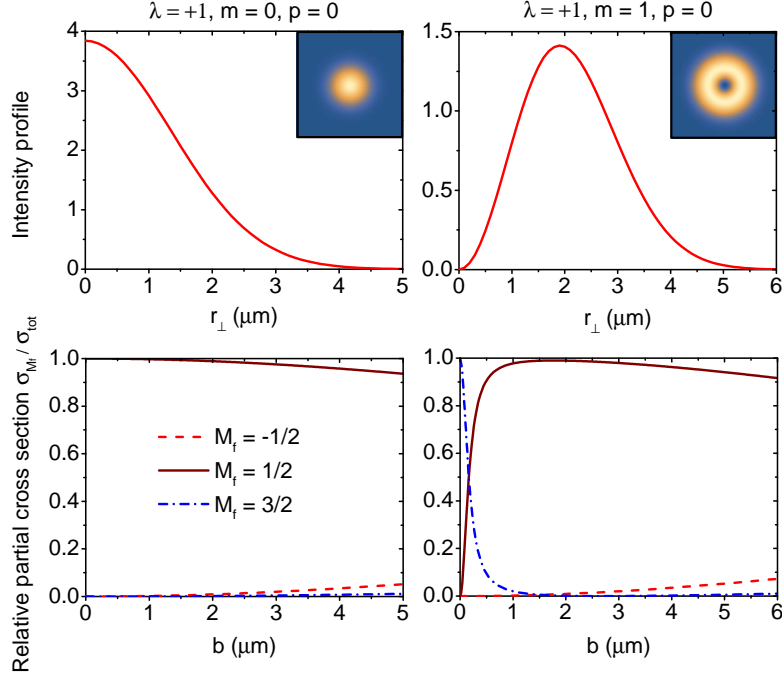
Figure 5.4: Same as Fig. 5.3, but for the Laguerre-Gaussian beams with different OAM $m = 0$ and $m = 1$, while the helicity $\lambda = +1$ and the radial index $p = 0$ are kept fixed.

of $M_f = 3/2$ decreases like $1 - c_f \cdot (kb)^2$ with increasing b, the population of the sublevel $M_f = 1/2$ increases like $\tilde{c}_f \cdot (kb)^2$. For a sufficiently large impact parameter $b = 2.7 \, \mu$m and for the radial index $p = 1$, however, the atoms are located in the dark ring of the beam and the sublevel population differs significantly from that for $p = 0$: the $M_f = -1/2$ and $M_f = 3/2$ magnetic sublevels are excited when $p = 1$, in contrast to the $M_f = 1/2$ when $p = 0$.

Let us further analyze how the partial cross sections $\sigma_{M_f}/\sigma_{\text{tot}}$ depend on the projection of the OAM m of the Laguerre-Gaussian beam. We consider two beams with different OAM $m = 0$ and $m = 1$, but with the same radial index $p = 0$ and helicity $\lambda = +1$. The intensity profile of the beam with quantum numbers $p = 0$ and $m = 0$ corresponds to a Gaussian beam and just comprises a central bright spot. In contrast, the intensity profile of the beam with $p = 0$ and $m = 1$ exhibits a central dark spot [cf. the upper line of Fig. 5.4]. The partial excitation cross sections for these two beams are shown in the lower line of Fig. 5.4. For the Gaussian beam ($p = 0$ and $m = 0$), only the $M_f = 1/2$ sublevel is populated when the atoms are located on the beam axis ($b = 0$). Moreover, this sublevel population remains almost unchanged if the impact parameter b increases. Note that such an excitation
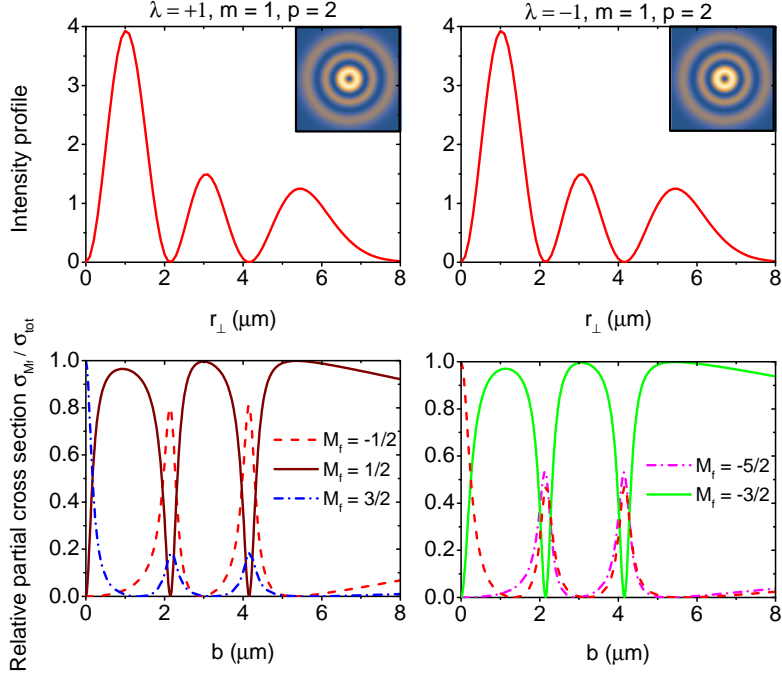
Figure 5.5: Same as Fig. 5.3, but for the Laguerre-Gaussian beams with different helicities $\lambda = \pm 1$, when the OAM $m = 1$ and the radial index $p = 2$ are kept constant. In the case of helicity $\lambda = +1$ ($\lambda = -1$), the relative cross sections are compared for sublevels with $M_f = \pm 1/2$, $+3/2$ ($M_f = -5/2, -3/2, -1/2$), while those with $M_f = \pm 5/2, -3/2$ ($M_f = +1/2, +3/2, +5/2$) are very small and are not shown here.

of only the $M_f = M_i + \lambda = 1/2$ sublevel is expected also if one assumes the absorption of plane-wave radiation that propagates with identical polarization along the z axis. Thus, the photoexcitation by a Gaussian beam is very similar to the photoexcitation by a plane wave. The pronounced difference from the plane-wave result $M_f = 1/2$ is found for OAM $m = 1$ in the dark spot ($b < 0.5\,\mu$m), where the $M_f = 3/2$ sublevel is mainly populated. If the impact parameter b increases, however, the sublevel population approaches the plane-wave limit $M_f = 1/2$. This indicates that the OAM m of the beam is much less transferred to atoms that are far from the beam axis, as has been noticed in the photoionization study (Wätzel and Berakdar 2016).

In order to further explore the influence of polarization on the excitation by a Laguerre-Gaussian beam, we consider two left-hand ($\lambda = -1$) and right-hand ($\lambda = +1$) circularly polarized beams with $p = 2$ and $m = 1$. Fig. 5.5 shows that although the intensity profiles of these two beams are identical, the population of excited
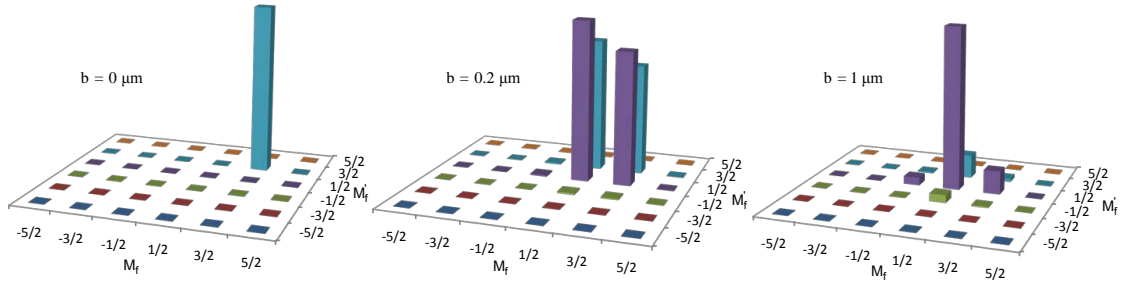
Figure 5.6: Density matrix $\langle \alpha_f J_f M_f | \hat{\rho}_f | \alpha_f J_f M'_f \rangle$ of the excited $3d$ $^2D_{5/2}$ state of a Ca$^+$ ion following the $4s$ $^2S_{1/2}$ $M_i = -1/2 \rightarrow 3d$ $^2D_{5/2}$ excitation by a Laguerre-Gaussian beam. Here, the absolute values of density matrix elements are displayed for three different impact parameters b. Calculations were performed for a beam with helicity $\lambda = +1$, radial index $p = 0$, OAM $m = 1$, beam waist $w_0 = 2.7 \,\mu$m, and photon energy $\hbar\omega = 1.699$ eV.

atomic states is significantly different in the case of different helicities. For the atoms near the beam axis, in particular, the $M_f = -1/2$ sublevel is mainly excited for the helicity $\lambda = -1$, while this applies to sublevel $M_f = 3/2$ if $\lambda = +1$. Again, this can be understood from the selection rule (5.9) for $b = 0$ and the formula (5.10) for small b.

5.2.2 Density matrix of excited $3d$ $^2D_{5/2}$ state

So far, we have considered the relative partial excitation cross sections (5.8) as obtained from the diagonal elements of the density matrix. In contrast, little was said about the non-diagonal matrix elements. Fig. 5.6 displays the absolute values of all elements $\langle \alpha_f J_f M_f | \hat{\rho}_f | \alpha_f J_f M'_f \rangle$ of the density matrix of the excited $3d$ $^2D_{5/2}$ state. Here, the density matrix (5.7) is shown for three different impact parameters $b = 0 \,\mu$m, $0.2 \,\mu$m, and $1 \,\mu$m and was calculated for a Laguerre-Gaussian beam with $\lambda = +1$, $p = 0$, and $m = 1$. As seen from Fig. 5.6, the atoms on the beam axis ($b = 0$) are found in an incoherent superposition of the magnetic M_f sublevels, since all non-diagonal elements of the density matrix are identically zero. On the other hand, there is coherence between the magnetic sublevels for those atoms that are displaced from the beam axis ($b = 0.2 \,\mu$m and $b = 1 \,\mu$m) because the non-diagonal elements of the density matrix do not vanish in this case.

6 Rayleigh scattering of Bessel beam by hydrogenlike ions

We have so far discussed primarily the resonant processes in which the frequency of the incident twisted photon is very close to the frequency of an atomic transition between two discrete states. However, not much is known about the nonresonant processes, for example, about the elastic scattering of twisted photons at the bound electrons of atoms or ions, commonly called as Rayleigh scattering, when the photon energy is not close to possible excitations of any intermediate states (Smend *et al* 1987). In this chapter we shall consider the behavior of the polarization of outgoing photons for the nonresonant Rayleigh scattering of a Bessel beam by hydrogenlike ions in their ground state, and especially by C^{5+} ions. We begin by deriving the polarization Stokes parameters of scattered photons within the framework of second-order perturbation theory and the density matrix approach. Then three different "experimental" scenarios are considered for the scattering at a single atom, a mesoscopic, or a macroscopic atomic target, and which are all assumed to be centered on the beam axis. Finally, results of our calculations for the Bessel beams with different polarizations, opening angles, and projections of the total angular momentum are compared with those for incident plane-wave radiation and demonstrate that the scattering of twisted light may lead to well detectable changes in the polarization of scattered photons.

6.1 Theory of Rayleigh scattering of Bessel beams

6.1.1 Evaluation of the transition amplitude

To discuss the Rayleigh scattering of twisted Bessel beams by hydrogenlike ions, we begin from the Furry picture of QED in which the electron-nucleus interaction is included into the unperturbed Hamiltonian, while the interaction with the radiation field is treated as a perturbation (Kane *et al* 1986). In this picture, the properties of the scattered photons can all be obtained from the second-order transition amplitude, based on Dirac's relativistic equation. In this framework, the amplitude is
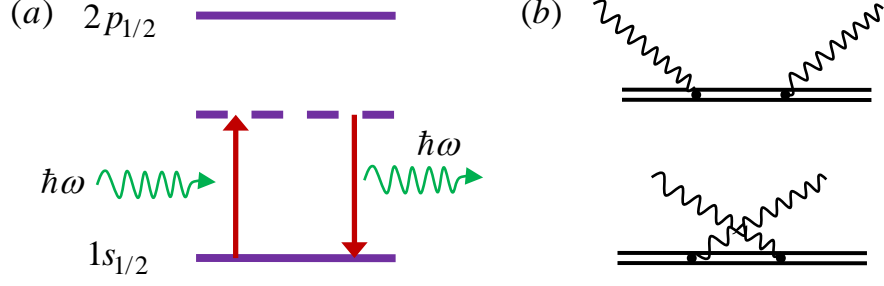
Figure 6.1: (a) Schemes of transitions in Rayleigh scattering of photons by C^{5+} ions. (b) Diagrams of lowest-order contributions to the Rayleigh scattering amplitude (6.1): the "absorption-first" contribution and the "emission-first" contribution.

given by (Surzhykov *et al* 2013, Akhiezer and Berestetskii 1965)

$$
\begin{aligned}
&\mathcal{M}^{\lambda_2 \lambda_1}_{m_f m_i}(\boldsymbol{b}) \\
&= \sum_{n_\nu j_\nu m_\nu} \frac{\langle n_f j_f m_f | \boldsymbol{\alpha} \cdot \boldsymbol{A}^{\mathrm{pl}*}(\boldsymbol{r}) | n_\nu j_\nu m_\nu \rangle \langle n_\nu j_\nu m_\nu | \boldsymbol{\alpha} \cdot \boldsymbol{A}^{\mathrm{B}}(\boldsymbol{r} + \boldsymbol{b}) | n_i j_i m_i \rangle}{E_i - E_\nu + \omega} \\
&+ \sum_{n_\nu j_\nu m_\nu} \frac{\langle n_f j_f m_f | \boldsymbol{\alpha} \cdot \boldsymbol{A}^{\mathrm{B}}(\boldsymbol{r} + \boldsymbol{b}) | n_\nu j_\nu m_\nu \rangle \langle n_\nu j_\nu m_\nu | \boldsymbol{\alpha} \cdot \boldsymbol{A}^{\mathrm{pl}*}(\boldsymbol{r}) | n_i j_i m_i \rangle}{E_i - E_\nu - \omega} \,, \quad (6.1)
\end{aligned}
$$

where $|n_i j_i m_i\rangle$ and $|n_f j_f m_f\rangle$ denote the states of the hydrogenlike ion before and after the scattering, and where $j_{i,f}$ and $m_{i,f}$ refer to the total angular momenta and their projections, and $n_{i,f}$ stand for principal quantum numbers. We here restrict ourselves to the elastic scattering of the photons with the energy ω on the ground state of atoms. This implies that the total energy of the bound electron for the initial and final states of the atom with $n_i = n_f$ and $j_i = j_f$ obeys the energy conservation law $E_i = E_f$, while the photon energy ω is not close to possible excitations of any intermediate states $|n_\nu j_\nu m_\nu\rangle$ over which the summation in the matrix element (6.1) is carried out, i.e., $\omega \neq E_\nu - E_i$ [cf. Fig. 6.1 (a)]. The two terms in Eq. (6.1) are represented diagrammatically in Fig. 6.1 (b), and $\boldsymbol{A}^{\mathrm{B}}$ is the vector potential of the Bessel beam given by Eq. (2.13) with the atomic impact parameter $\boldsymbol{b}$.

We assumed that the scattered photons are plane waves $\boldsymbol{A}^{\mathrm{pl}}(\boldsymbol{r}) = \boldsymbol{e}_{\boldsymbol{k}_2 \lambda_2} e^{i \boldsymbol{k}_2 \boldsymbol{r}}$ with $k_2 = k_1 = \omega/c$ measured by a plane-wave detector placed at asymptotic distance under the direction $\boldsymbol{k}_2$. To further analyze the transition amplitude (6.1), we can use the decomposition (5.3) of the plane-wave components of the incident and outgoing radiation in terms of the electric and magnetic multipole fields. If we substitute this

multipole expansion into Eq. (6.1) and make use of the vector potential (2.13) of Bessel beams, we can rewrite the transition amplitude as

$$\mathcal{M}_{m_f m_i}^{\lambda_2 \lambda_1}(\boldsymbol{b}) = \sum_{M_1} \int a_{\varkappa m_\gamma}(\boldsymbol{k}_{\perp_1}) \, e^{-iM_1 \phi_{k_1} + i\boldsymbol{k}_{\perp_1} \boldsymbol{b}} \, T_{m_f m_i}^{\lambda_2 \lambda_1}(M_1) \frac{d^2 \boldsymbol{k}_{\perp_1}}{(2\pi)^2} \qquad (6.2)$$

with the function $T_{m_f m_i}^{\lambda_2 \lambda_1}(M_1)$ of the form

$$T_{m_f m_i}^{\lambda_2 \lambda_1}(M_1) = \sum_{L_1 p_1} \sum_{L_2 M_2 p_2} 2\pi i^{L_1 - L_2} \sqrt{(2L_1 + 1)(2L_2 + 1)}$$

$$\times (i\lambda_1)^{p_1} (-i\lambda_2)^{p_2} \, e^{iM_2 \phi_{k_2}} \, d_{M_1 \lambda_1}^{L_1}(\theta_{k_1}) d_{M_2 \lambda_2}^{L_2}(\theta_{k_2})$$

$$\times \sum_{j_\nu} \left(\frac{\langle j_i m_i, L_1 M_1 | j_\nu m_\nu \rangle \langle j_\nu m_\nu, L_2 M_2 | j_f m_f \rangle}{\sqrt{(2j_\nu + 1)(2j_f + 1)}} \, S_{L_2 \mathfrak{p}_2, L_1 \mathfrak{p}_1}^{j_\nu}(\omega) \right.$$

$$\left. + \frac{\langle j_i m_i, L_2 M_2 | j_\nu m_\nu \rangle \langle j_\nu m_\nu, L_1 M_1 | j_f m_f \rangle}{\sqrt{(2j_\nu + 1)(2j_f + 1)}} \, S_{L_1 \mathfrak{p}_1, L_2 \mathfrak{p}_2}^{j_\nu}(-\omega) \right), \qquad (6.3)$$

where we have used the Wigner small d function and the Wigner-Eckart theorem (Varshalovich *et al* 1988). The reduced second-order matrix element is given by

$$S_{L_1 \mathfrak{p}_1, L_2 \mathfrak{p}_2}^{j_\nu}(\pm\omega) = \sum_{n_\nu} \frac{\langle n_f j_f \| \boldsymbol{\alpha} \cdot \boldsymbol{a}_{L_1}^{\mathfrak{p}_1} \| n_\nu j_\nu \rangle \langle n_\nu j_\nu \| \boldsymbol{\alpha} \cdot \boldsymbol{a}_{L_2}^{\mathfrak{p}_2} \| n_i j_i \rangle}{E_i - E_\nu \pm \omega} \,. \qquad (6.4)$$

Here the indices 1 and 2 refer to the incoming and outgoing photons, respectively. To further simplify the matrix element (6.2), we perform the integration over $k_{\perp_1}$ and ϕ_{k_1} with the help of Eq. (2.14) and by making use of the integral representation of the Bessel function (2.15). With this substitution, the transition amplitude for the scattering on a single hydrogenlike ion can be written as

$$\mathcal{M}_{m_f m_i}^{\lambda_2 \lambda_1}(\boldsymbol{b}) = \sqrt{\frac{\varkappa}{2\pi}} \sum_{M_1} (-i)^{M_1} \, e^{i(m_\gamma - M_1)\phi_b} \, J_{m_\gamma - M_1}(\varkappa b) \, T_{m_f m_i}^{\lambda_2 \lambda_1}(M_1) \,. \qquad (6.5)$$

As seen from this formula, the amplitude for the scattering of a Bessel beam depends not only on its helicity λ_1, the opening angle θ_{k_1} and the projection m_γ of the TAM, but also on the impact parameter $\boldsymbol{b}$ of the atom with respect to the beam axis. Below, we shall apply this transition amplitude to calculate the polarization of scattered light.

6.1.2 Scattering on a single atom

To characterize the polarization of scattered photons, we need to introduce the photon density matrix. For the scattering of twisted light on a single initially unpolarized atom with the impact parameter $\boldsymbol{b}$, the density matrix of scattered photons can be expressed in terms of the transition amplitudes as (Balashov *et al* 2000)

$$\langle \boldsymbol{k}_2 \lambda_2 | \hat{\rho}_{\gamma_2} | \boldsymbol{k}_2 \lambda_2' \rangle = \frac{1}{2j_i + 1} \sum_{\lambda_1 \lambda_1'} \sum_{m_i m_f} \mathcal{M}_{m_f m_i}^{\lambda_2 \lambda_1}(\boldsymbol{b}) \, \mathcal{M}_{m_f m_i}^{\lambda_2' \lambda_1' *}(\boldsymbol{b}) \, \langle \boldsymbol{k}_1 \lambda_1 | \hat{\rho}_{\gamma_1} | \boldsymbol{k}_1 \lambda_1' \rangle \,.$$

(6.6)

Here we assume that the magnetic sublevel population of the final state $|n_f j_f\rangle$ of the atom remains unobserved. The density matrix of an incident photon is $\langle \boldsymbol{k}_1 \lambda_1 | \hat{\rho}_{\gamma_1} | \boldsymbol{k}_1 \lambda_1' \rangle = \delta_{\lambda_1 \lambda_1'}$ for a completely polarized radiation with the helicity λ_1. In typical experiments, however, the incident light is often unpolarized, i.e. the beam consists out of a mixture of photons in states of opposite helicity $\lambda_1 = \pm 1$ with equal intensities whose density matrix is $\langle \boldsymbol{k}_1 \lambda_1 | \hat{\rho}_{\gamma_1} | \boldsymbol{k}_1 \lambda_1' \rangle = 1/2 \, \delta_{\lambda_1 \lambda_1'} \delta_{\lambda_1 + 1} + 1/2 \, \delta_{\lambda_1 \lambda_1'} \delta_{\lambda_1 - 1}$. Using the explicit expression of the amplitude (6.5), we can rewrite the density matrix of scattered photons in the form

$$\langle \boldsymbol{k}_2 \lambda_2 | \hat{\rho}_{\gamma_2} | \boldsymbol{k}_2 \lambda_2' \rangle = \frac{1}{2j_i + 1} \frac{\varkappa}{2\pi} \sum_{\lambda_1 \lambda_1'} \sum_{m_i m_f} \sum_{M_1 M_1'} i^{M_1' - M_1} \, e^{i(M_1' - M_1)\phi_b}$$
$$\times \, T_{m_f m_i}^{\lambda_2 \lambda_1}(M_1) \, T_{m_f m_i}^{\lambda_2' \lambda_1' *}(M_1') \, J_{m_\gamma - M_1}(\varkappa b) \, J_{m_\gamma - M_1'}(\varkappa b) \, \langle \boldsymbol{k}_1 \lambda_1 | \hat{\rho}_{\gamma_1} | \boldsymbol{k}_1 \lambda_1' \rangle \,. \quad (6.7)$$

Let us analyze the special case of atoms placed right on the beam axis $(b = 0)$. In this scenario, the Bessel function from Eq. (6.7) is just $J_{m_\gamma - M_1}(0) = \delta_{m_\gamma M_1}$, so that the photon density matrix reads

$$\langle \boldsymbol{k}_2 \lambda_2 | \hat{\rho}_{\gamma_2} | \boldsymbol{k}_2 \lambda_2' \rangle = \frac{1}{2j_i + 1} \frac{\varkappa}{2\pi} \sum_{\lambda_1 \lambda_1'} \sum_{m_i m_f} T_{m_f m_i}^{\lambda_2 \lambda_1}(M_1 = m)$$
$$\times \, T_{m_f m_i}^{\lambda_2' \lambda_1' *}(M_1' = m) \, \langle \boldsymbol{k}_1 \lambda_1 | \hat{\rho}_{\gamma_1} | \boldsymbol{k}_1 \lambda_1' \rangle \,. \quad (6.8)$$

This expression again indicates that the atom on the beam axis can just absorb a photon with the projection of the angular momentum m_γ. In practice, however, it is often difficult to position the atom just on the beam axis $(b = 0)$. Therefore, in the next section we will consider the scattering of twisted light by a mesoscopic atomic target in which atoms are localized with nanometer precision.
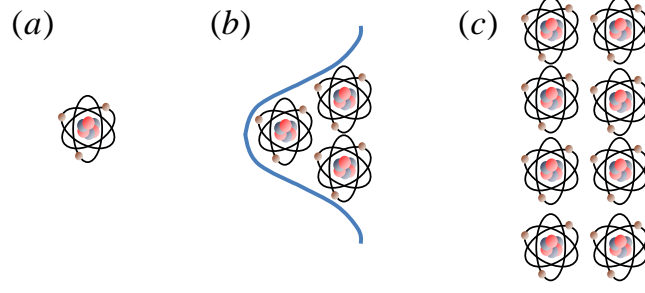
Figure 6.2: Different types of atomic targets: (a) a single atom, (b) mesoscopic target (atoms in a trap), (c) macroscopic target (foil).

6.1.3 Scattering on mesoscopic atomic target

The experiments on the interaction of twisted light beams with the atoms or ions, which are localized in a small volume of several tens of nanometers by means of a microstructured Paul trap, are feasible today (Schmiegelow *et al* 2016). For the Rayleigh scattering by such a mesoscopic atomic target centered on the beam axis, the density matrix of scattered photons is given by

$$\langle \boldsymbol{k}_2\lambda_2|\hat{\rho}_{\gamma_2}|\boldsymbol{k}_2\lambda_2'\rangle = \frac{1}{2j_i+1}\sum_{\lambda_1\lambda_1'}\sum_{m_im_f}\langle \boldsymbol{k}_1\lambda_1|\hat{\rho}_{\gamma_1}|\boldsymbol{k}_1\lambda_1'\rangle$$
$$\times \int f(\boldsymbol{b})\mathcal{M}_{m_fm_i}^{\lambda_2\lambda_1}(\boldsymbol{b})\,\mathcal{M}_{m_fm_i}^{\lambda_2'\lambda_1'\,*}(\boldsymbol{b})\,d^2\boldsymbol{b}\,, \tag{6.9}$$

where the atomic density of this target in the transverse plane [cf. Fig. 6.3] is assumed to follow the Gaussian distribution (4.10) with $b_t = 0$. After making use of the transition amplitude (6.5) and integrating over the azimuthal angle ϕ_b, the photon density matrix for the mesoscopic atomic target becomes

$$\langle \boldsymbol{k}_2\lambda_2|\hat{\rho}_{\gamma_2}|\boldsymbol{k}_2\lambda_2'\rangle = \frac{1}{2j_i+1}\frac{\varkappa}{2\pi w^2}\sum_{\lambda_1\lambda_1'}\sum_{m_im_fM_1}\langle \boldsymbol{k}_1\lambda_1|\hat{\rho}_{\gamma_1}|\boldsymbol{k}_1\lambda_1'\rangle\,T_{m_fm_i}^{\lambda_2\lambda_1}(M_1)$$
$$\times T_{m_fm_i}^{\lambda_2'\lambda_1'\,*}(M_1)\int_0^\infty J_{m_\gamma-M_1}^2(\varkappa b)\,e^{-\frac{b^2}{2w^2}}\,bdb\,. \tag{6.10}$$

Both the density matrices (6.8) and (6.10) show that the polarization of outgoing photons depends on the TAM projection m_γ of an incident Bessel beam in the elastic scattering by a single atom or by a mesoscopic atomic target. However, there is no m_γ dependence for a rather large macroscopic atomic target, as we shall see below.

6.1.4 Scattering on macroscopic atomic target

We next analyze the scattering of Bessel beam by a macroscopic (infinitely extended) target in which atoms are distributed uniformly over the entire plane normal to the beam propagation (z) direction. In the case of such a large target, the photon density matrix is defined by (Surzhykov *et al* 2015)

$$
\langle \boldsymbol{k}_2 \lambda_2 | \hat{\rho}_{\gamma_2} | \boldsymbol{k}_2 \lambda_2' \rangle
$$
$$
= \frac{1}{2j_i + 1} \sum_{\lambda_1 \lambda_1'} \sum_{m_i m_f} \langle \boldsymbol{k}_1 \lambda_1 | \hat{\rho}_{\gamma_1} | \boldsymbol{k}_1 \lambda_1' \rangle \int \mathcal{M}_{m_f m_i}^{\lambda_2 \lambda_1}(\boldsymbol{b}) \, \mathcal{M}_{m_f m_i}^{\lambda_2' \lambda_1' *}(\boldsymbol{b}) \, d^2 \boldsymbol{b}
$$
$$
= \frac{1}{2j_i + 1} \sum_{\lambda_1 \lambda_1'} \sum_{m_i m_f} \sum_{M_1 M_1'} \langle \boldsymbol{k}_1 \lambda_1 | \hat{\rho}_{\gamma_1} | \boldsymbol{k}_1 \lambda_1' \rangle \int a_{\varkappa m_\gamma}(\boldsymbol{k}_{\perp_1}) \, a_{\varkappa m_\gamma}^*(\boldsymbol{k}_{\perp_1}')
$$
$$
\times \, e^{-iM_1 \phi_{k_1} + iM_1' \phi_{k_1'} + i(\boldsymbol{k}_{\perp_1} - \boldsymbol{k}_{\perp_1}')\boldsymbol{b}} \, T_{m_f m_i}^{\lambda_2 \lambda_1}(M_1) \, T_{m_f m_i}^{\lambda_2' \lambda_1' *}(M_1') \frac{d^2 \boldsymbol{k}_{\perp_1} d^2 \boldsymbol{k}_{\perp_1}' d^2 \boldsymbol{b}}{(2\pi)^4} \,, \quad (6.11)
$$

where we have used the transition amplitude (6.2). Here the integration over the impact parameter $\boldsymbol{b}$ yields immediately the δ function $\delta(\boldsymbol{k}_{\perp_1} - \boldsymbol{k}_{\perp_1}')$. Moreover, if we perform the integration over the wave vector $\boldsymbol{k}_{\perp_1}'$ and over the azimuthal angle ϕ_{k_1}, we simply obtain $M_1 = M_1'$. We can further simplify the photon density matrix (6.11) by integrating over $k_{\perp_1}$, so that

$$
\langle \boldsymbol{k}_2 \lambda_2 | \hat{\rho}_{\gamma_2} | \boldsymbol{k}_2 \lambda_2' \rangle = \frac{1}{2j_i + 1} \sum_{\lambda_1 \lambda_1'} \sum_{m_i m_f M_1} T_{m_f m_i}^{\lambda_2 \lambda_1}(M_1) \, T_{m_f m_i}^{\lambda_2' \lambda_1' *}(M_1) \, \langle \boldsymbol{k}_1 \lambda_1 | \hat{\rho}_{\gamma_1} | \boldsymbol{k}_1 \lambda_1' \rangle \,.
$$
$$
(6.12)
$$

This formula shows that in the scattering on a macroscopic target the density matrix of outgoing photons and, hence, also their polarization are independent of the TAM projection m_γ of incoming twisted light, but still depend on its helicity λ_1 and opening angle θ_{k_1}.

6.1.5 Polarization parameters of the scattered photons

With the photon density matrices obtained above, we can now analyze the polarization of the Rayleigh scattered light. As before, the polarization properties of photons are characterized by the Stokes parameters. In particular, the parameter $P_1 = (I_{\chi=0°} - I_{\chi=90°})/(I_{\chi=0°} + I_{\chi=90°})$ characterizes the degree of linear polarization and is determined by the intensities I_χ of scattered light linearly polarized at an angle $\chi = 0°$ or $\chi = 90°$. Here the angle χ is defined with respect to the plane
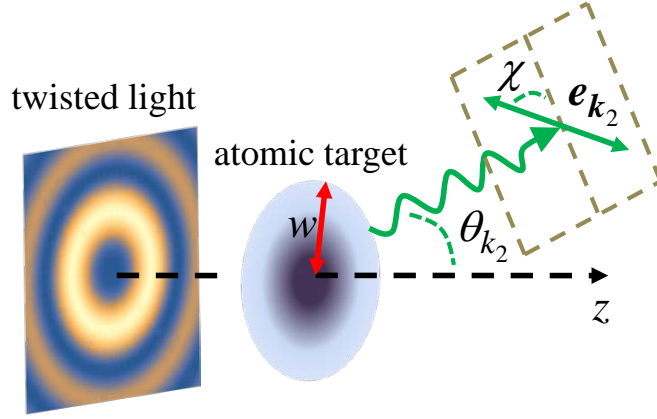
Figure 6.3: Geometry of the Rayleigh scattering of twisted light by a mesoscopic atomic target of size w. While the quantization (z) axis is taken along the propagation direction of the incident beam, the center of atomic target is placed on the beam axis. The emission direction of the outgoing photons is characterized by the angle θ_{k_2}, and their polarization vector $\boldsymbol{e}_{k_2}$ is described by the angle χ.

spanned by the directions of incident and outgoing photons [cf. Fig. 6.3]. Another parameter P_2, given by a similar ratio but for $\chi = 45°$ and $\chi = 135°$, is close to zero and therefore is not of interest. On the other hand, the nonzero parameter $P_3 = (I_{\lambda_2=+1} - I_{\lambda_2=-1})/(I_{\lambda_2=+1} + I_{\lambda_2=-1})$ characterizes the degree of circular polarization and is determined by the intensities I_{λ_2} of outgoing circularly polarized photons with the helicity $\lambda_2 = \pm 1$. Both these Stokes parameters can be expressed in terms of the density matrix of photons as (Balashov *et al* 2000)

$$P_1(\theta_{k_2}) = -\frac{\langle \boldsymbol{k}_2\lambda_2 = +1|\hat{\rho}_{\gamma_2}|\boldsymbol{k}_2\lambda_2' = -1\rangle + \langle \boldsymbol{k}_2\lambda_2 = -1|\hat{\rho}_{\gamma_2}|\boldsymbol{k}_2\lambda_2' = +1\rangle}{\langle \boldsymbol{k}_2\lambda_2 = +1|\hat{\rho}_{\gamma_2}|\boldsymbol{k}_2\lambda_2' = +1\rangle + \langle \boldsymbol{k}_2\lambda_2 = -1|\hat{\rho}_{\gamma_2}|\boldsymbol{k}_2\lambda_2' = -1\rangle},$$

$$P_3(\theta_{k_2}) = \frac{\langle \boldsymbol{k}_2\lambda_2 = +1|\hat{\rho}_{\gamma_2}|\boldsymbol{k}_2\lambda_2' = +1\rangle - \langle \boldsymbol{k}_2\lambda_2 = -1|\hat{\rho}_{\gamma_2}|\boldsymbol{k}_2\lambda_2' = -1\rangle}{\langle \boldsymbol{k}_2\lambda_2 = +1|\hat{\rho}_{\gamma_2}|\boldsymbol{k}_2\lambda_2' = +1\rangle + \langle \boldsymbol{k}_2\lambda_2 = -1|\hat{\rho}_{\gamma_2}|\boldsymbol{k}_2\lambda_2' = -1\rangle}. \quad (6.13)$$

As seen from these expressions, the Stokes parameters depend on the direction θ_{k_2} of scattered light. Therefore, in the next section we will use Eq. (6.13) to investigate the polarization of outgoing photons for different scattering angles θ_{k_2}.

6.1.6 Computations

Before we present our results for the Stokes parameters, let us briefly discuss some computational details. The evaluation of the polarization of scattered photons re-

quires the knowledge of the reduced second-order transition amplitude (6.4), which involves the summation over the complete basis of the intermediate states $|n_\nu j_\nu\rangle$. In order to perform this summation, we use two independent approaches: the finite basis-set method and the Dirac-Coulomb Green's function [see Volotka *et al* (2016) for further details]. These two numerical methods provide identical results, which demonstrates the high accuracy of our calculations.

6.2 Numerical results for C^{5+} ions

We found above the Stokes parameters P_1 and P_3 describing the polarization of scattered photons in the Rayleigh scattering of twisted Bessel beams by hydrogenlike ions. Such polarization parameters can be observed in present experiments (Blumenhagen *et al* 2016) and are expressed in terms of the photon density matrix, as seen from Eq. (6.13). We further analyze how these Stokes parameters of scattered photons depend on their emission angle θ_{k_2} for incident Bessel beams with different projections m_γ of the TAM, helicities λ_1, and opening angles θ_{k_1}. In addition, we compare these parameters P_1 and P_3 for twisted light with those obtained for a plane-wave radiation of the same helicity incident along the z axis. Calculations were performed for the photon energy $\hbar\omega = 100$ eV and for three different targets of C^{5+} ions: a single atom (6.8), a mesoscopic target (6.10), and a macroscopic target (6.12) which are centered on the beam axis.

6.2.1 Polarization for a single atom and mesoscopic target

We start with the first Stokes parameter P_1 that characterizes the degree of linear polarization of outgoing photons. Fig. 6.4 illustrates the parameter P_1 as a function of the emission angle θ_{k_2} for the Rayleigh scattering on a single atom (top row) as well as on the mesoscopic targets of size $w = 10$ nm (middle row) and $w = 20$ nm (bottom row). As seen from this figure, the outgoing photons are completely $P_1 = -1$ linearly polarized in the $\chi = 90°$ direction at the scattering angle $\theta_{k_2} = 90°$ for incoming plane waves (black solid lines). This is also true if a Bessel beam collides with a single atom that is located on the beam axis. However, the scattering of such a Bessel beam by mesoscopic target with width $w = 10$ nm, for example, leads to a significant decrease of the polarization at the angle $\theta_{k_2} = 90°$, namely $P_1 = -0.58$ when $m_\gamma = +1$ (red dashed line) or $P_1 = -0.47$ when $m_\gamma = -1$ (blue dash-dotted
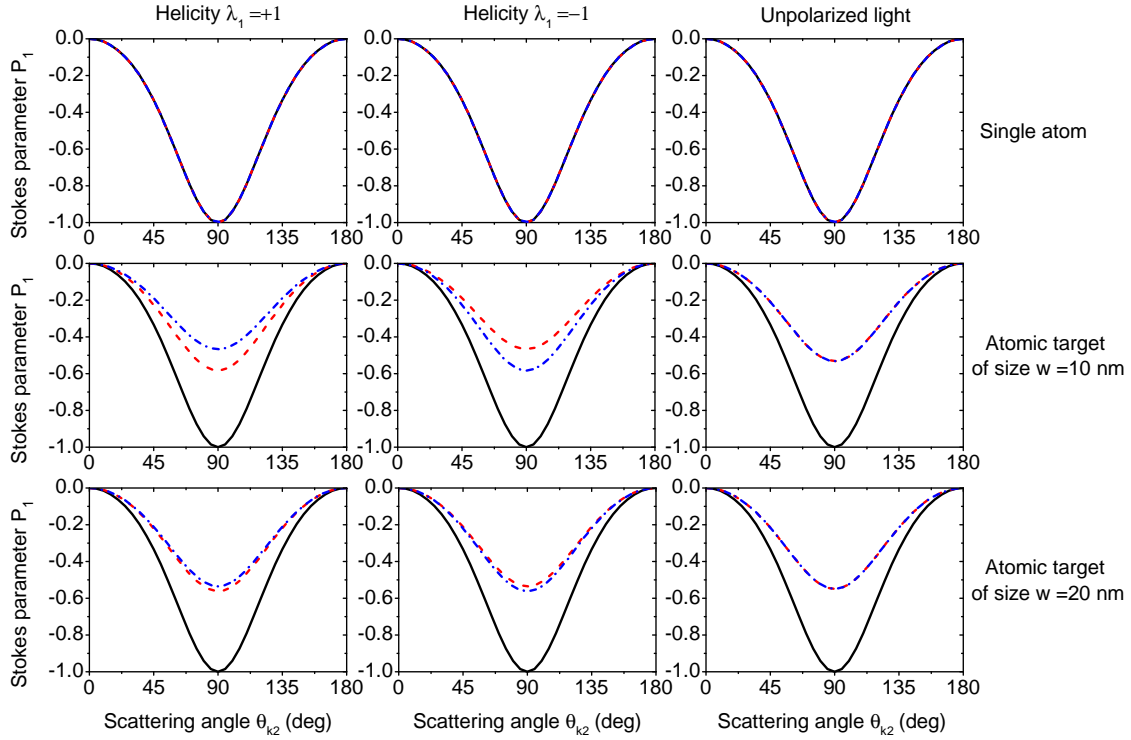
Figure 6.4: Stokes parameters P_1 of Rayleigh scattered light on hydrogenlike C^{5+} ions in their ground state as a function of the emission angle θ_{k_2}. Results for incident plane waves (black solid lines) are compared with those for Bessel beams with TAM $m_\gamma = +1$ (red dashed lines) and $m_\gamma = -1$ (blue dash-dotted lines), respectively. Relativistic calculations were performed for a single atom (top row) and for mesoscopic atomic targets of size $w = 10$ nm (middle row) and $w = 20$ nm (bottom row), which are centered on the beam axis. Results are shown for different helicities λ_1 of the incident light: $\lambda_1 = +1$ (left column), $\lambda_1 = -1$ (central column), and for the unpolarized light (right column). Both the opening angle $\theta_{k_1} = 30°$ of Bessel beams and the photon energy $\hbar\omega = 100$ eV are kept fixed.

line) for positive helicity $\lambda_1 = +1$, and vice versa for negative helicity $\lambda_1 = -1$. Thus the Stokes parameter P_1 of scattered photons depends on the TAM projection m_γ of twisted light of a well-defined helicity λ_1 in the scattering by a mesoscopic target. On the other hand, P_1 is independent of TAM m_γ if an incoming Bessel beam is unpolarized [cf. Fig. 6.4].

Apart from the linear polarization of elastically scattered light, we can analyze its degree of circular polarization. To do so, the third Stokes parameter P_3 as a function of the scattering angle θ_{k_2} is presented in Fig. 6.5. One sees that when the
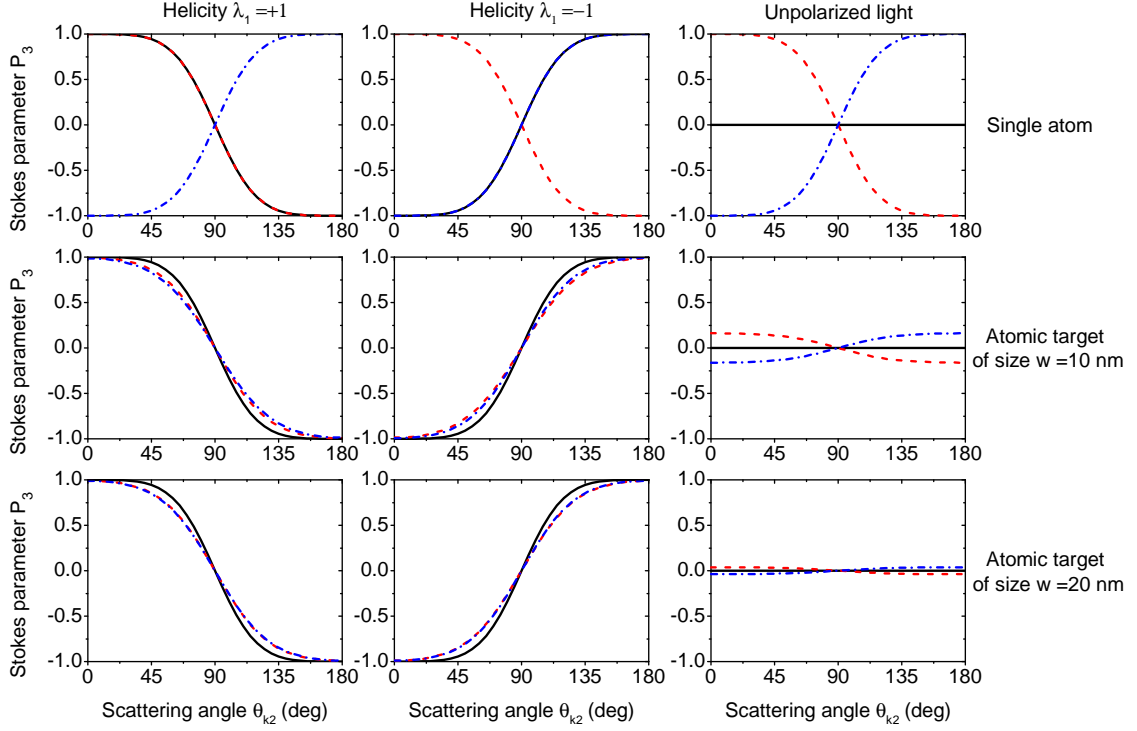
Figure 6.5: Same as Fig. 6.4, but for the Stokes parameters P_3 of elastically scattered photons.

incident radiation is a plane wave of helicity λ_1, the photons scattered in the forward $(\theta_{k_2} = 0°)$ direction are completely circularly polarized, namely $P_3 = +1$ if $\lambda_1 = +1$ or $P_3 = -1$ if $\lambda_1 = -1$. Moreover, the Stokes parameter P_3 of outgoing photons for the scattering of a twisted beam by a single atom on the beam axis coincides with the plane-wave results at all emission angles θ_{k_2} if the TAM projection of the beam is $m_\gamma = \lambda_1$, as shown in Fig. 6.5. However, P_3 corresponding to twisted light shows the opposite behaviour to P_3 for the plane waves if the TAM projection is $m_\gamma = -\lambda_1$. Such a difference in the polarization (or helicity) of outgoing photons is caused by the conservation of the angular momentum projection: the helicity λ_2 of a photon emitted in the forward $(\theta_{k_2} = 0°)$ direction should be equal to the projection M_1 of the angular momentum of a photon absorbed by the atom on the beam axis, which is $M_1 = m_\gamma$ for a Bessel beam (6.8), in contrast to $M_1 = \lambda_1$ for a plane wave.

Let us consider how the mesoscopic atomic target may affect the third Stokes parameter of scattered light. Eq. (6.10) implies that all possible projections M_1 of the angular momentum of incoming photons are able to contribute to the scattering of

twisted light by mesoscopic target, in contrast to $M_1 = m_\gamma$ for the scattering by a single atom. As a result, in the case of a mesoscopic target the parameter P_3 of outgoing photons for an incident Bessel beam is slightly different from that for a plane wave in the angular range $30° \lesssim \theta_{k_2} \lesssim 70°$ and $110° \lesssim \theta_{k_2} \lesssim 150°$, as can be seen from the middle and bottom rows of Fig. 6.5. In addition, the Stokes parameters P_1 and P_3 are quite different for the two TAM projections $m_\gamma = \pm 1$ of the beam when the mesoscopic target is rather small ($w = 10$ nm). However, Figs. 6.4 and 6.5 also show that this difference between the Stokes parameters for various TAM m_γ decreases with increasing size of the target ($w = 20$ nm).

Strong effects of "twistedness" in the polarization of scattered light can be observed also for an incoming unpolarized Bessel beam containing photons of both helicities $\lambda_1 = \pm 1$ but with a fixed TAM projection m_γ. In particular, Fig. 6.5 demonstrates that the Stokes parameter P_3 of outgoing photons is not always zero in the scattering of such a beam, in contrast to P_3 for incident unpolarized plane waves. For example, when the unpolarized twisted light with TAM projection $m_\gamma = +1$ collides with a single atom, the third Stokes parameter (red dashed line) behaves similarly to that obtained for the incident beam with a well-defined helicity $\lambda_1 = +1$. This is because in the scattering of twisted light by a single atom P_3 does not depend on the helicity λ_1, but is only sensitive to the TAM m_γ. With increasing target size w, however, the parameter P_3 for the case of unpolarized Bessel beam decreases and tends to zero as expected for incoming unpolarized plane waves [cf. Fig. 6.5].

6.2.2 Polarization for macroscopic target

Finally, we consider the scattering of twisted light by a macroscopic target as it occurs, for instance, for the scattering at a foil of neutral atoms or at a jet of ions (Blumenhagen *et al* 2016). For such an extended target, the polarization of outgoing photons is independent of the TAM projection m_γ of the twisted light, and as pointed out already in Sec. 6.1.4. In Fig. 6.6 we compare the two Stokes parameters P_1 and P_3 of the scattered light for different opening angles θ_{k_1} of Bessel beams with those for plane waves incident along the z axis. Similar as before, results were obtained as a function of the scattering angle θ_{k_2} for different helicities of the radiation. Here one can see that the parameters P_1 and P_3 for the scattering of a Bessel beam with a very small opening angle ($\theta_{k_1} = 1°$) are almost identical to those as obtained for incident plane waves. However, the Stokes parameter P_1 behaves very differently for large opening angles ($\theta_{k_1} = 60°$) and may become even positive at the emission angle
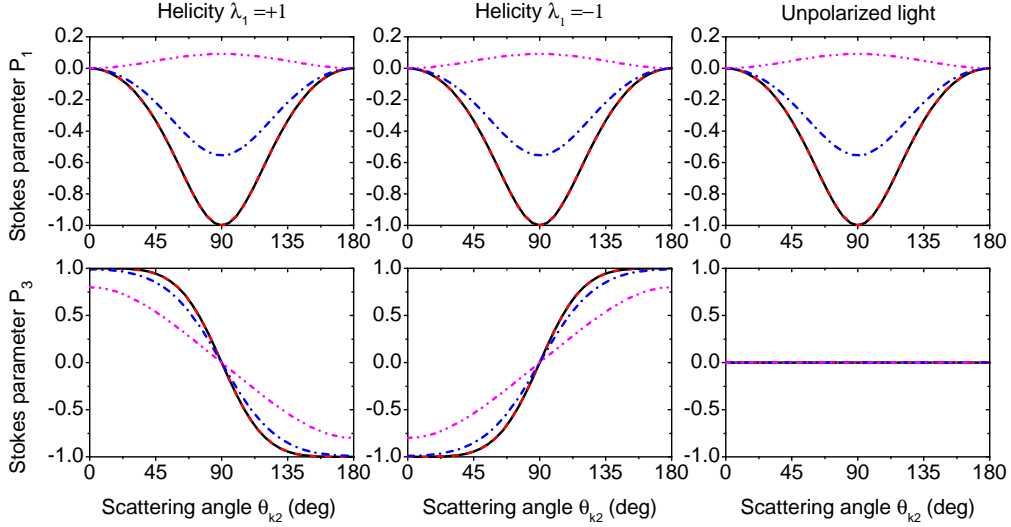
Figure 6.6: Stokes parameters P_1 (top row) and P_3 (bottom row) of elastically scattered photons on hydrogenlike C^{5+} ions in their ground state for a macroscopic target. Plane-wave results (black solid lines) are compared with those for Bessel beams with opening angles $\theta_{k_1} = 1°$ (red dashed lines), $\theta_{k_1} = 30°$ (blue dash-dotted lines), and $\theta_{k_1} = 60°$ (magenta dash-dot-dotted lines). Calculations were performed for different helicities λ_1 of the incident light: $\lambda_1 = +1$ (left column), $\lambda_1 = -1$ (central column), and for the unpolarized light (right column), when the photon energy $\hbar\omega = 100$ eV is fixed.

$\theta_{k_2} = 90°$. Moreover, for large angles θ_{k_1}, the circular polarization of the scattered photons is decreased in forward direction, for example $P_3 = \pm 0.8$ if the helicity of a Bessel beam is $\lambda_1 = \pm 1$. These modifications of the polarization of scattered light follow from Eq. (6.12) and imply that the scattering of a Bessel beam by macroscopic target can be considered as a scattering of plane waves propagating at the opening angle θ_{k_1} with respect to the quantization z axis.

7 Summary

In the present thesis, a number of processes involving the interaction of twisted photons with atomic systems have been investigated theoretically. We started in Chapter 2 with a brief review of the twisted beams of light. The vector potentials for Bessel and Laguerre-Gaussian beams have then been introduced. It was shown that both these twisted photon beams may have a well-defined projection of the OAM upon their propagation direction, leading to the helical wavefront and to transverse intensity profile with a ring-like pattern, in contrast to plane waves with a plane wavefront and homogeneous intensity profile. We have also derived the vector potentials for the Bessel and Laguerre-Gaussian beams in the form of a superposition of plane waves given in the Coulomb gauge, which is convenient when performing atomic calculations.

Chapter 3 deals with the the photoionization of H_2^+ molecular ions by twisted Bessel beam. The nonrelativistic theory along with first-order Born approximation were applied to derive and analyze the angle-differential photoionization cross sections. In this analysis, a macroscopic target of randomly distributed but aligned H_2^+ molecular ions was assumed throughout the derivations. For such a target, it was shown that the differential cross section is sensitive to the opening angle of the incident Bessel beam, while it remains independent of the TAM projection. Detailed calculations have been carried out for different alignment of the molecular ions and for different photon energies of the incident Bessel light to see how these properties affect the oscillations in the cross sections as known for incident plane-wave radiation. The main modifications in the angular distribution of the photoelectrons hereby arise due to the ringlike pattern of Bessel beams and their intensity variation relative to the size of the H_2^+ molecular ions. Hence, the photoionization of diatomic molecules by twisted radiation opens up different possibilities for the investigation of atomic double-slit phenomena. The use of twisted photons will allow one to perform a molecular analog of Young's experiment with two slits of unequal widths.

Then in Chapter 4 we performed an analysis of the excitation of the mesoscopic hydrogen-atom target (atoms in a trap) by Bessel beams within the framework of the density-matrix theory. Special attention was paid to the magnetic sublevel population of excited atomic states described by means of the alignment parameters. We found that these alignment parameters can be very sensitive not only with

regard to the opening angle of the Bessel beams, but also to their TAM projection for sufficiently small atomic targets. Our calculations performed for the $1s \rightarrow 2p$ transition in hydrogen indicate that the "twistedness" of incoming radiation can lead to a measurable change in the linear polarization of the subsequent fluorescence emission. Experimental observations of the fluorescence photons are well established today and can provide valuable information about the interaction of twisted light with atomic ensembles.

In Chapter 5 we looked at the excitation of atoms by a Laguerre-Gaussian light beam. A great deal of attention has been paid to the relative partial cross sections for the excitation to a particular magnetic sublevel, when the atoms are displaced from the beam axis by some impact parameter. The calculations were performed especially for the $4s\ ^2S_{1/2} \rightarrow 3d\ ^2D_{5/2}$ transition in Ca$^+$ ions. It was shown that the sublevel population of excited atoms is sensitive to the polarization of the incident twisted beam. Moreover, we find that the projection of the beam's OAM modifies the sublevel population if the atoms are located in the dark spot within the central region of the beam. In contrast, the radial index of the Laguerre-Gaussian beam affects the population of excited atomic states when the atoms are far from the beam axis and are placed in the dark ring of the beam. In addition, the atoms on the beam axis are found in an incoherent superposition of magnetic sublevels, while there is coherence between magnetic sublevels for the atoms moved from the beam's center. We emphasize that our theory confirms the results of the experiment by Schmiegelow *et al* (2016), which was performed with atoms on the beam axis, and predicts also the results of experiments with arbitrary atomic impact parameter.

Finally, in Chapter 6 we explored the Rayleigh scattering of twisted Bessel beam by hydrogenlike ions within the framework of Dirac's relativistic equation. In this analysis, we focused on the polarization of photons scattered by a single atom, by a mesoscopic target of trapped atoms, or by a macroscopic target like a foil or jet of atoms. The polarization Stokes parameters of outgoing photons were calculated especially for hydrogenlike carbon. We have shown that the linear and circular polarization of scattered light depends generally on the polarization and the opening angle of Bessel beams, leading to Stokes parameters that differ quite significantly from the scattering of incident plane-wave photons. Moreover, the polarization of the scattered photons is very sensitive to the TAM projection of twisted light for mesoscopic atomic targets of a few tens of nm in size, while it remains unaffected by the TAM in the case of a larger macroscopic target. Although our study was

restricted to the scattering by hydrogenlike ions in their ground $1s$ state, similar polarization properties can also be observed in the scattering of twisted light by electrons in other s shells. For example, we expect the same scattering polarization pattern for Ca^+ ions. Thus the Rayleigh scattering may serve as an accurate technique for measuring the properties of twisted beams in a wide range of photon energies, and in particular at rather high energies.

Bibliography

Abramowitz M and Stegun I A 1964 *Handbook of Mathematical Functions* (Washington, DC: National Bureau of Standards)

Afanasev A, Carlson C E and Mukherjee A 2013 *Phys. Rev.* A **88** 033841

Akhiezer A I and Berestetskii V B 1965 *Quantum Electrodynamics* (New York: Wiley)

Akoury D *et al* 2007 *Science* **318** 949

Akulshin A M, McLean R J, Mikhailov E E and Novikova I 2015 *Opt. Lett.* **40** 1109

Allen L, Beijersbergen M W, Spreeuw R J C and Woerdman J P 1992 *Phys. Rev.* A **45** 8185

Anderson M H, Ensher J R, Matthews M R, Wieman C E and Cornell E A 1995 *Science* **269** 198

Andrews D L and Babiker M (Eds.) 2013 *The Angular Momentum of Light* (Cambridge: Cambridge University Press)

Auzinsh M, Budker D and Rochester S M 2010 *Optically Polarized Atoms: Understanding Light-Atom Interactions* (Oxford: Oxford University Press)

Babiker M, Bennett C R, Andrews D L and Romero L C D 2002 *Phys. Rev. Lett.* **89** 143601

Bahrdt J, Holldack K, Kuske P, Müller R, Scheer M and Schmid P 2013 *Phys. Rev. Lett.* **111** 034801

Balashov V V, Grum-Grzhimailo A N and Kabachnik N M 2000 *Polarization and Correlation Phenomena in Atomic Collisions* (Berlin: Springer)

Baltenkov A S, Becker U, Manson S T and Msezane A Z 2012 *J. Phys.* B **45** 035202

Baranova N B and Zel'dovich B Ya 1981 *Zh. Eksp. Teor. Fiz.* **80** 1789

Berestetskii V B, Lifshitz E M and Pitaevskii L P 1982 *Quantum Electrodynamics* (Oxford: Pergamon)

Blaga C I, Catoire F, Colosimo P, Paulus G G, Muller H G, Agostini P and DiMauro L F 2009 *Nature Phys.* **5** 335

70

Bliokh K Y and Nori F 2015 *Phys. Rep.* **592** 1

Blum K 2012 *Density Matrix Theory and Applications* (Berlin: Springer)

Blumenhagen K-H, Fritzsche S, Gassner T, Gumberidze A, Märtin R, Schell N, Seipt D, Spillmann U, Surzhykov A, Trotsenko S, Weber G, Yerokhin V A and Stöhlker T 2016 *New J. Phys.* **18** 103034

Bransden B H and Joachain C J 2003 *Physics of Atoms and Molecules* (Harlow: Prentice Hall)

Cerjan A and Cerjan C 2011 *J. Opt. Soc. Am.* A **28** 2253

Choporova Yu Yu, Knyazev B A, Kulipanov G N, Pavelyev V S, Scheglov M A, Vinokurov N A, Volodkin B O and Zhabin V N 2017 *Phys. Rev.* A **96** 023846

Cohen H D and Fano U 1966 *Phys. Rev.* **150** 30

Cubaynes D, Bizau J M, Wuilleumier F J, Carré B and Gounand F 1989 *Phys. Rev. Lett.* **63** 2460

Davis B S, Kaplan L and McGuire J H 2013 *J. Opt.* **15** 035403

Davis L W 1979 *Phys. Rev.* A **19** 1177

Demtröder W 2011 *Atoms, Molecules and Photons. An Introduction to Atomic-, Molecular- and Quantum Physics* (Heidelberg, New York: Springer)

Eichler J and Stöhlker Th 2007 *Phys. Rep.* **439** 1

Eschner J 2003 *Eur. Phys. J.* D **22** 341

Fox M 2006 *Quantum Optics: An Introduction* (Oxford: Oxford University Press)

Haus H A 1984 *Waves and Fields in Optoelectronics* (Englewood Cliffs, NJ: Prentice-Hall)

Jackson J D 1962 *Classical Electrodynamics* (New York: Wiley)

Jentschura U D and Serbo V G 2011 *Phys. Rev. Lett.* **106** 013001

Johnson W R 2007 *Atomic Structure Theory* (New York: Springer)

Kane P P 1992 *Phys. Rep.* **218** 67

Kane P P, Kissel L, Pratt R H and Roy S C 1986 *Phys. Rep.* **140** 75

Lapierre A, Jentschura U D, Crespo López-Urrutia J R, Braun J, Brenner G, Bruhns H, Fischer D, González Martínez A J, Harman Z, Johnson W R, Keitel C H,

Mironov V, Osborne C J, Sikler G, Soria Orts R, Shabaev V, Tawara H, Tupitsyn I I, Ullrich J and Volotka A 2005 *Phys. Rev. Lett.* **95** 183001

Lebedev N N 1965 *Special Functions and Their Applications* (Englewood Cliffs, NJ: Prentice-Hall)

Matula O, Hayrapetyan A G, Serbo V G, Surzhykov A and Fritzsche S 2013 *J. Phys. B* **46** 205002

Molina-Terriza G, Torres J P and Torner L 2007 *Nat. Phys.* **3** 305

Monroe C, Meekhof D M, King B E, Itano W M and Wineland D J 1995 *Phys. Rev. Lett.* **75** 4714

Müller R A, Seipt D, Beerwerth R, Ornigotti M, Szameit A, Fritzsche S and Surzhykov A 2016 *Phys. Rev.* A **94** 041402(R)

Oskay W H, Diddams S A, Donley E A, Fortier T M, Heavner T P, Hollberg L, Itano W M, Jefferts S R, Delaney M J, Kim K, Levi F, Parker T E and Bergquist J C 2006 *Phys. Rev. Lett.* **97** 020801

Padgett M and Bowman R 2011 *Nature Photon.* **5** 343

Padgett M, Courtial J and Allen L 2004 *Phys. Today* **57** 35

Picón A, Benseny A, Mompart J, Vázquez de Aldana J R, Plaja L, Calvo G F and Roso L 2010 *New J. Phys.* **12** 083053

Picón A, Mompart J, Vázquez de Aldana J R, Plaja L, Calvo G F and Roso L 2010 *Opt. Express.* **18** 3660

Quinteiro G F and Berakdar J 2009 *Opt. Express* **17** 20465

Quinteiro G F, Reiter D E and Kuhn T 2015 *Phys. Rev.* A **91** 033808

Radwell N, Clark T W, Piccirillo B, Barnett S M and Franke-Arnold S 2015 *Phys. Rev. Lett.* **114** 123603

Rodrigues J D, Marcassa L G and Mendonça J T 2016 *J. Phys. B* **49** 074007

Rose M E 1957 *Elementary Theory of Angular Momentum* (New York: John Wiley and Sons)

Rudolph J K, Bernitt S, Epp S W, Steinbrügge R, Beilmann C, Brown G V, Eberle S, Graf A, Harman Z, Hell N, Leutenegger M, Müller A, Schlage K, Wille H-C, Yavaş H, Ullrich J and Crespo López-Urrutia J R 2013 *Phys. Rev. Lett.* **111** 103002

Schmiegelow C T and Schmidt-Kaler F 2012 *Eur. Phys. J.* D **66** 157

Schmiegelow C T, Schulz J, Kaufmann H, Ruster T, Poschinger U G and Schmidt-Kaler F 2016 *Nat. Commun.* **7** 12998

Scholz-Marggraf H M, Fritzsche S, Serbo V G, Afanasev A and Surzhykov A 2014 *Phys. Rev.* A **90** 013425

Seipt D, Müller R A, Surzhykov A and Fritzsche S 2016 *Phys. Rev.* A **94** 053420

Sherwin J A 2017 *Phys. Rev. A* **95** 052101

Siegman A E 1986 *Lasers* (Mill Valley, CA: University Science Books)

Smend F, Schaupp D, Czerwinski H, Schumacher M, Millhouse A H and Kissel L 1987 *Phys. Rev.* A **36** 5189

Stock S, Surzhykov A, Fritzsche S and Seipt D 2015 *Phys. Rev.* A **92** 013401

Surzhykov A, Seipt D and Fritzsche S 2016 *Phys. Rev.* A **94** 033420

Surzhykov A, Seipt D, Serbo V G and Fritzsche S 2015 *Phys. Rev.* A **91** 013403

Surzhykov A, Yerokhin V A, Jahrsetz T, Amaro P, Stöhlker Th and Fritzsche S 2013 *Phys. Rev.* A **88** 062515

Swartzlander G A, Ford E L, Abdul-Malik R S, Close L M, Peters M A, Palacios D M and Wilson D W 2008 *Opt. Express* **16** 10200

Tabosa J W R and Petrov D V 1999 *Phys. Rev. Lett.* **83** 4967

Varshalovich D A, Moskalev A N and Khersonskii V K 1988 *Quantum Theory of Angular Momentum* (Singapore: World Scientific)

Volotka A V, Yerokhin V A, Surzhykov A, Stöhlker Th and Fritzsche S 2016 *Phys. Rev.* A **93** 023418

Walde M, Jost A, Wicker K and Heintzmann R 2017 *Opt. Commun.* **383** 64

Walker G, Arnold A S and Franke-Arnold S 2012 *Phys. Rev. Lett.* **108** 243601

Walter M and Briggs J 1999 *J. Phys.* B **32** 2487

Watson G N 1966 *Theory of Bessel Functions* (Cambridge: Cambridge University Press)

Wätzel J and Berakdar J 2016 *Phys. Rev.* A **94** 033414

Yao A M and Padgett M J 2011 *Adv. Opt. Photon.* **3** 161

Acknowledgements

Publications

Results obtained in the course of elaborating this thesis are published in

- *Ionization of* H_2^+ *molecular ions by twisted Bessel light*
  Peshkov A A, Fritzsche S and Surzhykov A
  2015 *Phys. Rev.* A **92** 043415

- *Absorption of twisted light by a mesoscopic atomic target*
  Peshkov A A, Serbo V G, Fritzsche S and Surzhykov A
  2016 *Phys. Scr.* **91** 064001

- *Photoexcitation of atoms by Laguerre-Gaussian beams*
  Peshkov A A, Seipt D, Surzhykov A and Fritzsche S
  2017 *Phys. Rev.* A **96** 023407

- *Rayleigh scattering of twisted light by hydrogenlike ions*
  Peshkov A A, Volotka A V, Surzhykov A and Fritzsche S
  2018 *Phys. Rev.* A **97** 023802

Ehrenwörtliche Erklärung

Ich erkläre hiermit ehrenwörtlich, dass ich die vorliegende Arbeit selbstständig, ohne unzulässige Hilfe Dritter und ohne Benutzung anderer als der angegebenen Hilfsmittel und Literatur angefertigt habe. Die aus anderen Quellen direkt oder indirekt übernommenen Daten und Konzepte sind unter Angabe der Quelle gekennzeichnet.

Bei der Auswahl und Auswertung folgenden Materials haben mir die nachstehend aufgeführten Personen in der jeweils beschriebenen Weise unentgeltlich geholfen: Prof. Dr. Stephan Fritzsche, Prof. Dr. Andrey Surzhykov, Dr. Andrey V. Volotka, Dr. Daniel Seipt und Prof. Dr. Valery G. Serbo.

Weitere Personen waren an der inhaltlich-materiellen Erstellung der vorliegenden Arbeit nicht beteiligt. Insbesondere habe ich hierfür nicht die entgeltliche Hilfe von Vermittlungs- bzw. Beratungsdiensten (Promotionsberater oder andere Personen) in Anspruch genommen. Niemand hat von mir unmittelbar oder mittelbar geldwerte Leistungen für Arbeiten erhalten, die im Zusammenhang mit dem Inhalt der vorgelegten Dissertation stehen.

Die Arbeit wurde bisher weder im In- noch im Ausland in gleicher oder ähnlicher Form einer anderen Prüfungsbehörde vorgelegt.

Die geltende Promotionsordnung der Physikalisch-Astronomischen Fakultät ist mir bekannt.

Ich versichere ehrenwörtlich, dass ich nach bestem Wissen die reine Wahrheit gesagt und nichts verschwiegen habe.

Jena, den

....

Anton Anatolyevich Peshkov

Curriculum Vitae

Personal Information

Name	Anton Anatolyevich Peshkov
Born	10 June 1991 in Voronezh, Russia

School education

09.1998 - 06.2008	Gymnasium named after N. G. Basov, Voronezh, Russia

University education

09.2008 - 06.2012	Bachelor of Radiophysics, Physics Department, Saint-Petersburg State University, Russia
09.2012 - 06.2014	Master of Physics, Physics Department, Saint-Petersburg State University, Russia
11.2014 - 06.2018	Promotion, Physikalisch-Astronomische Fakultät, Friedrich-Schiller-Universität Jena, Germany

Employment

11.2014 - 06.2018	Research fellow, Helmholtz Institute Jena, Germany